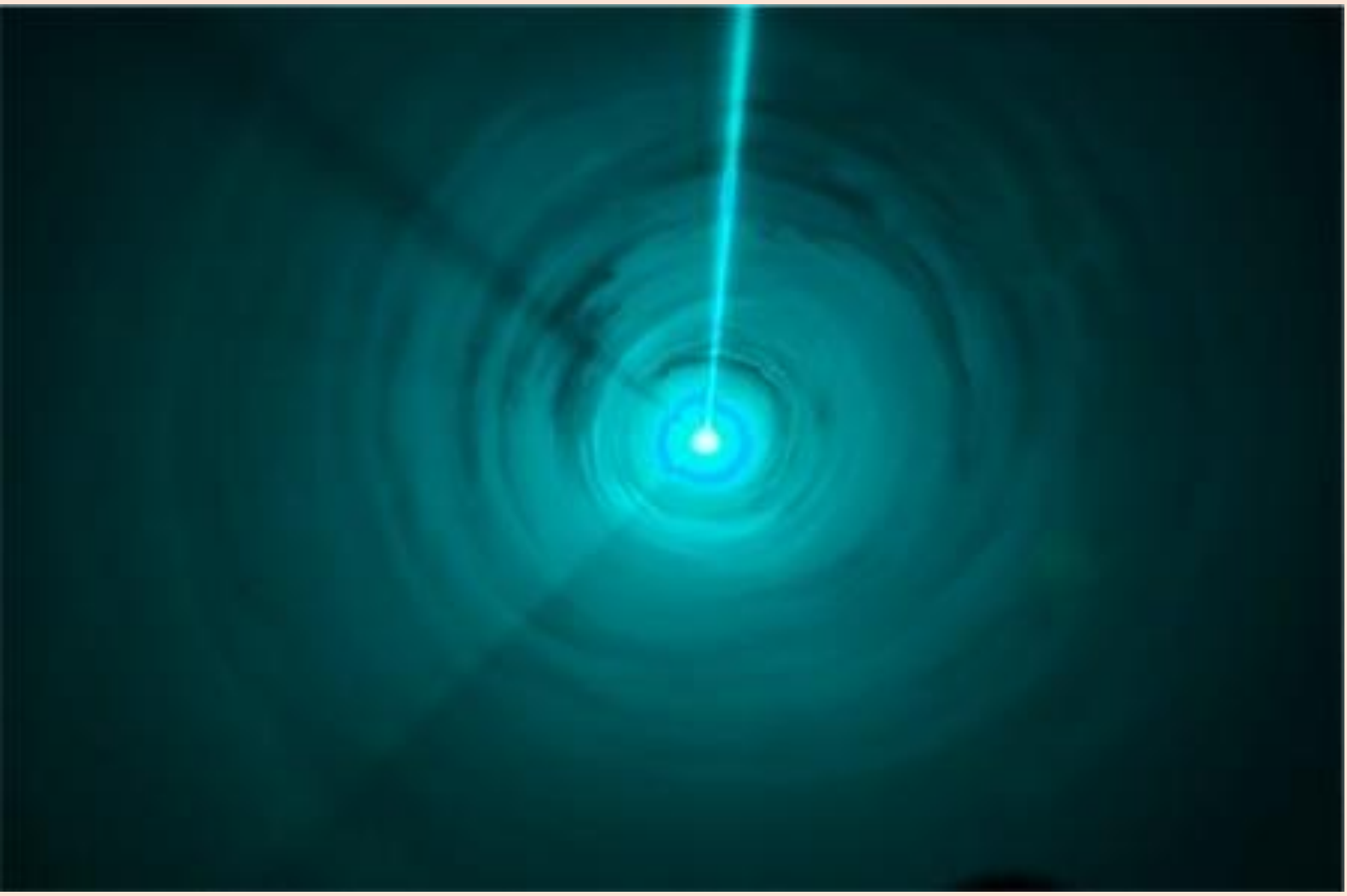
Vol.1, No 4 - December 2015

Special Issue: SFM

Journal of Biomedical Photonics & Engineering

http://journals.ssau.ru/JBPE



ISSN 2411-2844

SSAU

Journal of Biomedical Photonics & Engineering

Volume 1, Issue 4 (*December 2015*)

Special Issue:
Selected papers from Saratov Fall Meeting 2015

Elina A. Genina, Alexey N. Bashkatov, Valery V. Tuchin (eds.)

Editorial Board

Editor-In-Chief

Valery V. Tuchin - Saratov State University, Russia; Institute of Precision Mechanics and Control RAS, Russia; University of Oulu, Finland; Samara State Aerospace University, Russia

Deputy Editor-In-Chief

Valery P. Zakharov - Samara State Aerospace University, Russia

Editorial Board

Stefan Andersson-Engels (Lund University, Sweden), **Alexey N. Bashkatov** (Saratov State University, Russia), **Ekaterina Borisova** (Academician Emil Djakov Institute of Electronics, Bulgarian Academy of Sciences, Bulgaria), **Wei Chen** (University of Central Oklahoma, USA), **Arthur Chiou** (National Yang-Mind University, Taiwan), **Elina A. Genina** (Saratov State University, Russia), **Min Gu** (Swinburne University, Australia), **Vyacheslav Kalchenko** (The Weizmann Institute of Science, Israel), **Nikolay G. Khlebtsov** (Institute of Biochemistry and Physiology of Plants and Microorganisms RAS, Russia), **Juergen Lademann** (Charite University Clinic, Germany), **Kirill V. Larin** (University of Houston, USA), **Martin Leahy** (University of Galway, Ireland), **Qingming Luo** (Huazhong University of Science and Technology, China), **Stephen J Matcher** (University of Sheffield, Great Britain), **Igor Meglinski** (University of Oulu, Finland), **Vladimir S. Pavelyev** (Image Processing Systems Institute RAS, Russia), **Francesco Pavone** (University of Florence, Italy), **Roberto Pini** (Institute of Applied Physics, Italy), **Igor A. Platonov** (Samara State Aerospace University, Russia), **Juergen Popp** (Institute of Photonic Technology, Germany), **Alexander V. Priezzhev** (Moscow State University, Russia), **David Sampson** (The University of Western Australia, Australia), **Alexander Savitsky** (Institute of Biochemistry RAS, Russia), **Alexander P. Shkurinov** (Moscow State University, Russia), **Peter So** (Massachusetts Institute of Technologies, USA), **Janis Spigulis** (University of Latvia, Latvia), **Ilya V. Turchin** (Institute of Applied Physics RAS, Russia), **Vladimir G. Volostnikov** (N.P.Lebedev Physical Institute, Russia), **Lihong V. Wang** (Washington University, USA), **Ruikang Wang** (University of Washington, USA), **Xunbin Wei** (Shanghai Jiao Tong University, China), **Dan Zhu** (Britton Chance Center for Biomedical Photonics, Huazhong University of Science and Technology, China).

Publisher**: Samara State Aerospace University**

Postal address:
39B Lukacheva st., room #301
Samara 443086, Russian Federation

web: http://journals.ssau.ru/JBPE
phone: +7-846-267-24550
e-mail: j-bpe@ssau.ru

 © 2015 SSAU

Contents

Introduction

Special Issue: Optical Technologies for Biomedical Applications 208
by E.A. Genina, A.N. Bashkatov, and V.V. Tuchin

Reviews

Integrated intravascular ultrasound and optical coherence tomography technology: a promising tool to identify vulnerable plaques [INVITED PAPER] 209
by J. Li, and Z. Chen

Articles

Biophysical approach to the correction of supporting tissue microcirculation impairments 225
by S.I. Kireev, A.M. Imamov, and A.G. Kurmanov

Assessing mechanical properties of tissue phantoms with non-contact optical coherence elastography and Michelson interferometric vibrometry 229
by J. Li, C.-H. Liu, A. Schill, M. Singh, A. Nair, V.P. Zakharov, and K.V. Larin

Optical method for screening and a new proteinuria focus group 236
by A. Sünter, A. Frorip, V. Korsakov, R. Kurruk, A. Kuznetsov, and M. Ots-Rosenberg

The stress-related changes in the cerebral blood flow in newborn rats with intracranial hemorrhage: metabolic and endothelial mechanisms 248
by O. Sindeeva, E. Borisova, A. Abdurashitov, E. Zhinchenko, A. Gekalyuk, M. Ulanova, A.E. Sharif, V. Razubaeva, S. Serov, L. Yankovskaya, V. Tuchin, and O. Semyachkina-Glushkovskaya

Software development for estimation of optical clearing agent's diffusion coefficients in biological tissues 255
by P. Peixoto, L. Oliveira, M.I. Carvalho, E. Nogueira, and V.V. Tuchin

Statistical analysis of the parameters of the optic disk image 270
by V. Bakutkin, V. Gorelov, and Y. Zayko

Special Issue: Optical Technologies for Biomedical Applications

We are pleased to present the fourth issue of JBPE, which focuses on optical technologies for study of biological tissues and fluids. These are selected papers presented at Saratov Fall Meeting 2015 – International Symposium on Optics and Biophotonics - III (September 22-25, 2015, Saratov, Russia). This issue includes 7 representative papers that well characterize the major topics of SFM-15.

Development of non-contacted optical methods for detection the pathological alterations in tissues is an urgent problem of biomedical diagnostics. Invited paper of **J. Li and Zh. Chen** presents a novel integrated medical imaging modality IVUS-OCT (Intravascular Ultrasound and Optical Coherence Tomography) that provides opportunities for accurate assessment of vulnerable plaques *in vivo* in patients. The authors reviewed the fundamentals, technical designs, applications and future directions of IVUS-OCT technology. The paper of **J. Li** and co-authors is dedicated to comparison of two methods of noncontact optical elastography: a laser Michelson interferometric vibrometery and a phase-stabilized swept source optical coherence elastography system. The elasticity of tissue-mimicking agar phantoms was estimated from the velocity of air-pulse induced elastic waves as measured by these two techniques.

O. Sindeeva and co-authors used laser speckle-contrast imaging to found mechanisms underlying pathological processes in the cerebral blood flow in newborn rats. In this study, authors utilized a model of sound-stress-induced brain hemorrhages in newborns.

Method based on the optical absorption measurements (285 nm) in the protein fractions of urine received with use of the commercial desalting columns is developed in the paper of **A. Sünter** and co-authors.

The study of molecular diffusion in biological tissues is a research field of high importance with the multiple applications in diagnostics and therapeutics. Diffusion properties and dynamic viscosity of many immersion molecular agents can be evaluated from kinetic optical measurements. **P. Peixoto** and co-authors have developed a software that integrates all processing and calculations, turning the work easier and faster.

Computer program for analysis of the optic disc nerve images is presented by **V. Bakutkin** and co-authors. The goal of the study was to reveal the bounds of the norm for the glaucoma disease using the special “FUNDUS-camera” based on a microscope combined with the photo-camera.

Application of terahertz-frequency electro-magnetic radiation in medicine attracts more and more attention. The study of **S. Kireev** and co-authors demonstrates the possibility of terahertz wave therapy in the correction of microcirculation impairments in bone tissue.

In overall, papers collected in this special issue demonstrate well the exciting potential of optical technologies for biomedical studies and applications aiming medical diagnostics and treatment.

Special issue Editors:

Elina A. Genina, Alexey N. Bashkatov,
Optics and Biophotonics Department, Research and Educational Institute of Optics and Biophotonics of the Saratov National Research State University; Biophotonics Laboratory of the Tomsk National Research State University, Russia

Valery V. Tuchin,
Optics and Biophotonics Department, Research and Educational Institute of Optics and Biophotonics of the Saratov National Research State University; Institute of Precision Mechanics and Control RAS; Samara State Aerospace University, Russia

Integrated intravascular ultrasound and optical coherence tomography technology: a promising tool to identify vulnerable plaques [INVITED PAPER]

Jiawen Li[#], and Zhongping Chen*
Beckman Laser Institute, University of California, Irvine, 1002 Health Sciences Road East, Irvine, CA 92612, USA
The author is currently working at the Optical+Biomedical Engineering Laboratory, the University of Western Australia.

* Correspondence and requests for materials should be addressed to Z.C. (**e-mail:** z2chen@uci.edu)

Abstract. Heart attack is mainly caused by the rupture of a vulnerable plaque. IVUS-OCT is a novel medical imaging modality that provides opportunities for accurate assessment of vulnerable plaques *in vivo* in patients. IVUS provides deep penetration to image the whole necrotic core while OCT enables accurate measurement of the fibrous cap of a plaque owing to its high resolution. In this paper, the authors describe the fundamentals, the technical designs and the applications of IVUS-OCT technology. Results from cadaver specimens are summarized, which indicated the complementary nature of OCT and IVUS for assessment of vulnerable plaques, plaque composition, and stent-tissue interactions. Furthermore, previously reported *in vivo* animal experiments are reviewed to assess the clinical adaptability of IVUS-OCT. Future directions for this technology are also discussed in this review. © 2016 Samara State Aerospace University (SSAU).

Keywords: Optical coherence tomography, ultrasound, multi-modality imaging, intravascular imaging, vulnerable plaques, cardiology, intravascular OCT, IVUS, integraged IVUS/OCT.

Paper #2865 received 2015.11.29; revised manuscript received 2015.12.25; accepted for publication 2015.12.27; published online 2016.02.01.

References

1. K. Okrainec, D. K. Banerjee, and M. J. Eisenberg, "Coronary artery disease in the developing world," American Heart Journal 148(1), 7-15 (2004).
2. J. G. Kips, P. Segers, and L. M. Van Bortel, "Identifying the vulnerable plaque: A review of invasive and non-invasive imaging modalities," Artery Research 2(1), 21-34 (2008).
3. J. Sanz, and Z. A. Fayad, "Imaging of atherosclerotic cardiovascular disease," Nature 451(7181), 953-957 (2008).
4. D. Vancraeynest, A. Pasquet, V. Roelants, B. L. Gerber, and J.-L. J. Vanoverschelde, "Imaging the Vulnerable Plaque," Journal of the American College of Cardiology 57(20), 1961-1979 (2011).
5. J. R. Davies, J. H. F. Rudd, P. L. Weissberg, and J. Narula, "Radionuclide Imaging for the Detection of Inflammation in Vulnerable Plaques," Journal of the American College of Cardiology 47(8 SUPPL.), C57-C68 (2006).
6. T. Kubo, T. Imanishi, S. Takarada, A. Kuroi, S. Ueno, T. Yamano, Y. Matsuo, T. Masho, H. Kitabata, K. Tsuda, Y. Tomobuchi, and T. Akasaka, "Assessment of Culprit Lesion Morphology in Acute Myocardial Infarction," Journal of the American College of Cardiology 50(10), 934-939 (2007).
7. T. Sawada, J. Shite, H. M. Garcia-Garcia, T. Shinke, S. Watanabe, H. Otake, D. Matsumoto, Y. Tanino, D. Ogasawara, H. Kawamori, H. Kato, N. Miyoshi, M. Yokoyama, P. W. Serruys, and K.-I. Hirata, "Feasibility of combined use of intravascular ultrasound radiofrequency data analysis and optical coherence tomography for detecting thin-cap fibroatheroma," European Heart Journal 29(9), 1136-1146 (2008).

8. K. Fujii, H. Hao, M. Shibuya, T. Imanaka, M. Fukunaga, K. Miki, H. Tamaru, H. Sawada, Y. Naito, M. Ohyanagi, S. Hirota, T. Masuyama, "Accuracy of OCT, grayscale IVUS, and their combination for the diagnosis of coronary TCFA: An ex vivo validation study," JACC: Cardiovascular Imaging 8(4), 451-460 (2015).
9. M. Kawasaki, B. E. Bouma, J. Bressner, S. L. Houser, S. K. Nadkarni, B. D. MacNeill, I.-K. Jang, H. Fujiwara, and G. J. Tearney, "Diagnostic Accuracy of Optical Coherence Tomography and Integrated Backscatter Intravascular Ultrasound Images for Tissue Characterization of Human Coronary Plaques," Journal of the American College of Cardiology 48(1), 81-88 (2006).
10. J. Rieber, O. Meissner, G. Babaryka, S. Reim, M. Oswald, A. Koenig, T. M. Schiele, M. Shapiro, K. Theisen, M. F. Reiser, V. Klauss, and U.Hoffmann, "Diagnostic accuracy of optical coherence tomography and intravascular ultrasound for the detection and characterization of atherosclerotic plaque composition in ex-vivo coronary specimens: A comparison with histology," Coronary Artery Disease 17(5), 425-430 (2006).
11. M. Okubo, M. Kawasaki, Y. Ishihara, U. Takeyama, S. Yasuda, T. Kubota, S. Tanaka, T. Yamaki, S. Ojio, K. Nishigaki, G. Takemura, M. Saio, T. Takami, H. Fujiwara, and S. Minatoguchi, "Tissue characterization of coronary plaques - Comparison of integrated backscatter intravascular ultrasound with virtual histology intravascular ultrasound," Circulation Journal 72(10), 1631-1639 (2008).
12. F. Alfonso, J. Dutary, M. Paulo, N. Gonzalo, M. Pérez-Vizcayno, P. Jiménez-Quevedo, J. Escaned, C. Bañuelos, R. Hernández, and C. Macaya, "Combined use of optical coherence tomography and intravascular ultrasound imaging in patients undergoing coronary interventions for stent thrombosis," Heart 98(16), 1213-1220 (2012).
13. L. Räber, J. H. Heo, M. D. Radu, H. M. Garcia-Garcia, G. G. Stefanini, A. Moschovitis, J. Dijkstra, H. Kelbaek, S. Windecker, and P. W. Serruys, "Offline fusion of co-registered intravascular ultrasound and frequency domain optical coherence tomography images for the analysis of human atherosclerotic plaques," EuroIntervention 8(1), 98-108 (2012).
14. R. S. C. Cobbold, Foundations of Biomedical Ultrasound, Oxford University Press, USA (2006). ISBN: 978-0195168310
15. A. Ng, and J. Swanevelder, "Resolution in ultrasound imaging," Contin Educ Anaesth Crit Care Pain 11(5), 186-192 (2011).
16. A. Okamura, K. Iwakura, and K. Fujii, "ViewIT improves intravascular ultrasound-guided wiring in coronary intervention of chronic total occlusion," Catheterization and Cardiovascular Interventions 75(7), 1062-1066 (2010).
17. S. Tanaka, K. Sakamoto, R. Yamada, K. Nakagawa, P. G. Yock, P. J. Fitzgerald, F. Ikeno, and Y. Honda, "Plaque assessment with a novel high-definition 60-MHz IVUS imaging system: comparison with conventional 40MHz IVUS and Optical Coherence Tomography," J Am Coll Cardiol 61(10_S), E1878 (2013).
18. Y. Kobayashi, H. Kitahara, S. Tanaka, K. Nakagawa, K. Okada, K. Otagiri; P. Yock, P. Fitzgerald, F. Ikeno, and Y. Honda, "TCT-363 Precision of a Novel High-Definition 60MHz IVUS in Quantitative Measurement: Comparison with Conventional 40MHz IVUS and Optical Coherence Tomography," J Am Coll Cardiol 64(11_S), B105–B106 (2014).
19. G. J. Tearney, M. E. Brezinski, S. A. Boppart, B. E. Bouma, N. Weissman, J. F. Southern, E. A. Swanson, and J. G. Fujimoto, "Catheter-based optical imaging of a human coronary artery," Circulation 94(11), 3013-3013 (1996).
20. S.-J. Park, Y.-H. Kim, S.-W. Lee, and S.-W. Park, "Left main interventions: treatment of serious potential complications," Chapter 15 (Section E) in Handbook of Complications during Percutaneous Cardiovascular Interventions, Informa UK Ltd, 211-218 (2007).
21. J. Yin, H.-C. Yang, X. Li, J. Zhang, Q. Zhou, C. Hu, K. B. Kirk Shung, and Z. Chen, "Integrated intravascular optical coherence tomography ultrasound imaging system," Journal of biomedical optics 15(1), 010512 (2010).
22. J. Yin, X. Li, J. Jing, J. Li, D. Mukai, S. Mahon, A. Edris, K. Hoang, K. Kirk Shung, M. Brenner, J. Narula, Q. Zhou, and Z. Chen, "Novel combined miniature optical coherence tomography ultrasound probe for in vivo intravascular imaging," Journal of Biomedical Optics 16(6), 060505 (2011).
23. B. H. Li, A. S. O. Leung, A. Soong, C. E. Munding, H. Lee, A. S. Thind, N. R. Munce, G. A. Wright, C. H. Rowsell, V. X. D. Yang, B. H. Strauss, F. Stuart Foster, and B. K. Courtney, "Hybrid intravascular ultrasound and optical coherence tomography catheter for imaging of coronary atherosclerosis," Catheterization and Cardiovascular Interventions 81(3), 494-507 (2013).
24. J. Li, X. Li, D. Mohar, A. Raney, J. Jing, J. Zhang, A. Johnston, S. Liang, T. Ma, K. K. Shung, S. Mahon, M. Brenner, J. Narula, Q. Zhou, P. M. Patel, and Z. Chen, "Integrated IVUS-OCT for real-time imaging of coronary atherosclerosis," JACC: Cardiovascular Imaging 7(1), 101-103 (2014).
25. X. Li, J. Li, J. Jing, T. Ma, S. Liang, J. Zhang, D. Mohar, A. Raney, S. Mahon, M. Brenner, P. Patel, K. K. Shung, Q. Zhou, and Z. Chen, "Integrated IVUS-OCT Imaging for Atherosclerotic Plaque Characterization," IEEE Journal on Selected Topics in Quantum Electronics 20(2), 6573330 (2014).

26. J. Li, T. Ma, D. Mohar, E. Steward, M. Yu, Z. Piao, Y. He, K. K. Shung, Q. Zhou, P. M. Patel, and Z. Chen, "Ultrafast optical-ultrasonic system and miniaturized catheter for imaging and characterizing atherosclerotic plaques in vivo," Scientific Reports 5, 18406 (2015).
27. T.-H. Tsai, B. Potsaid, Y. K. Tao, V. Jayaraman, J. Jiang, P. J. S. Heim, M. F. Kraus, C. Zhou, J. Hornegger, H. Mashimo, A. E. Cable, and J. G. Fujimoto, "Ultrahigh speed endoscopic optical coherence tomography using micromotor imaging catheter and VCSEL technology," Biomedical Optics Express 4(7), 1119-1132 (2013).
28. R. Huber, M. Wojtkowski, and J. G. Fujimoto, "Fourier Domain Mode Locking (FDML): A new laser operating regime and applications for optical coherence tomography," Optics Express 14(8), 3225-3237 (2006).
29. X. Li, J. Yin, C. Hu, Q. Zhou, K. K. Shung, and Z. Chen, "High-resolution coregistered intravascular imaging with integrated ultrasound and optical coherence tomography probe," Applied Physics Letters 97(13), 133702 (2010).
30. H.-C. Yang, J. Yin, C. Hu, J. Cannata, Q. Zhou, J. Zhang, Z. Chen, and K. K. Shung, "A dual-modality probe utilizing intravascular ultrasound and optical coherence tomography for intravascular imaging applications," IEEE Transactions on Ultrasonics, Ferroelectrics, and Frequency Control 57(12), 2839-2843 (2010).
31. J. Li, T. Ma, J. Jing, J. Zhang, P. M. Patel, K. Kirk Shung, Q. Zhou, and Z. Chen, "Miniature optical coherence tomography-ultrasound probe for automatically coregistered three-dimensional intracoronary imaging with real-time display," Journal of Biomedical Optics 18(10), 100502 (2013).
32. J. Li, J. Yin, X. Li, J. Jing, D. Mukai, S. Mahon, A. Edris, K. Hoang, K. K. Shung, M. Brenner, J. Narula, Q. Zhou, P. Patel, and Z. Chen, "Miniature integrated optical coherence tomography (OCT) - ultrasound (US) probe for intravascular imaging," Proceedings of the SPIE 8207, 82073X (2012).
33. J. Li, T. Ma, D. Mohar, A. Correa, H. Minami, J. Jing, Q. Zhou, P. M. Patel, and Z, Chen, "Diagnostic accuracy of integrated intravascular ultrasound and optical coherence tomography (IVUS-OCT) system for coronary plaque characterization," Proceedings of the SPIE 8926, 892635 (2014).
34. J. Li, H. Minami, E. Steward, T. Ma, D. Mohar, C. Robertson, K. Shung, Q. Zhou, P. Patel, and Z. Chen, "Optimal flushing agents for integrated optical and acoustic imaging systems," Journal of Biomedical Optics 20(5), 056005 (2015).
35. R. Waksman, H. Kitabata, F. Prati, M. Albertucci, and G. S. Mintz, "Intravascular ultrasound versus optical coherence tomography guidance," Journal of the American College of Cardiology 62(17 SUPPL), S32-S40 (2013).
36. H. G. Bezerra, M. A. Costa, G. Guagliumi, A. M. Rollins, and D. I. Simon, "Intracoronary Optical Coherence Tomography: A Comprehensive Review. Clinical and Research Applications," JACC: Cardiovascular Interventions 2(11), 1035-1046 (2009).
37. Y. Ozaki, H. Kitabata, H. Tsujioka, S. Hosokawa, M. Kashiwagi, K. Ishibashi, K. Komukai, T. Tanimoto, Y. Ino, S. Takarada, T. Kubo, K. Kimura, A. Tanaka, K. Hirata, M. Mizukoshi, T. Imanishi, and T. Akasaka, "Comparison of contrast media and low-molecular-weight dextran for frequency-domain optical coherence tomography," Circulation Journal 76(4), 922-927 (2012).
38. V. V. Tuchin, D. M. Zhestkov, A. N. Bashkatov, and E. A. Genina, "Theoretical study of immersion optical clearing of blood in vessels at local hemolysis," Optics Express 12(13), 2966-2971 (2004).
39. X. Xu, R. K. Wang, J. B. Elder, and V. V. Tuchin, "Effect of dextran-induced changes in refractive index and aggregation on optical properties of whole blood," Physics in Medicine and Biology 48(9), 1205-1221 (2003).
40. M. Brezinski, K. Saunders, C. Jesser, X. Li, and J. Fujimoto, "Index matching to improve optical coherence tomography imaging through blood," Circulation 103(15), 1999-2003 (2001).
41. E. A. Genina, A. N. Bashkatov, Yu. P. Sinichkin, I. Yu. Yanina, and V. V. Tuchin, "Optical clearing of biological tissues: prospects of application in medical diagnostics and phototherapy," J of Biomedical Photonics & Eng l(1), 22-58 (2015).
42. V. V. Tuchin, X. Xu, and R. K. Wang, "Dynamic optical coherence tomography in studies of optical clearing, sedimentation, and aggregation of immersed blood," Applied Optics 41(1), 258-271 (2002).
43. K. Ohtsuki, M. Hayase, K. Akashi, S. Kopiwoda, and H. W. Strauss, "Detection of monocyte chemoattractant protein-1 receptor expression in experimental atherosclerotic lesions: An autoradiographic study," Circulation 104(2), 203-208 (2001).
44. F. D. Kolodgie, A. Petrov, R. Virmani, N. Narula, J. W. Verjans, D. K. Weber, D. Hartung, N. Steinmetz, J. L. Vanderheyden, M. A. Vannan, H. K. Gold, C. P. M. Reutelingsperger, L. Hofstra, and J. Narula, "Targeting of Apoptotic Macrophages and Experimental Atheroma with Radiolabeled Annexin V: A Technique with Potential for Noninvasive Imaging of Vulnerable Plaque," Circulation 108(25), 3134-3139 (2003).
45. P. Schoenhagen, K. M. Ziada, D. G. Vince, S. E. Nissen, and E. M. Tuzcu, "Arterial remodeling and coronary artery disease: the concept of "dilated" versus "obstructive" coronary atherosclerosis," Journal of the American College of Cardiology 38(2), 297-306 (2001).

46. G. J. Tearney, I.-K. Jang, and B. E. Bouma, "Optical coherence tomography for imaging the vulnerable plaque," Journal of Biomedical Optics 11(2), 021002 (2006).
47. C. Xu, J. M. Schmitt, S. G. Carlier, and R. Virmani, "Characterization of atherosclerosis plaques by measuring both backscattering and attenuation coefficients in optical coherence tomography," Journal of Biomedical Optics 13(3), 034003 (2008).
48. G. Van Soest, T. Goderie, E. Regar, S. Koljenović, G. L. J. H. Van Leenders, N. Gonzalo, S. Van Noorden, T. Okamura, B. E. Bouma, G. J. Tearney, J. Wolter Oosterhuis, P. W. Serruys, and A. F. W. Van Der Steen, "Atherosclerotic tissue characterization in vivo by optical coherence tomography attenuation imaging," Journal of Biomedical Optics 15(1), 011105 (2010).
49. N. Gonzalo, J. Escaned, F. Alfonso, P. Jiménez-Quevedo, B. Zakhem, C. Bañuelos, R. Hernández-Antolín, and C. Macaya, "Is refined OCT guidance of stent implantation needed?" EuroIntervention 6(Suppl G), G145-153 (2010).
50. A. V. Finn, M. Joner, G. Nakazawa, F. Kolodgie, J. Newell, M. C. John, H. K. Gold, and R. Virmani, "Pathological correlates of late drug-eluting stent thrombosis: Strut coverage as a marker of endothelialization," Circulation 115(18), 2435-2441 (2007).
51. N. Gonzalo, P. W. Serruys, T. Okamura, Z. J. Shen, H. M. Garcia-Garcia, Y. Onuma, R. J. Van Geuns, J. Ligthart, and E. Regar, "Relation between plaque type and dissections at the edges after stent implantation: An optical coherence tomography study," International Journal of Cardiology 150(2), 151-155 (2011).
52. S. Tahara, H. G. Bezerra, V. Sirbu, H. Kyono, G. Musumeci, N. Rosenthal, G. Guagliumi, and M. A. Costa, "Angiographic, IVUS and OCT evaluation of the long-term impact of coronary disease severity at the site of overlapping drug-eluting and bare metal stents: A substudy of the ODESSA trial," Heart 96(19), 1574-1578 (2010).
53. F. Alfonso, M. Paulo, N. Gonzalo, J. Dutary, P. Jimenez-Quevedo, V. Lennie, J. Escaned, C. Bauelos, R. Hernandez, and C. MacAya, "Diagnosis of spontaneous coronary artery dissection by optical coherence tomography," Journal of the American College of Cardiology 59(12), 1073-1079 (2012).
54. L. Misuraca, F. De Caro, C. Grigoratos, M. De Carlo, and A. S. Petronio, "OCT-guided stenting of a spontaneous coronary artery dissection," Cardiovascular Revascularization Medicine 13(5), 301-303 (2012).
55. K. Poon, A. Incani, A. Small, and O. C. Raffel, "Drug eluting stents trapping intramural hematoma in spontaneous coronary artery dissection and healing pattern at six months: Optical coherence tomography findings," Cardiovascular Revascularization Medicine 14(3), 183-186 (2013).
56. M. Paulo, J. Sandoval, V. Lennie, J. Dutary, M. Medina, N. Gonzalo, P. Jimenez-Quevedo, J. Escaned, C. Bañuelos, R. Hernandez, C. Macaya, and F. Alfonso, "Combined use of OCT and IVUS in spontaneous coronary artery dissection," JACC: Cardiovascular Imaging 6(7), 830-832 (2013).
57. The Global Market for Intravascular Ultrasound Tools and Ancillary Equipment, BCC Research
58. P. R. Moreno, R. A. Lodder, K. R. Purushothaman, W. E. Charash, W. N. O'Connor, J. E. Muller, "Detection of lipid pool, thin fibrous cap, and inflammatory cells in human aortic atherosclerotic plaques by near-infrared spectroscopy," Circulation 105(8), 923-927 (2002).
59. J. Wang, Y.-J. Geng, B. Guo, T. Klima, B. N. Lal, J. T. Willerson, and W. Casscells, "Near-infrared spectroscopic characterization of human advanced atherosclerotic plaques," Journal of the American College of Cardiology 39(8), 1305-1313 (2002).
60. P. Wang, T. Ma, M. N. Slipchenko, S. Liang, J. Hui, K. K. Shung, S. Roy, M. Sturek, Q. Zhou, Z. Chen, and J.-X. Cheng, "High-speed intravascular photoacoustic imaging of lipid-laden atherosclerotic plaque enabled by a 2-kHz Barium Nitrite Raman Laser," Scientific Reports 4, 6889 (2014).
61. B. Wang, A. Karpiouk, D. Yeager, J. Amirian, S. Litovsky, R. Smalling, and S. Emelianov, "In vivo Intravascular Ultrasound-guided Photoacoustic Imaging of Lipid in Plaques Using an Animal Model of Atherosclerosis," Ultrasound in Medicine and Biology 38(12), 2098-2103 (2012).
62. Z. Piao, T. Ma, J. Li, M. Wiedmann, S. Huang, M. Yu, K. K. Shung, Q. Zhou, C. S. Kim, and Z. Chen, "High speed intravascular photoacoustic imaging with fast OPO laser at 1.7 μm," Applied Physics Letters 107(8), 083701 (2015).
63. W. Wei, X. Li, Q. Zhou, K. K. Shung, and Z. Chen, "Integrated ultrasound and photoacoustic probe for co-registered intravascular imaging," Journal of Biomedical Optics 16(10), 106001 (2011).
64. X. Li, W. Wei, Q. Zhou, K. K. Shung, and Z. Chen, "Intravascular photoacoustic imaging at 35 and 80 MHz," Journal of Biomedical Optics 17(10), 106005 (2012).
65. B. F. Kennedy, K. M. Kennedy, and D. D. Sampson, "A review of optical coherence elastography: Fundamentals, techniques and prospects," IEEE Journal on Selected Topics in Quantum Electronics 20(2), 6670078 (2014).
66. S. J. Kirkpatrick, R. K. Wang, and D. D. Duncan, "OCT-based elastography for large and small deformations," Optics Express 14(24), 11585-11597 (2006).

67. J. Zhu, Y. Qu, T. Ma, R. Li, Y. Du, S. Huang, K. K. Shung, Q. Zhou, and Z. Chen, "Imaging and characterizing shear wave and shear modulus under orthogonal acoustic radiation force excitation using OCT Doppler variance method," Optics Letters 40(9), 2099-2102 (2015).
68. W. Qi, R. Li, T. Ma, J. Li, K. Kirk Shung, Q. Zhou, and Z. Chen, "Resonant acoustic radiation force optical coherence elastography," Applied Physics Letters 103(10), 103704 (2013).
69. W. Qi, R. Chen, L. Chou, G. Liu, J. Zhang, Q. Zhou, and Z. Chen, "Phase-resolved acoustic radiation force optical coherence elastography," Journal of Biomedical Optics 17(11), 110505 (2012).
70. W. Qi, R. Li, T. Ma, K. Kirk Shung, Q. Zhou, and Z. Chen, "Confocal acoustic radiation force optical coherence elastography using a ring ultrasonic transducer, " Applied Physics Letters 104(12), 123702 (2014).

1 Introduction

Coronary artery disease (CAD) is the current number one cause of death worldwide [1]. CAD is ascribed to the development of atherosclerotic plaques. The vast majority of plaques remain stable after built and won't cause any acute coronary syndromes, such as heart attacks. Vulnerable (unstable) plaques, however, are prone to rupture and may lead to life-threatening events.

To detect atherosclerotic plaques, X-ray angiography is routinely employed in hospitals. By providing a two-dimensional (2D) visualization of patients' coronary arteries, angiography shows where there is a severe stenosis. However, extensive data showed that vulnerable plaques are actually less obtrusive plaques and are characterized with a large lipid core overlaid by a thin fibrous cap, which are not visible by angiography. Therefore, angiography is usually not able to accurately discern vulnerable plaques, prognose, and prevent heart attack.

A variety of three-dimensional (3D) imaging techniques have been developed to image plaques. Some techniques are non-invasive, where there is no need of inducing a catheter into body, and others are minimally invasive. Well-developed non-invasive imaging modalities include ultrasound, computed tomography (CT), magnetic resonance imaging (MRI), single photon emission computed tomography (SPECT) and positron emission tomography (PET). Ultrasound [2] (spatial resolution ~400 μm) can image large superficial arteries, such as carotid, iliac and femoral arteries, by placing an ultrasound transducer closer to those arteries. CT (spatial resolution ~400 μm) provides 3D information by rotating the X-ray source or detector around the patient's body and reconstructing acquired 2D images [3]. MRI (spatial resolution ~250 μm) can characterize and quantify plaque composition by using a strong homogenous magnetic field [4]. Using a similar mechanism, magnetic resonance angiography (MRA) can assess the distribution of stenotic plaques [2]. SPECT (spatial resolution ~1 cm) can detect inflammations, a process closely associated with the severity of atherosclerosis, by using gamma rays [2, 4, 5]. PET (spatial resolution ~4 mm) can also visualize inflammation, by detecting annihilation ɣ-photons [2, 4, 5]. Currently, PET and SPECT are only used for preclinical study [2], unlike MRI and CT which has been used for clinical studies to image carotid arteries. However, the coronary arteries, where heart attack happens, are much smaller than carotid arteries and are constantly moving along with the cardiac and respiratory motions. At the present stage of development, none of these non-invasive imaging modalities are capable for imaging of a coronary artery with enough spatial and temporal resolution to characterize and quantify vulnerable plaques. Therefore, they are also not suitable for identifying vulnerable plaques that cause acute coronary syndromes.

On the other hand, minimally invasive methods, such as intravascular ultrasound (IVUS) and optical coherence tomography (OCT), enable clear 3D visualization of coronary arteries. IVUS is used to visualize the size of a plaque burden, such as the lipid core of a vulnerable plaque. Furthermore, post-processing of the IVUS signal (virtual histology-IVUS and integrated backscatter-IVUS) offers another contrast to characterize plaque composition. However, the axial resolution of IVUS is only 100-200 μm and, thus, cannot measure the thickness of a fibrous cap. In contrast, the axial resolution of OCT is better than 10 μm and allows accurate measurement of the thickness of a fibrous cap. Nevertheless, OCT can only penetrate ~1.5 mm in coronary arteries, making it challenging and unreliable for evaluating the size of a large lipid core. As shown in Table 1, OCT has high spatial resolution but low penetration depth. IVUS has deep penetration depth but low resolution. OCT and IVUS provide complementary information for high risk plaque identification.

Clinical studies, using separate IVUS and OCT catheters, also validated this observation. In 2007, a study which enrolled 30 patients with acute myocardial infarction was reported [6]. In this study, the ability of OCT and IVUS to assess vulnerable plaques was compared. In 2008, Sawada et al. [7] imaged and evaluated plaques *in vivo* in 56 patients using separate IVUS and OCT catheters. They found that neither modality was capable of identifying vulnerable plaques accurately, but these two modalities provided complementary information about vulnerable plaques. Accordingly, they proposed that the combined use of IVUS and OCT may be a sensible tool to detect vulnerable plaques. In 2015, an *ex vivo* study with a bigger sample size was conducted and validated this proposed idea [8]. In this study, 685 regions of interests were imaged. Since this study was performed on cadaver samples instead of live patients, histology slides

Table 1 Comparison of OCT and IVUS in clinical applications in cardiology.

		OCT	IVUS
Axial resolution		10 μm	100-200 μm
Penetration depth		1-2 mm	More than 5 mm
Vulnerable plaques identification	Detect thin fibrous cap	Strong. The only clinically available technology to measure fibrous cap thickness	Weak
	Large lipid or necrotic core	Not able to image deeper than 1.5 mm	Strong
	Contrast of lipid and others	Relatively strong	Weak
Plaque type classification	Calcification	Strong	Stronger than OCT
	Lipid	Stronger than IVUS	Weak
	Fibrosis	Stronger than IVUS	Weak
Stent	Small degrees of in-stent neointima	Strong	Weak but more clinical evidence reported
	Uncovered struts	Strong	Weak but more clinical evidence reported

of the imaged regions could be dissected and analyzed to compare with image-guided diagnosis. By using histology as the gold standard, the positive predictive value (PPV) was found to be increased from 19% (IVUS-only) or 41% (OCT-only) to 69% when IVUS was used in combination with OCT. Thus, they concluded that the combined use of OCT and IVUS may improve the detection accuracy of vulnerable plaques. Apart from the complementary nature of IVUS and OCT in identifying vulnerable plaques, there is an increased number of studies showing that IVUS and OCT allow for assessment of different plaque compositions [9-11] and stent-tissue interaction [12], as summarized in Table 1.

It should be noted that all these studies were conducted using separate IVUS and OCT catheters and co-registered the IVUS and OCT data sets off-line. The co-registration was performed based on artery landmarks [7, 8, 13], such as side branches and calcifications, manually or semi-automatically. This process could result in human error and interobserver variances. Moreover, it cannot provide real-time evaluation of the artery and cannot fit the need for guiding intervention on the spot. An integrated IVUS-OCT system can address all these issues and provide complementary information to discern vulnerable plaques simultaneously, and, thus, enable intraoperative guidance.

Therefore it can be stated that an integrated IVUS and OCT system holds great promise in improving clinical outcomes in cardiology.

Over the past 6 years, integrated IVUS-OCT systems for cardiovascular applications have been developed. In this review, the fundamentals of IVUS and OCT are described first to prepare readers about the key concerns of building an integrated IVUS-OCT system and catheter. Then the fundamental challenges and technical advances of IVUS-OCT technology are presented. *In vivo* and *ex vivo* studies assessing the potentials of IVUS-OCT for imaging plaques are also reviewed. Last but not least, some future research directions are discussed.

2 Fundamentals of IVUS and OCT and their commercial products

The goal of developing integrated IVUS-OCT technology is to provide the advantages of both technologies at the same time. Consequently, we will first describe fundamentals of IVUS-alone and OCT-alone technologies before reviewing the integrated technology. Such an understanding is vital if IVUS-OCT is to be successfully developed. In this section, important parameters and features of IVUS and OCT technologies are described, and commonly-used commercial IVUS or OCT products are introduced and compared.

There are two main components for an intravascular imaging apparatus (either an IVUS or OCT apparatus): the imaging system and the catheter. The imaging system is to generate light or ultrasound for detection and to receive and process the returned signal. The catheter is a miniaturized sensor inserted into the artery to acquire signals *in situ*.

2.1 IVUS

The most important parameters of an IVUS apparatus are the resolution of the system and the outer diameter of the catheter.

The axial resolution of IVUS is determined by the central frequency and the bandwidth of the ultrasound system [14, 15]:

$$B = \frac{V}{2 \cdot f_o \cdot BW},$$

where f_0 is central frequency, BW is the fractional frequency bandwidth, and V is speed of sound. The comparison of central frequencies of commercial IVUS

Table 2 Comparison of commercial IVUS products.

Company name	Product name	Central frequency (MHz)	Outer diameter (French)	Other features
Boston scientific	iCross™	40	3.5	
	Atlantis™ SR Pro	40	3.6	
	OptiCross™	40	3.15	It performs a higher axial resolution than those of other Boston Scientific IVUS products.
Philips (Volcano)	Revolution®	45	3.2	Virtual histology function is available.
	Eagle Eye®	20	3.5	The sensor is a phase array and ChromaFlo® imaging function is available.
Terumo	View IT®	40	2.6 (3.2)*	It has a smaller diameter of its imaging window (2.6 French) than its proximal shaft (3.2 French).
	Intrafocus®	40	2.4 (3.2)	Two guide-wire channels: at the bent portion, more stable
ACIST	Kodama® HD-IVUS	60	N.A.	There are reports [17, 18] that this product can run at a faster imaging speed than other commercial IVUS products, but no product is available yet for sale. **

*Crossing profile is 2.6 French and the outer diameter of the proximal shaft is 3.2F.
**The imaging speed of these products are all between 20 fps to 35 fps, except ACIST.

products is summarized in column 3, Table 2. Two commercial products, Opticross and iCross from Boston Scientific, have the same center frequency, but Opticross performs with a superior resolution because of its broad bandwidth.

The lateral resolution of IVUS is determined by the beam spot exiting the ultrasound transducer [14, 15]:

$$R = \frac{V}{f_0} \cdot F\#,$$

where F# is the quotient of the focal length f and the outer diameter D of the transducer aperture.

Lateral resolution is not discussed as often as the axial resolution because most intravascular applications focus on resolving the cross-sectional features of the multilayered structure of the artery lumen, which are in the axial direction.

The outer diameter over the entire length of a catheter is usually not a constant value. The crossing profile, i.e., the outer diameter of the distal tip, determines how small a vascular lesion that this catheter can go into, while the proximal shaft size determines the size of the guiding catheter that this imaging catheter can be used with and pass through. For example, a key feature of Terumo's IVUS products is the small crossing profile although the proximal shaft diameters of these products are similar to other companies' products. This special design is used for accessing arteries with large plaque burdens, such as those with chronic total occlusion [16]. The comparison of outer diameters of commercial IVUS products is summarized in column 4, Table 2.

Some other features of IVUS commercial products, which are possible to be added in an integrated IVUS-OCT apparatus, are also listed in Table 2. Volcano is a company dedicated to developing IVUS technology. It has developed and implemented a number of software based imaging processing features, such as virtual histology, which provides automatic analysis of plaque components, and ChromaFlo®, which indicates the locations of blood vessels, to enhance IVUS capability. Recently, Volcano was acquired by Philips. Silicon Valley Medical Instrument, a relatively new player in the IVUS market, was acquired by ACIST. Its product is highlighted by a higher frequency and higher imaging speed than those of established IVUS players.

2.2 OCT

Unlike IVUS, which was invented 60 years ago, OCT is relatively new, and the first use of OCT in cardiology was briefly reported in Circulation in 1996 [19]. Two decades of research in OCT cardiovascular imaging has led to the generation of two commercial product-lines, from St. Jude Medical and Terumo.

The two most important features, the outer diameter of the catheter and the imaging speed of commercial OCT products, are compared in Table 3. Similar to IVUS, the outer diameter of a catheter determines whether a catheter can cross a heavily blocked coronary artery. There are several generations of St. Jude Medical products: the imaging speed has increased from 20 frames per second (fps, M2/M3) to 100 fps (C7XR) and now to 180 fps (ILUMIEN™ OPTIS™). However, they are very similar in terms of the catheter size and thus only the latest product is listed here for comparison.

Some other clinically relevant features, which could be considered in future to improve the design of an IVUS-OCT catheter, are also listed. Purging, injecting saline into the lumen of a catheter, is needed for St. Jude Medical products. This extra step is to reduce astigmatism and high reflection signals caused by the catheter sheath and to decrease non-uniform rotational distortion (NURD). But some clinicians may find this step cumbersome and prefer using a non-purge catheter.

Table 3 Comparison of commercial OCT products.

		Crossing profile	Speed	Other feature
Terumo	LUNAWAVE™ OFDI	2.4 F	160 fps	No purge is needed.
St. Jude Medical (Lightlab)	ILUMIEN™ OPTIS™	2.7 F	180 fps	It has a dual-lumen tip design for excellent handling and automated, continuous calibration.

As shared by both IVUS-alone and OCT-alone technologies, the speed, the catheter size, and the image quality (such as spatial resolution) are key features. Although it is ideal to keep the best performance of each system when integrating IVUS and OCT together, there are many theoretical and engineering challenges in achieving this goal. Technical advances addressing these challenges, in terms of the system and the catheter, will be separately described in the following two sections.

3 Integrated IVUS-OCT system

The foremost challenge of a clinically-adaptable integrated IVUS-OCT system lies in enabling high imaging speed [13]. There is a large gap between the imaging speeds of current commercial IVUS and OCT systems. For safe intracoronary imaging in humans, an ultrafast integrated IVUS-OCT imaging system, which can image at over 70 fps and take less than 4 seconds for imaging a coronary artery, would be critical to translate this technology to clinical applications. By using an ultrafast system, the risk of catheter-induced spasm [20] and the use of a toxic contrast agent would be significantly reduced. This breakthrough could expedite the translation of the IVUS-OCT technology into clinical practice. However, the speed of most state-of-the-art commercial IVUS systems is only around 30 fps. No IVUS system, either commercial or investigational, running over 70 fps has been reported. Thus, to develop an ultrafast IVUS-OCT system, we have to first develop an ultrafast IVUS sub-system and then build a synchronized IVUS-OCT system without sacrificing the imaging quality of either sub-system.

A common design for an integrated IVUS-OCT system is shown in Fig. 1. IVUS and OCT sub-systems are used getting IVUS and OCT signals, respectively. Acquired IVUS and OCT signals are then sent to a data acquisition (DAQ) card and work station for processing. Radial scanning is usually achieved by using a motor to rotate the optical rotary joint and, hence, the probe. The electrical and optical signals are transferred from a rotational to a stationary side usually by an electrical slip ring and an optical rotary joint, respectively. The pullback movement of a catheter is induced by using a linear stage. The imaging speed of the system (i.e., the rotation speed of an imaging probe) is usually determined by the system. However, the transmission of rotation, mechanical strength and coaxial of the catheter may cause non-uniform rotational distortion (NURD) during high speed rotation and thus limit the rotation speed of an OCT probe.

Previous research on different generations of IVUS-OCT systems can be summarized as a journey to increase the imaging speed of this common system design. In 2010, a system with a speed of 1 fps was reported [21]. By using a digitizer for data acquisition and a graphics processing unit (GPU) for signal processing, 4 fps was reached in 2011 [22]. A 5-fps imaging system, which used separated data acquisition boards for IVUS and OCT signals, was published in 2013 [23]. Soon after this, 20 fps, a speed that is the same order of that of a commercial IVUS system, was achieved and safely demonstrated *in vivo* in pigs and rabbits [24, 25]. In 2015, an integrated IVUS-OCT system running at an imaging speed of 72 fps was reported [26] by using a customized slip ring, an ultrahigh write-speed solid-state drive (SSD), and an ultrasound pulser/receiver faster than those employed in a commercial IVUS system [4]. This breakthrough facilitates the implementation of IVUS-OCT into clinical practice. In the following paragraphs, key elements and difficulties of previously-reported IVUS-OCT systems will be summarized.

3.1 OCT sub-system

In an integrated IVUS-OCT system, Fourier Domain OCT (FDOCT) is usually used. FDOCT is achieved by calculating the Fourier transform of an acquired spectra. Mechanically scanning the reference arm is not needed to get depth information; thus, a faster imaging speed can be achieved using FDOCT instead of time domain OCT (e.g., the first generation commercial system St. Jude Medical M2/M3). The interference signal in the frequency domain (i.e., wavelength domain) is acquired using either a frequency-swept laser source (swept source OCT, SSOCT) or a spectrometer using a high speed line-scan camera as the detector (Spectral domain OCT, SDOCT). With the development of fast swept lasers [27, 28], the SSOCT is able to scan at a few megahertz. In general, the SSOCT system is also more compact than SDOCT. Accordingly, a SSOCT system was commonly used to be integrated with an IVUS sub-system for dual-modality intravascular imaging.

3.2 IVUS sub-system

The IVUS sub-system is achieved by using an IVUS pulser/receiver, which can be bought as one instrument or built by using a separate pulser [23], a

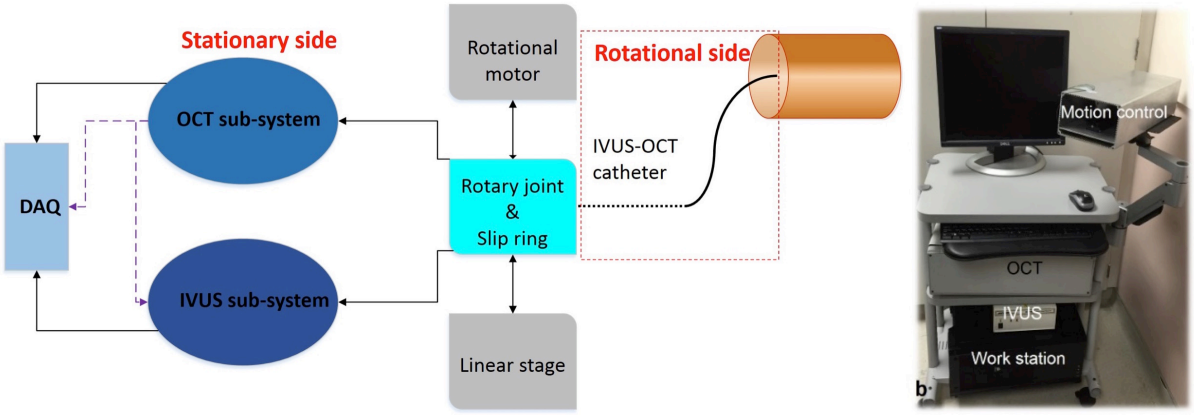


Fig. 1 Diagram (a) and photo (b) of a fully-integrated IVUS-OCT system. Black solid lines indicate IVUS and OCT signal transfer paths. Purpule dash lines denote the trigger signals.

transmit/receive switch, and a pre-amplifier. A pulse energy of 1-5 μJ is usually used to drive an IVUS transducer. In one design of the IVUS-OCT systems [21-23, 29], a Panametrics PR5900 pulser/receiver (Olympus NDT, Kennewick, WA) was used to drive the transducer for pulse generation and subsequent echo signal detection. For ultra-high speed imaging, a 50 kHz-external-triggered ultrasound pulser (PR-H4, JSR Ultrasonics, Pittsford, NY) [26] and a customized receiver were used to drive the transducer and detect the eco signal, respectively.

3.3 Synchronization of the system

Synchronization between the OCT sub-system, the IVUS sub-system and the DAQ card in the integrated system design is critical. Otherwise, the IVUS imaged location may not match that of OCT. Usually the A-line trigger signal of the OCT sub-system, which indicates the beginning of an OCT acquisition, is sent to the IVUS sub-system and the DAQ card for synchronizing the entire integrated system, see purple dash lines in Fig. 1. There could be other ways of synchronization, such as altering timing between IVUS-OCT by using a function generator, or acquiring multiple OCT frames while only acquiring a single IVUS frame (due to IVUS's low imaging speed).

3.4 The fundamental challenge for an IVUS-OCT system

Because it takes time for a sound wave to travel, there is a theoretical imaging-speed limit of an IVUS-OCT system. For the IVUS sub-system, when the rotation speed is over a certain value, the echo signal generated by the sample cannot be detected by the aperture of the IVUS transducer. This is because the transducer had already rotated to a different location and there is little overlap between the new location and the original location, see Fig. 2. A simple calculation can be used to estimate the theoretical limitation of IVUS sub-system. If we want to image to 5 mm deep, t1, which represents the time of the ultrasound wave to travel from the transducer to the sample and back to the transducer, is 10mm/1560 m/s= 6.4 μs. If a 50% overlap is needed to maintain enough detection sensitivity, t2, the time taken to rotate between 2 frames, needs to be considerably bigger than t1. Thus, the maximal speed of this system is calculated to be 78 kHz. Assume acquiring 500 A-lines per frame, the theoretical limit for IVUS is 156 frames per second. In addition, the less overlap that there is between the end and original locations and the farther that the sound travels (i.e., imaging a deeper sample), the less signal that can be collected. Accordingly, the sensitivity of an IVUS system drops when running at an ultrafast speed. We tested the contrast to noise ratio (CNR), an important indicator of the IVUS system sensitivity, at different imaging speeds. It was found that CNR was gradually decreasing as the speed of the system increased: CNR=6.49 dB (at 25 fps); CNR=6.19 dB (at 50 fps) and CNR=6.18 dB (at 72 fps). This experiment finding validated our theoretical analysis. On the other hand, there is almost no theoretical limit for OCT imaging speed since the speed of light is significantly higher (~20,000 times in blood) than that of sound.

3.4.1 OCT sub-system and IVUS sub-system

For the OCT sub-system, a 50 kHz (or higher frequency) swept laser is commercially available. However, off-the-shelf pulser/receivers, which fit the requirements of SNR, pulse power, external trigger compatibility, and frequency response for an IVUS sub-system, are usually running at a speed below 30 kHz. Thus, a customized or home-made pulser/receiver is needed for an ultrafast imaging system.

3.4.2 Design of rotary system

Similar to the ultrafast pulser/receiver, there are few off-the-shelf slip rings that can transmit a signal over 50

fps, while maintaining a decent performance. To keep an OCT and IVUS imaging probe co-axial even at the proximal end, a through-hole slip ring is usually used. The imaging probe is inserted through the hole of the slip ring. A 72 fps IVUS-OCT system was reported recently where a customized slip ring was used [26].

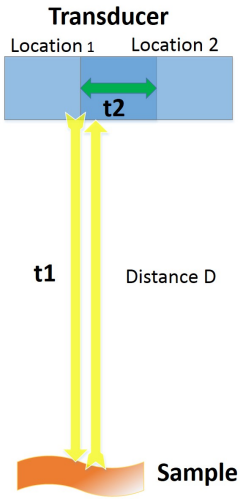


Fig. 2 Demonstration of the theoretical speed limit of an IVUS system.

3.4.3 IT challenge

Ultrafast imaging also requires the DAQ card and the work station to transfer, process and display the signal at an ultrahigh speed. GPU, a PCI express bus for transferring the data and a high writing speed SSD can be used to address this challenge. To transfer and save the data at an ultrahigh speed, a SSD with a write/read/transfer speed of over 800 Mbits/s is needed: if 8192 points are acquired in each A-line for both two 12-bit channels at 50 kHz A-line speed, there will be 819.2 Megabits data coming into the SSD every second. To process this large amount of data, an advanced GPU is needed. A thorough analysis of the requirement of a GPU was described by Li et al. [25]. The speed of commercially available GPU has increased dramatically in the past five years, and this fits the need of an ultrafast IVUS-OCT system.

4 Catheter designs

Another important component of an intravascular imaging apparatus is its imaging catheter. An intravascular imaging catheter usually consists of an imaging core (probe) and an outer catheter sheath. At the tip of the imaging core, both OCT and IVUS imaging sensors are located. The catheter sheath is used outside the imaging core to avoid cross-contamination between the imaging core and the biomedical tissue. In order to avoid any catheter-induced injury to an artery and catheter-induced spasm, the outer diameter of such an imaging catheter is suggested to be smaller than 1.2 mm. Consequently, the major challenge of catheter design is to fabricate the catheter small enough and adaptable for safe routine clinical procedures while maintaining good OCT and IVUS imaging qualities.

4.1 Probe design

An integrated probe is made by assembling OCT and IVUS sub-probes. An OCT sub-probe can use either a GRIN lens, GRIN fiber or ball lens design. Either a single crystal square transducer or a ring transducer, with a center frequency at 35 MHz to 45 MHz, can serve as an IVUS sub-probe.

The foremost difficulty in making an intracoronary catheter is to make it small while maintaining its imaging quality. Usually, we want to make the IVUS and OCT sub-probes as small as possible. However, there is a trade-off between the lateral resolution and the size of a probe. If the depth of focus (DOF) is kept constant, the smaller the aperture size, the worse the lateral resolution. Thus, an optical aperture larger than 0.3 mm is commonly applied to maintain high lateral resolution and large DOF. Previously reported generations of IVUS-OCT probe designs address this issue by using different configurations and methods to minimize the IVUS or OCT sub-probes while keeping imaging quality, see Table 4.

The first demonstration of an integrated IVUS-OCT probe (see Gen 1.1 in Fig. 3) was reported in 2010 [21]. This probe used a side-by-side arrangement of IVUS and OCT sensors. A different side-by-side design which employed a common mirror to reflect the sound wave and light beam (see Gen 1.2 in Fig. 3) was published soon after this one [30]. Subsequently, a co-axial probe design (see Gen 2 in Fig. 3) was reported in which a ring IVUS transducer was used, and an OCT sub-probe was inserted inside the ring transducer [29].

The first IVUS-OCT probe capable of imaging in a coronary artery *in vivo* was demonstrated in 2011, employing a sequential configuration [22] (see Gen 3 in Fig. 3). This design enabled a smaller outer diameter than the side-by-side designs [21, 30], while using the same IVUS and OCT sub-probes and thus keeping similar imaging quality. Notably, this probe had the same outer diameter as a commercial IVUS-only probe. In 2012, a probe design (see Gen 4 in Fig. 3) very similar to the original side-by-side design was reported [23]. However, in this design, a much smaller OCT probe (0.14mm GRIN lens) was used, and there was a 90-degree difference between the exiting angles of the light beam and the sound wave.

As a matter of fact, not only is a small outer diameter important to ensure the safety of using a catheter in a coronary artery, the length of the probe rigid-part is also critical for safe operations. There are many sharp turns in the path of inserting a catheter from a femoral artery to an aorta and to a coronary artery. A probe with a short rigid-part length can be flexible and easily navigated into a coronary artery. The most recently published back-to-back design [31] (see Gen 5 in Fig. 3) addressed the strict size requirements of OD and rigid-part length at the same time. Compared with previous designs, the length of the OCT sub-probe was

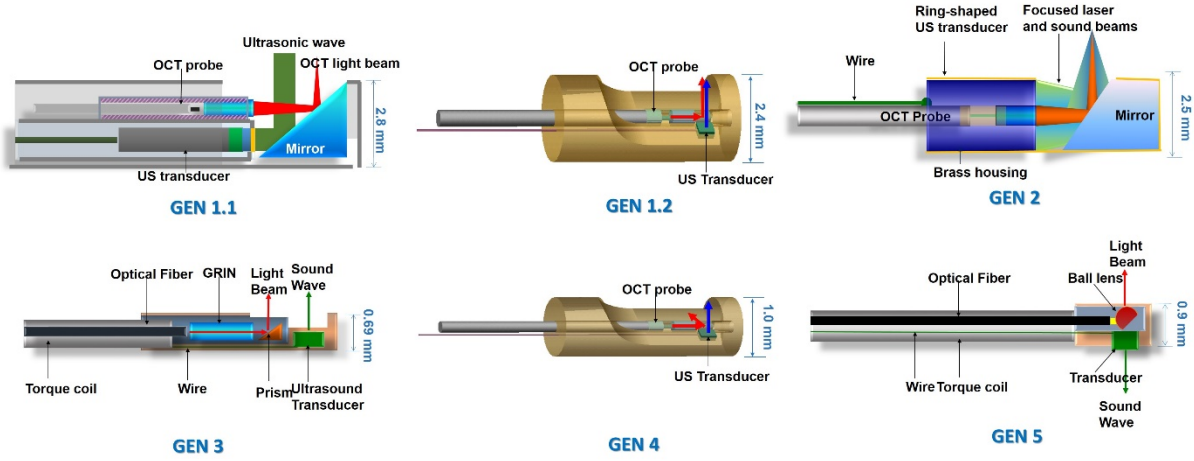


Fig. 3 Different generations of IVUS-OCT probes.

Table 4 Comparison of different generations of IVUS-OCT probes.

	Configuration	OD	Estimated rigid-part length	Size of the IVUS sub probe	Size of the OCT sub probe
Gen 1.1 [21]	Side by side	2.4 mm	5 mm	0.4 mm by 0.4 mm	0.5 mm GRIN
Gen 1.2 [30]	Side by side	2.8 mm	5 mm	0.4 mm by 0.4 mm	0.5 mm GRIN
Gen 2 [29]	Ring	2.4 mm	5.5 mm	2 mm by 5.5 mm	0.7 mm GRIN
Gen 3 [22]	Sequential	0.69 mm	4 mm	0.4 mm by 0.4mm	0.35 mm GRIN
Gen 4 [23]	Side by side	0.9 mm	2.5 mm	0.5 mm by 0.5 mm	0.14 mm GRIN
Gen 5 [31]	Back to back	0.9 mm	1.5 mm	0.4 mm by 0.4 mm	0.3 mm ball lens

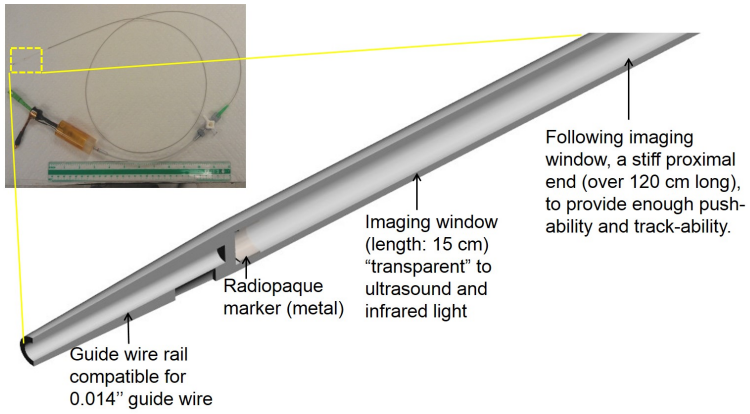


Fig. 4 Requirements of an IVUS-OCT outer sheath.

reduced by using a ball-lens design instead of a traditional GRIN lens design. The thickness of the IVUS probe was reduced by connecting the center core of a coaxial cable to the side of the backing rather than to its back surface. Although rigid-part lengths of previous generations were not reported, approximate numbers, estimated according to the sizes of IVUS and OCT sensors and published figures, are listed in Table 4 for comparison.

It is important to note that both the Gen 2 ring-transducer design [29] and Gen 5 back-to-back design [31] provide true co-axial IVUS-OCT imaging, which is not achieved by other designs.

4.2 Outer catheter sheath design

Essential considerations in making an IVUS-OCT outer catheter sheath [32] are listed in Fig.4.

It is critical to select optimal materials for the design of an outer catheter sheath. Usually, the higher the mechanical strength (thicker material or material with a higher durometer), the higher the reflection that will begenerated. To ensure the high pushability of the catheter and the high transparency of the catheter's imaging window, we used different materials for the imaging window and the proximal side of the catheter. We used a high durometer material for the proximal side to provide high pushability and trackability. A

relatively soft, low-ultrasound-attenuation material was used to reduce light and sound attenuations. These two materials were thermally bonded together to ensure a smooth transition and a strong connection between the imaging window and the proximal side.

When performing IVUS-OCT imaging *in vivo*, an X-ray C-arm and a guiding wire are used to position it smoothly into a coronary artery. Thus, radiopaque markers, a guide wire rail and a telescope design, which enable pull-back of the catheter and avoid kinking during movements, are also needed in the outer catheter sheath.

5 *In vivo* validation

After an imaging apparatus are successfully built, *in vivo* animal studies are needed to be conducted, so as to validate the safety and effectiveness of the design. The first *in vivo* demonstration of integrated IVUS-OCT was reported in 2011 by using a healthy rabbit aorta [22]. In 2014, studies showing the ability of imaging plaques and imaging coronary arteries *in vivo* were published [24, 25]. Recently, we reported ultrafast speed IVUS-OCT for *in vivo* imaging [26].

One common challenge for all *in vivo* experiments is the strong attenuation introduced by intraluminal blood. This doesn't pose a problem for *ex vivo* experiments [24, 26, 31, 33] summarized in the next section, since blood was usually drained from cadaver samples before imaging. Prior to *in vivo* imaging, an optical flushing agent is needed to be selected [34], so as to acquire clear IVUS and OCT images simultaneously, without inducing a great amount of toxicity. Since X-ray contrast agents (such as iohexol and iodixanol) are often used in patients in both IVUS and OCT procedures [35, 36], they were predicted as effective IVUS-OCT flushing agents and were commonly used in *in vivo* IVUS-OCT experiments [24-26]. However, alternative flushing agents, which have less side-effects than X-ray contrast agents and better OCT or IVUS clearing effects [34, 37-41], can be used *in vivo* experiments in future. Potential alternative flushing agents include mannitol, dextran, glucose solution and propylene glycol [42]. A high concentration of dextran was demonstrated to be useful for simultaneous IVUS-OCT imaging and could replace unsafe contrast agents [34].

A rabbit model is one of the most frequently used and successful animal models for atherosclerosis research [43]. Lesions similar to atherosclerotic plaques can be developed in the abdominal aortas of rabbits [44], where the size of artery lumen is similar to the human coronary artery lumen. A smaller animal model such as a rat cannot be utilized given the small size of its vessels and heart. Representative IVUS-OCT image pairs obtained in an atherosclerotic rabbit *in vivo* are shown in Fig. 5. Intimal thickening (see arrows in Fig. 5) can be observed by IVUS and OCT images.

Swine is another commonly used animal model for cardiovascular research. Porcine models are regularly used prior to human cardiovascular research to validate the mechanical properties (pull, torsion, flex, buckling, pull back, resistance, leaking, etc.) and clinical adaptability of catheters. In general, the cost of a pig is lower than that of a dog or primate. Pigs also have better facility acceptance and anatomical similarities than dogs. For cardiovascular research, pigs are one of the best animal models. The key reasons are: 1) a pig has a coronary artery distribution more similar to a human than other animals; 2) a pig has similar lipoproteins (critical molecules related to the atherosclerosis process) as humans; 3) the morphology and biochemistry of pig plaque is similar to that of human plaque [45]. Two representative IVUS-OCT image pairs obtained in healthy swine *in vivo* are shown in Fig. 6. In Fig. 6 Ia, an OCT image illustrates the three-layer structure of the artery wall. From the center of the OCT image, there is a high-signal thin band corresponding to the intima, followed by a high-signal strip corresponding to the external elastic lamina (EEL), and finally a low-signal area corresponding to the adventitia. Since this swine artery is healthy, there is no positive vascular remodeling. OCT is able to penetrate all three layers of the artery wall and provide a clear visualization of layers. On the contrary, the layer structure in an artery with a lipid-rich plaque (see Fig. 7) is sometimes difficult to visualize with OCT because lipid is a high attenuation source for an optical signal. In the IVUS image (Fig. 6 Ib), the three-layer structure of the swine coronary artery (wall thickness, 0.3 mm) is hardly visualized with a resolution of 60 μm. In Figs. 6 Ia and Ib, LAD branching can be visualized.

These animal studies validated that integrated IVUS-OCT is a feasible and safe technique for *in vivo* visualization of atherosclerotic plaques with high resolution and deep penetration simultaneously.

6 Clinical applications of IVUS-OCT in cardiology

IVUS-OCT has great potential for improving clinical management of cardiovascular diseases. In this section, applications where IVUS-OCT could be used to improve on current procedures will be summarized.

6.1 Classification of different plaque types

In 2006, three studies were published assessing the accuracy of IVUS or OCT using separate IVUS and OCT catheters. They all reached a similar conclusion that IVUS or OCT shows different strengths for tissue characterization of plaques, as summarized in Table 1. With the development of IVUS-OCT, the ability to classify different plaque types has been greatly improved. Figure 7 shows examples of IVUS-OCT image pairs of plaques with different compositions. In the IVUS image (Fig. 7 Ia, Fig. 7 IIa and Fig. 7 IIIa), positive vascular remodeling, i.e., intimal thickening, is identified by arrows. The total plaque volume and three-layer structure of the artery wall can also be visualized. Acoustic shadow in Fig. 7 IIa shows the location of a calcified plaque. However, it is difficult to classify the plaque types of Fig. 7 Ia and 7 IIIa from the IVUS

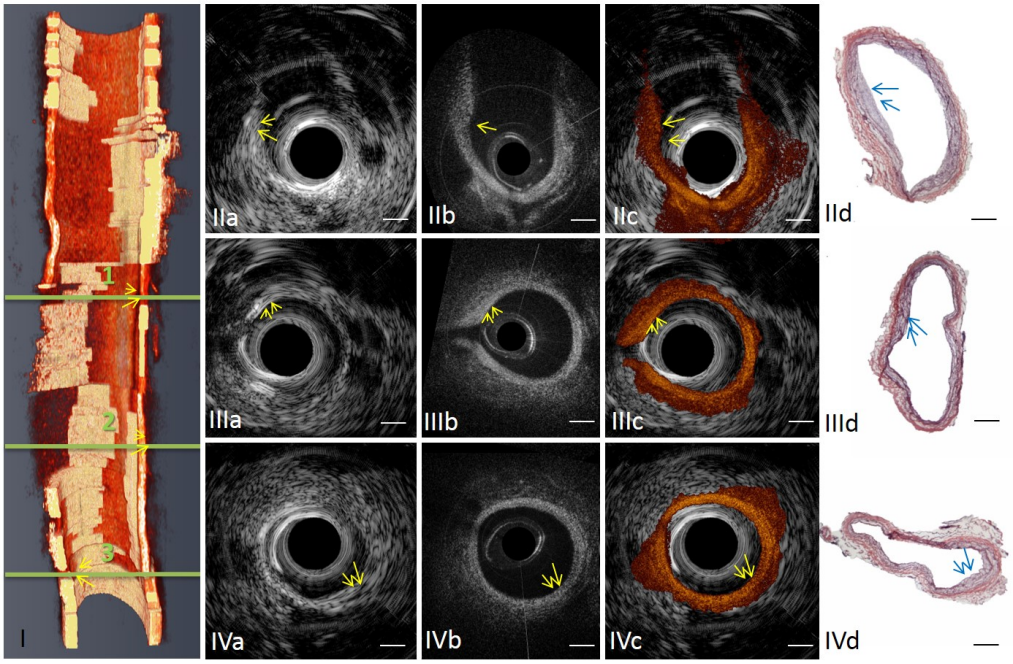


Fig. 5 IVUS-OCT imaging of a rabbit abdominal aorta *in vivo*. (I) Three-dimensional cut-away rendering of the volumetric data set acquired with an intravascular catheter in abdominal aorta of a live rabbit. The volume comprises 288 frames of images acquired in 4 s during the injection of iohexol at a rate of 3 ml/s. Red, artery wall; semi-transparent white, lipid. Circular cross-section IVUS (IIa) (IIIa) (IVa) OCT (IIb) (IIIb) (IVb) fused IVUS-OCT (IIc) (IIIc) (IVc) image pairs and the corresponding H&E histology photos (IId) (IIId) (IVd) at locations 1, 2 and 3 denoted in (I). Arrows point at lipid-rich plaque regions. Scale bar: 0.5 mm. The shape of this artery changed between *in vivo* imaging and histology due to the reduced intra-lumen pressure after this artery was harvested. Reprinted from [26], with permission.

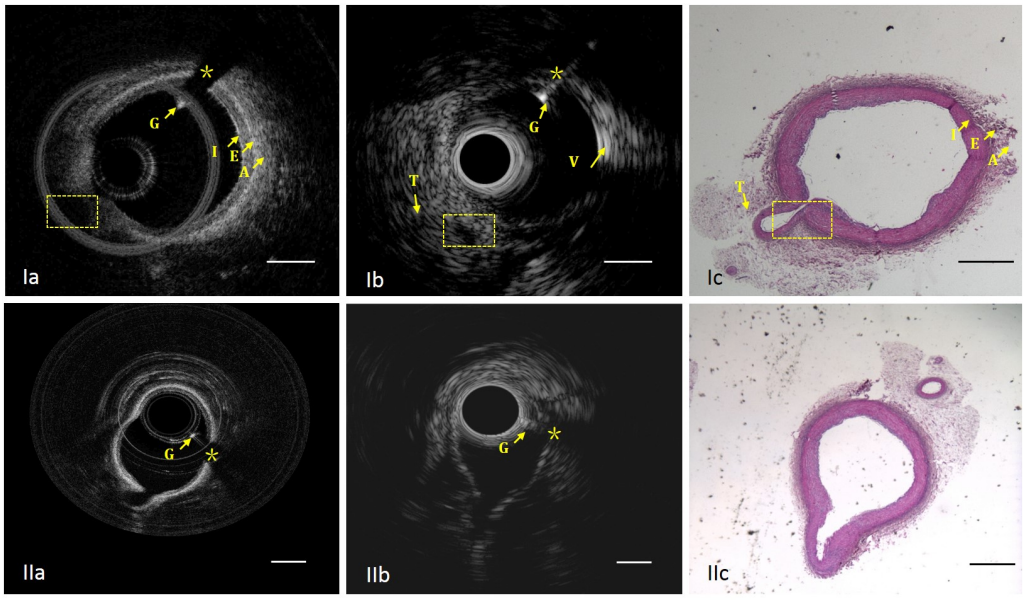


Fig. 6 An IVUS-OCT image pair obtained in a normal swine coronary artery *in vivo* during the injection of iohexol. (Ia) OCT image (Ib) IVUS image (Ic) corresponding H&E histology. Another IVUS-OCT image pair, also obtained in swine, demonstrates LAD branching. (IIa) OCT (IIb) IVUS cross-sectional image. (IIc) Corresponding H&E histology. ＊denotes guidewire artifact. G: guide wire. T: tissue. V: vessel. I: intima. E: EEL. A: adventitia. Yellow boxes denote LAD branch. Scale bar: 1mm. Row I is a reprint from [24], with permission.

images because of the intrinsically limited resolution and low soft tissue contrast. On the contrary, plaque types can be classified based on optical scattering contrast of different tissue types: 1) signal-rich regions from 3 o' clock to 6 o'clock in Fig. 7 Ib indicate a fibrous plaque; and 2) a homogenous-boundary, signal-pool region from 7 o'clock to 10 o'clock in Fig. 7 IIIb represents a lipid pool [46]. Automatic and quantitative classification of plaque types has been proposed by using algorithms [47, 48]. On the other hand, with limited penetration depth, OCT image cannot provide a clear visualization of media and adventitia layers at this intima-thickening coronary segment. The corresponding histology images (Fig. 7 Ic, Fig. 7 IIc and Fig. 7 IIIc) are stained with hematoxylin and eosin (H&E). Cells with abundant pale, vesicular cytoplasm and bland nuclei (Fig. 7 IIIc) are lipid-laden foamy macrophages which are also confirmed by positive stain in the CD 68 slide. The dense, compact eosinophilic fibers (Fig. 7 Ia) represent increased amounts of collagen seen in a fibrous plaque. These histology results confirm the classification of plaque types by the IVUS-OCT images.

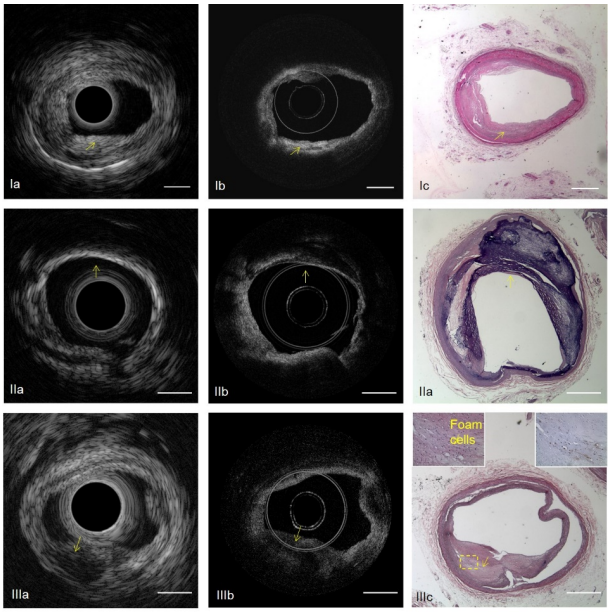


Fig. 7 Imaging of a coronary artery with a fibrous plaque (top row), a calcified plaque (middle row) and lipid plaque (bottom row). (Ia)(IIa)(IIIa) IVUS, (Ib)(IIb)(IIIb) OCT images, and (Ic)(IIc)(IIIc) corresponding histology image. Insets in (IIIc), high magnified images of the histology slides. Left inset, stained with H&E; right inset, stained with CD68. Arrows denote the location of plaques. Scale bar: 1mm. Reprinted from [24], with permission.

Similarly, the ability to differentiate necrotic, calcified and fibrotic tissues was also evaluated in other studies [13, 31]. Quantitatively, the diagnostic accuracy comparison of IVUS-OCT diagnosis, with IVUS-only diagnosis and OCT-only diagnosis was conducted by using 241 plaque regions [33]. It was concluded that the use of IVUS and OCT is superior to IVUS-only and OCT-only diagnosis for detection and characterization of coronary atherosclerotic plaques with high degree of sensitivity and specificity. In summary, IVUS-OCT shows promise to provide more accurate detection of different plaque types.

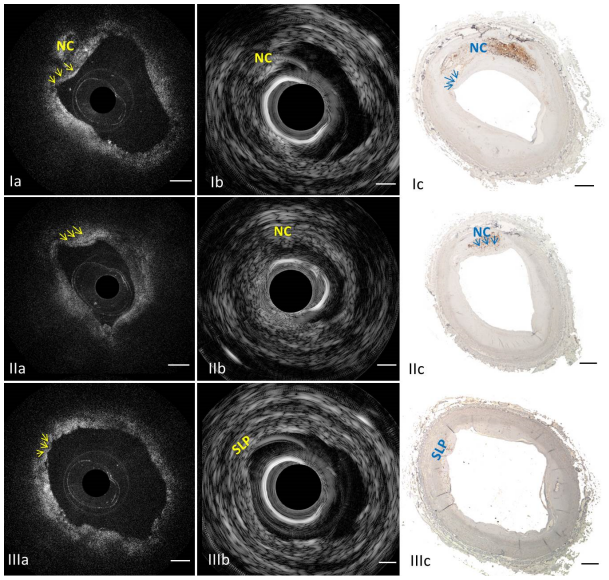


Fig. 8 Identification of vulnerable plaques by integrated IVUS-OCT system. First row: Example of a vulnerable plaque. (Ia) OCT image in which arrows point at the fibrous cap; (Ib) corresponding IVUS image indicates the location of necrotic core; (Ic) photo of the corresponding histology slide with CD 68 stain, highlighting macrophages and necrotic core. Middle row: A false positive case of vulnerable plaque diagnosis based on IVUS-only (IIb) was produced due to the insufficient resolution and sensitivity. Size of the thick cap can be determined by the corresponding OCT (IIa) and CD 68 histology (IIc). Bottom row: A false positive case of vulnerable plaque diagnosis based on OCT-only (IIIa) was produced due to OCT's limited penetration depth. A small lipid pool can be determined by IVUS (IIIb) and CD 68 histology (IIIc). Arrows denote the fibrous cap. NC: necrotic core; SLP: small lipid pool. Scale bar: 0.5 mm. Reprinted from [26], with permission.

Accurate diagnosis of different plaque types is the first and foremost step for discerning a vulnerable plaque in which there is a core filled with necrotic tissues and a cap filled with fibrotic tissues.

6.2 Identification of vulnerable plaques

IVUS-OCT has the potential to address the need to identify vulnerable plaque in patients. Examples of vulnerable plaque and false vulnerable plaques, obtained by using an integrated IVUS-OCT system, are shown in Fig. 8. A vulnerable plaque can be easily diagnosed, as shown in the first row of Fig. 8. Arrows in the OCT image (Fig. 8 Ia) denote the thin fibrous cap while the size of the necrotic core can be estimated using the IVUS image (Fig. 8 Ib). In Fig. 8 IIb,

physicians diagnosed this ROI as vulnerable plaques when only reading the IVUS image. This misdiagnosis was caused by the insufficient resolution and sensitivity of IVUS. However, using the OCT image as the reference (see Fig. 8 IIa), a signal low region with diffuse boundary (i.e., lipid plaque) could be visualized and the thickness of signal high region (fibrous cap) could be measured to be greater than 65μm. In Fig. 8 IIIa, physicians diagnosed this ROI as vulnerable plaques when only reading the OCT image. This misdiagnosis was caused by OCT's limited penetration depth. However, using the IVUS image as the reference (see Fig. 8 IIIb), the small size of the lipid pool could be visualized.

6.3 Evaluation of stent implantation

IVUS-OCT images of a stent in a coronary artery is shown in Fig. 9. The 3D reconstruction of the entire pullback is shown in Figs. 9 IIa and IIb. There are two points in the clinical workflow where IVUS-OCT may play a key role in improving clinical outcomes: before and after stenting. IVUS-OCT may bring new insights into optimizing the selection and placement of stents and minimizing side effects.

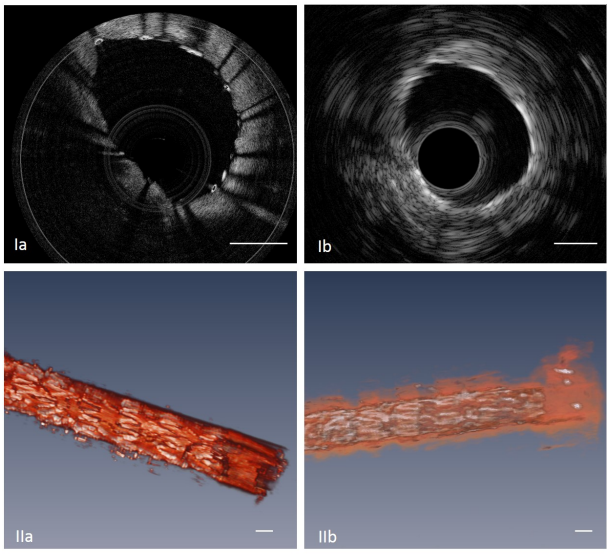


Fig. 9 IVUS-OCT imaging of a coronary artery with a stent implanted. OCT (Ia) IVUS (Ib) images, and OCT (IIa) IVUS (IIb) 3D rendering of a human coronary artery specimen with a stent. In (IIa) and (IIb), the white color coded places are stent struts and the red coded places are coronary artery tissue. Scale bar: 1mm.

In the previous section, the ability to accurately differentiate plaque types was discussed. Information, such as plaque compositions and lumen dimensions that are evaluated by IVUS-OCT, can assist cardiologists in optimizing the treatment plan. For instance, 1) heavily calcified lesions usually require more pressure to generate an adequate stent expansion than a softer lesion; 2) a lipid rich region is not a good landing point for a stent; 3) knowing the length of the lesion and the size of the lumen can help the physician select the optimal stent to use.

IVUS-OCT also provides important information after stenting, such as (1) evidence of inadequate stent expansion or strut apposition; (2) evidence of associated extensive vessel damage; and (3) evidence of the characteristics of neointimal hyperplasia in previously implanted stents [49]. Notably, there is a study that concluded that the best indicator to predict stent thrombosis, a deadly risk of stenting, was the ratio of uncovered to total stent struts [50]. By using IVUS-OCT, visualization of stent struts and the surrounding tissues, with OCT's high resolution (to recognize uncovered struts and neoatherosclerosis that are not detectable by IVUS) [51] and IVUS's deep penetration depth (to image stents out of OCT image range or depth), can be achieved. IVUS and OCT provide complementary diagnostic values and may potentially contribute as a clinical benefit for patients [12, 52].

6.4 Other clinical applications

IVUS-OCT can also provide clinically valuable, complementary information for some other applications. For example, spontaneous coronary artery dissection is a disease that induces acute heart attack, but cannot be predicted and then prevented by using typically heart disease risk factors. Intravascular imaging is needed to make definitive diagnosis for this disease [53-55]. OCT was reported to allow the recognition of intimal tear while IVUS enables analysis of structures which are beyond the image range or depth of OCT, such as side branches, 3-layered membranes and dorsal structures [56].

7 Future directions

Since the first development and demonstration of integrated IVUS-OCT technology in 2010 [21, 30], many technical breakthroughs have been achieved in the past 5 years. However, more research and validation are required before this technology can be implemented into the daily clinical routine. The first and foremost step to achieve this goal is evaluating the diagnostic accuracy of IVUS-OCT in patient, which, however, is extremely costly. Due to the invasive nature of the technology and the vulnerability of coronary arteries (at where the imaging is performed), the *in vivo* human evaluation of this technology is classified as a significant risk and thus requires FDA approval for human study to be conducted in any U.S. research institute. The FDA approval requires significant resources for research institutes to perform such a clinical study. However, the involvement of medical device companies holds promise in overcoming this challenge. With an increased number of countries beginning to reimburse intravascular catheters and the fast growth of the Asia-Pacific market, the global market for IVUS itself has reach $483.7 million in 2012 and is expected to reach $702 million in 2017 (for a compound annual growth rate of 7.7%) [57]. This fast

growth encourages and enables more and more medical device companies to invest in new intravascular technologies, such as IVUS-OCT.

Another future direction of IVUS-OCT technology is to derive other imaging modalities from it and/or to combine with other imaging techniques so as to make it more powerful in identifying vulnerable plaques. The knowledge gained in developing IVUS-OCT technology can benefit a range of new imaging methods, such as intravascular photoacoustic (IVPA) and acoustic radiation force optical coherence elastography (ARFOCE). IVPA is expected to provide stronger chemical contrast to accurately identify lipid cores while ARFOCE holds potential to predict the rupture of a plaque by analyzing the stress generated by its necrotic pool.

Both IVUS and OCT signals are generated by detecting the scattering information of different plaque compositions. However, the scattering pattern produced by lipids may look similar to what is generated by another chemical composition. The diagnostic accuracy of IVUS in detecting lipid is limited [4]. Thus, a more accurate detection of the chemical composition of plaques may be of great interest to physicians. Near infrared spectroscopy (NIRS), which detects different molecules by their unique absorption properties, is currently under investigation in large-scale clinical studies [58, 59]. There is, however, a fundamental limitation. NIRS only provides 2D imaging of a coronary artery. To provide a 3D map of chemical compositions of a plaque, a trend of using PA for intravascular imaging has been seen in recent publications [60-64]. Although *in vivo* validation of IVPA in animals remains limited [61], we can expect a fast growth of IVPA in the near future by adopting the technical advancements of IVUS-OCT.

From a mechanical perspective, the rupture of a plaque happens when the stress on the plaque exceeds its tensile strength. The stress in the cap increases with decreasing thickness of the fibrous cap and increasing lipid-core burden. Thus, elastography, which assesses the mechanical properties, offers the opportunity to evaluate plaque vulnerability by analyzing its mechanical behavior. Several elastography technologies have been developed or are in development, such as ultrasound, MRI, laser speckle or OCT-based ones. The spatial resolutions of elastography techniques are determined by the underlying imaging modality. Accordingly, OCT-based elastography can provide much better resolution than MRI and US-based elastography [65-68]. To generate elastography, mechanical excitation of a tissue is required. The traditional excitation approach which compresses the subject statically/quasi-statically has limited imaging speed for *in vivo* imaging. Recently, ARFOCE was proposed [68-70], which use a dynamic excitation method. This novel technology enables a much higher imaging speed and makes it possible for *in vivo* imaging. When developing ARFOCE, we can borrow insights obtained in advancing IVUS-OCT technology since ARFOCE and IVUS-OCT both use ultrasound and OCT. It is promising that ARFOCE can be used intravascularly in the next couple of years to evaluate the mechanical property of a plaque.

8 Conclusion

The integrated IVUS-OCT technology is a powerful tool for diagnosing and characterizing vulnerable plaque. Since the first demonstration of IVUS-OCT in 2010, significant advances have been made. The fundamental challenge of IVUS-OCT technology has been overcome, and the speed of a fully-synchronized integrated system is now fast enough for safely imaging coronary arteries *in vivo*. Advancements have also been completed in catheter design: the imaging probe can be fabricated small enough for intracoronary imaging while the imaging quality is well maintained. *In vivo* animal studies validated the safety and effectiveness of this technology. *Ex vivo* studies using human coronary specimens demonstrated potential clinical applications of IVUS-OCT. Future directions of this technology include performing *in vivo* human studies and developing derivative imaging modalities.

Acknowledgments

We would like to thank many of our colleagues who have contributed to the intravascular imaging project the UCI Beckman Laser Institute, The Edwards Lifesciences Center for Advanced Cardiovascular Technology, Department of Biomedical Engineering, and School of Medicine, particularly Dr. P. M. Patel and his team at the UCI Division of Cardiology. In addition, we would like to thank our collaborators, Drs. Q. Zhou and K. K. Shung, as well as their students the USC NIH Ultrasonic Transducer Resource Center and Department of Biomedical Engineering, for miniature ultrasound transducers for the intravascular imaging project. Finally, this work was supported by the National Institutes of Health under grants R01-HL-125084, R01-HL-127271, R01-HL-105215, R01-EY-021529, P41-EB-002182, P41-EB-015890. Dr. Zhongping Chen has a financial interest in OCT Medical Inc., which, however, does not support this work.

Biophysical approach to the correction of supporting tissue microcirculation impairments

Sergey I. Kireev[1,2*], Aslan M. Imamov[2], Alexander G. Kurmanov[2]

[1] Saratov State University n.a. N.G. Chernyshevsky, 83 Astrahaskaja str., Saratov 410012, Russia

[2] Saratov State Medical University n.a. V. I. Razumovsky, 112 B. Kazachya str., Saratov 410012, Russia

[*] **e-mail:** kireevsi@rambler.ru

Abstract. By experimental and histological methods it was estimated that application of terahertz –frequency electro-magnetic radiation at 150,176 – 150,664 GHz frequency at the background of acute and chronic immobilization stress contributes to the decrease of occurrence incidence of microcirculation impairments in the bone tissue and red bone marrow. The presented findings give the grounds to assume that terahertz – frequency electro-magnetic radiation at the frequency of molecular spectrum absorption and radiation of nitrogen oxide may be recommended as a valid and effective method in the complex treatment of patients with orthopedo-traumatological pathology. © 2016 Samara State Aerospace University (SSAU).

Keywords: electromagnetic radiation, terahertz range, nitric oxide, bone tissue, microcirculation, immobilization stress, skeletal trauma, orthopedics pathology.

Paper #2710 received 2015.10.29; revised manuscript received 2015.12.15; accepted for publication 2015.12.25; published online 2016.02.01.

References

1. O. V. Betsky, and N. N. Lebedeva, "Application of Low – Intensive Millimeter Waves in Biology and Medicine," Biomedical Radioelectronics 8-9, 6-25 (2007).
2. S. I. Kireev, Electro-magnetic Terahertz waves as the factor of the correction of supporting tissue microcirculation impairments (experimental-clinical research), Dissertation for the degree of doctor of medical sciences, Saratov (2011).
3. S. I. Kireev, "Electro-magnetic Terahertz waves as the factor of the correction of supporting tissue microcirculation impairments (experimental – clinical research)," Author's abstract of medical sciences doctoral dissertation, Saratov (2011).
4. S. I. Kireev, Biophysical Correction of Supporting Tissue Microcirculation Impairments (experimental-clinical research), Palmarium academic publishing (2012).
5. D. R. Lowrens, and P. N. Benitt, Clinical pharmacology, 1st ed., Moscow (1993). ISBN: 5-225-00491-1.
6. F. Murad, "Nitric oxide - biogeneration, regulation, and relevance to human diseases," Frontiers in Bioscience 8(1-3), 264-278 (2003).
7. B. Fagrell, and M. Intaglietta, "Microcirculation: its significance in clinical and molecular medicine," J. Intern. Medicine 241(5), 349-362 (1997).
8. R. F. Furchgott, and D. Jothianandan, "Endothelium-dependent and –independent vasodilation involving cyclic GMP: relaxation induced by nitric oxide, carbon monoxide and light," Blood Vessels 28(1-3), 52-61 (1991).

1 Introduction

In traumas of the supportive-locomotive system hemostasis is impaired at macro- and microlevels due to the effect of an extreme factor. One of the basic pathogenetic units determining the markedness of catabolic processes in the bone tissue during the nearest post-traumatic period, is the impairment of microcirculation [4,7]. Recently, the most commonly used medicamentous correction of microcirculation impairments includes treatment with anticoagulants, non-steroid anti-inflammation agents and desaggregants [5]. The presence of contraindications to the use of these preparations or the lack of the desired effect of their usage [5] prove the necessity to search for new methods

(including non-medicamentous ones) of microcirculation impairments' correction.

One of effective methods aimed to improve microcirculation in the damaged tissues is short-wave-frequency (SWF) therapy widely used in orthopedo-traumatological practice [2,3]. According to the opinion of a number of researchers, the study of the effect of terahertz –frequency (THF) radiation on microcirculation at the frequency of molecular spectrum absorption and radiation of nitrogen oxide (MSARNO) – a neurotransmitter, powerful hemostasis factor, thrombocyte aggregation inhibitor, endogenic vasodilator, - is, at the moment, of great scientific and practical interest [1,2,3,6,8]. Some investigations present the findings which prove the positive effect of electro-magnetic radiation (EMR) of THF range at MSARNO frequency on rheological properties of blood [1].

The aim of the present investigation is to study EMR THF MSARNO application effectiveness for correction of microcirculation impairments in the bone tissue.

2 Methods of the investigation

This work was based on the experimental method of investigation. The experiments were carried out on 135 white non-bred male rats of 180 – 220 g of weight. The animals were kept in standard vivarium conditions. Experimental studies were performed according to the principles of laboratory practice of the Russian Federation, and according to the requirements of Geneva Convention «International Guiding Principles for Biomedical Research Involving Animals» (Geneva, 1990). The experiments were carried out in a separate laboratory excluding outside effects, dietary errors, at constant air temperature of 18 – 22 0C, with standard levels of light and moisture, unification of seasonal and daily cycles.

Microcirculation impairments were modelled by means of immobilization stress: in acute stress variant – maximum fixation of the rats on the back for 3 hours, in chronic stress variant - maximum fixation of the rats on the back during 5 days for 3 hours a day.

The study consisted of 9 series of experiments, each including 15 animals. In the 1-st series acute immobilization stress without additional outside effects was modelled. In the next 3 series the animals were radiated with EMR THF MSARNO (150,176 – 150,66 GHz) at the background of acute immobilization stress. The source of radiation was placed at the distance of 1,5 cm from the skin surface of 3 cm² area above the sternal region (power density was 0,2 mWt/ cm²). In the 2-nd series the duration of radiation was 5 minutes, in the 3-d - 15 minutes, in the 4-th – 30 minutes. In the 5-th series chronic immobilization stress without additional outside effects was modelled. In the 6-th – 8-th series the animals were radiated with EMR THF MSARNO at the background of chronic immobilization stress. The duration of radiation was 5, 15, 30 minutes in the 6-th, 7-th and 8-th series respectively. The 9-th series of the experiment was intact control. At the end of the experiment the animals were decapitated in accordance to the basic principles of euthanasia. Series of cytological and histological samples of blood, red bone marrow (RBM), breastbone, femoral bones were prepared. The serial samples were stained with hematoxylin and eosine, according to Romanovsky – Gimse technique, with toluidine blue solution.

When studying the obtained preparations the presence and markedness of various signs, characterizing impairments in the vascular, intravascular and extravascular units of the microcirculation channel of the bone tissue and red bone marrow, were taken into consideration.

3 Results and discussion

It was established that in immobilization stress (to greater extent – in chronic, to lesser extent – in acute) the most significant changes occurred in capillaries and post-capillaries, where the signs of stasis, aggregation and sludge of the blood formed elements were noted. Leucocyte adhesion, high edgt position of the laminar vessels' surface with migration to the perivascular region were observed in the venules. In the system of the microcirculation channel the picture of amorphic – type sludge (according to V.V.Kuprianov, 1969) was formed. Parietal areas contained thrombocytic groups which gave the evidence of the tendency to thromboformation. All the above mentioned changes caused stasis in post-capillary-venular section, reduction of a significant amount of capillaries, which lost their functional properties. All units of the microcirculation channel were subjected to pathological transformation. Changes in smooth muscular and endothelial cells of the vessels aggravated and were accompanied by metachromasia, masaic hyperchromasia; signs of dystrophy of all cellular elements, connective tissue fibers and perivascular structures became more pronounced, - all these changes were accompanied by intensification of deformation of the vessels' contours. Alongside the passage of the vessels of metabolic and refluence units of the microcirculation channel all the objects of the investigation (the bone tissue and red bone marrow) showed aggravated perivascular edema, cell infiltration, which were caused by the increase of the vascular wall permeability. The number of the network capillaries with the formation of loop-shaped capillary complexes and extensive avascular regions was significantly reduced. The red bone marrow in the animals of the 5-th group looked like that consisting predominantly of cells, hemopoietic cells were arranged into islands, stroma elements were poorly differentiated. There were revealed the signs of dystrophy; a significant amount of stroma cells; the number of hemopoietic activity foci was significantly reduced; the number of cells in some islands was decreased, in other islands the reduction of the red bone marrow was observed. In the animals subjected to the effect of acute immobilization stress the incidence of impairments in intravascular and vascular microcirculation units was significantly close to the analogous indices observed in

chronic stress modelling. In particular, vascular dystonia occurred in all the animals in both acute and chronic stress. Under the influence of acute immobilization stress extravascular microcirculation impairments of the bone tissue and red bone marrow occurred 1,5 – 1,7 times more rarely as compared to the effect of chronic stress. In acute stress intravascular microcirculation impairments also occurred 1,2 – 1,4 times more rarely as compared to chronic stress. In particular, erythrocyte hemolysis in acute stress modelling was noted in 1/3 of the experimental animals, while in chronic stress it was observed in almost half of the cases (Table 1).

Table 1 Relative incidence (%) of occurrence of the signs of microcirculation impairments in the bone tissue and red bone marrow of experimental animals at acute and chronic immobilization stress modelling.

Unit of microcirculation channel (number of the signs analyzed)	**Acute immobilization stress (n=15)**	**Chronic immobilization stress (n=15)**
Vascular unit (8 signs)	76,6%	91,6%
Intravascular unit (8 signs)	75%	93,3%
Extravascular unit (5 signs)	70,6%	97,3%

There was noted practically equal decrease of the incidence of the impairments' occurrence in all three units of the microcirculation channel in the bone tissue and red bone marrow in the animals subjected to the influence of acute immobilization stress at the background of radiation during 5 minutes and 30 minutes as compared to the effect of acute stress without radiation (Table 2).

Table 2 Relative incidence (%) of occurrence of the signs of microcirculation impairments in the bone tissue and red bone marrow of experimental animals at the modelling of acute immobilization stress at the background of radiation with EMR THF 150,176-150,664 GHz.

Unit of microcirculation channel (number of the signs analyzed)	**Duration of radiation with EMR THF 150,176-150,664 GHz**		
	5 minutes (n=15)	**15 minutes (n=15)**	**30 minutes (n=15)**
Vascular unit 8 signs)	55%	7,5%	46,6%
Intravascular unit (8 signs)	44,2%	2,5%	35,8%
Extravascular unit (5 signs)	41,3%	4%	32%

Besides, the incidence of occurrence of the majority of the signs of microcirculation impairments at 30 – minute radiation was less as compared to 5 – minute radiation regimen (Table 2). In the animals subjected to the influence of acute immobilization stress at the background of 15 – minute radiation, practically complete normalization of the bone tissue and red bone marrow microcirculation conditions was noted in accordance with zero indices of the incidence of occurrence of the majority of the corresponding signs. Moreover, the incidence of occurrence of some signs of microcirculation impairments (dystonia and swelling of the vascular wall, focal perivascular edema, interstitial edema, poikilocytosis) in the animals of that experimental series did not exceed 1/5.

The analysis of the impairments' incidence in intravascular, vascular and extravascular units of the bone tissue and red bone marrow microcirculation channel in the animals subjected to the effect of chronic immobilization stress made it possible to establish significantly equal decrease of that index at the background of 5 – minute and 30 – minute radiation. Besides, when comparing the corresponding indices between the above mentioned experimental series of the animals, there was noted the tendency to more pronounced decrease of the incidence of occurrence of the majority of signs of microcirculation impairments at 30 – minute radiation as compared to 5 – minute radiation (Table 3).

Table 3 Relative incidence (%) of occurrence of the signs of microcirculation impairments in the bone tissue and red bone marrow of experimental animals at the modelling of chronic immobilization stress at the background of radiation with EMR THF 150,176-150,664 GHz.

Unit of microcirculation channel (number of the signs analyzed)	**Duration of radiation with EMR THF 150,176-150,664 GHz**		
	5 minutes (n=15)	**15 minutes (n=15)**	**30 minutes (n=15)**
Vascular unit (8 signs)	50%	26,6%	45%
Intravascular unit (8 signs)	45%	17,5%	38,3%
Extravascular unit (5 signs)	62,6%	30,6%	52%

The animals under chronic immobilization stress at the background of 15 – minute radiation, as compared to other experimental series of chronic stress modelling, demonstrated maximum degree of correction of microcirculation impairments in the bone tissue and red bone marrow, in accordance to the minimal incidence indices of the majority of corresponding signs. The incidence of occurrence some signs of microcirculation impairments (dystonia and swelling of the vascular wall, focal perivascular edema, capillary network reduction; metachromasia of Haversian canals' elements; bone matrix acidophilia) in the animals of that experimental series did not exceed 1/3, the signs of erythrocyte hemolysis were noted in none of the cases.

4 Conclusion

Application of radiation with EMR THF at 150,176-150,664 GHz frequency at the background of acute and chronic immobilization stress contributes to the decrease of occurrence incidence of microcirculation impairments in the bone tissue and red bone marrow. It has been established that in experimental conditions the effect of EMR THF at the frequency of molecular spectrum of absorption and radiation of nitrogen oxide (150,176-150,664 GHz) on microcirculation impairments in the supporting tissues under immobilization stress depends on the radiation duration. The highest degree of correction of the supporting tissue microcirculation impairments is reached by application of 15-minute radiation duration.

The presented findings give the grounds to assume that EMR THF MSARNO may be recommended as a valid and effective method in the complex treatment of patients with orthopedo-traumatological pathology.

Assessing mechanical properties of tissue phantoms with non-contact optical coherence elastography and Michelson interferometric vibrometry

Jiasong Li[1], Chih-Hao Liu[1], Alexander Schill[1], Manmohan Singh[1], Achuth Nair[1], Valery P. Zakharov[2], and Kirill V. Larin[1,2,3*]

[1] Department of Biomedical Engineering, University of Houston, TX, 77204, USA
[2] Department of Laser and Biotechnical Systems, Samara State Aerospace University, Samara, 443086, Russia
[3] Department of Molecular Physiology and Biophysics, Baylor College of Medicine, TX, 77030, USA

[*] **e-mail**: klarin@central.uh.edu

Abstract. *Purpose*: Elastography is an emerging method for detecting the pathological changes in tissue biomechanical properties caused by various diseases. In this study, we have compared two methods of noncontact optical elastography for quantifying Young's modulus of tissue-mimicking agar phantoms of various concentrations: a laser Michelson interferometric vibrometer and a phase-stabilized swept source optical coherence elastography system. *Methods*: The elasticity of the phantoms was estimated from the velocity of air-pulse induced elastic waves as measured by these two techniques. *Results*: The results show that both techniques were able to accurately assess the elasticity of the samples as compared to uniaxial mechanical compression testing. *Conclusion*: The laser Michelson interferometric vibrometer is significantly more cost-effective, but it cannot directly provide the elastic wave temporal profile, nor can it offer in-depth information. © 2016 Samara State Aerospace University (SSAU).

Keywords: optical coherence elastography, optical coherence tomography, laser Michelson interferometric vibrometer, elasticity, elastic wave, air-pulse, non-contact.

Paper #2809 received 2015.12.10; revised manuscript received 2015.12.25; accepted for publication 2015.12.30; published online 2016.02.01.

References

1. J. F. Greenleaf, M. Fatemi, and M. Insana, "Selected methods for imaging elastic properties of biological tissues," Annu Rev Biomed Eng 5, 57-78 (2003).
2. M. C. Chirambo, and D. Benezra, "Causes of blindness among students in blind school institutions in a developing country," Br J Ophthalmol 60(9), 665-8 (1976).
3. M. J. Paszek, N. Zahir, K. R. Johnson, J. N. Lakins, G. I. Rozenberg, A. Gefen, C. A. Reinhart-King, S. S. Margulies, M. Demb, D. Boettiger, D. A. Hammer, and V. M. Weaver, "Tensional homeostasis and the malignant phenotype," Cancer Cell 8(3), 241-54 (2005).
4. S. J. Zieman, V. Melenovsky, and D. A. Kass, "Mechanisms, pathophysiology, and therapy of arterial stiffness," Arterioscler Thromb Vasc Biol 25(5), 932-43 (2005).
5. J. S. Pepose, S. K. Feigenbaum, M. A. Qazi, J. P. Sanderson, and C. J. Roberts, "Changes in corneal biomechanics and intraocular pressure following LASIK using static, dynamic, and noncontact tonometry," Am J Ophthalmol 143(1), 39-47 (2007).
6. K. J. Parker, and R. M. Lerner, "Sonoelasticity of organs: shear waves ring a bell," J Ultrasound Med 11(8), 387-92 (1992).
7. R. Muthupillai, D. J. Lomas, P. J. Rossman, J. F. Greenleaf, A. Manduca, and R. L. Ehman, "Magnetic resonance elastography by direct visualization of propagating acoustic strain waves," Science 269(5232), 1854-7 (1995).

8. M. D'Onofrio, A. Gallotti, and R.P. Mucelli, "Tissue quantification with acoustic radiation force impulse imaging: Measurement repeatability and normal values in the healthy liver," AJR Am J Roentgenol 195(1), 132-6 (2010).
9. J. Bercoff, M. Tanter, and M. Fink, "Supersonic shear imaging: a new technique for soft tissue elasticity mapping," IEEE Trans Ultrason Ferroelectr Freq Control 51(4), 396-409 (2004).
10. G. Grabner, R. Eilmsteiner, C. Steindl, J. Ruckhofer, R. Mattioli, and W. Husinsky, "Dynamic corneal imaging," J Cataract Refract Surg 31(1), 163-74 (2005).
11. K. W. Hollman, S. Y. Emelianov, J. H. Neiss, G. Jotyan, G. J. Spooner, T. Juhasz, R. M. Kurtz, and M. O'Donnell, "Strain imaging of corneal tissue with an ultrasound elasticity microscope," Cornea 21(1), 68-73 (2002).
12. M. Tanter, D. Touboul, J. L. Gennisson, J. Bercoff, and M. Fink, "High-resolution quantitative imaging of cornea elasticity using supersonic shear imaging," IEEE Trans Med Imaging 28(12), 1881-93 (2009).
13. C. Li, Z. Huang, and R. K. Wang, "Elastic properties of soft tissue-mimicking phantoms assessed by combined use of laser ultrasonics and low coherence interferometry," Opt Express 19(11), 10153-63 (2011).
14. S. Wang, K. V. Larin, J. Li, S. Vantipalli, R. K. Manapuram, S. Aglyamov, S. Emelianov, and M. D. Twa, "A focused air-pulse system for optical-coherence-tomography-based measurements of tissue elasticity," Laser Phy Lett 10(7), 075605 (2013).
15. G. Scarcelli, and S. H. Yun, "In vivo Brillouin optical microscopy of the human eye," Opt Express 20(8), 9197-202 (2012).
16. G. Scarcelli, P. Kim, and S. H. Yun, "In vivo measurement of age-related stiffening in the crystalline lens by Brillouin optical microscopy," Biophys J 101(6), 1539-45 (2011).
17. J. Schmitt, "OCT elastography: imaging microscopic deformation and strain of tissue," Opt Express 3(6), 199-211 (1998).
18. S. Wang, and K. V. Larin, "Optical coherence elastography for tissue characterization: a review," J Biophotonics 8(4), 279-302 (2015).
19. D. Huang, E. A. Swanson, C. P. Lin, J. S. Schuman, W. G. Stinson, W. Chang, M. R. Hee, T. Flotte, K. Gregory, C. A. Puliafito, and J. G. Fojimoto, "Optical coherence tomography," Science 254(5035), 1178-81 (1991).
20. M. Sticker, C. K. Hitzenberger, R. Leitgeb, and A. F. Fercher, "Quantitative differential phase measurement and imaging in transparent and turbid media by optical coherence tomography," Opt Lett 26(8), 518-20 (2001).
21. S. Wang, J. Li, R. K. Manapuram, F. M. Menodiado, D. R. Ingram, M. D. Twa, A. J. Lazar, D. C. Lev, R. E. Pollock, and K. V. Larin, "Noncontact measurement of elasticity for the detection of soft-tissue tumors using phase-sensitive optical coherence tomography combined with a focused air-puff system," Opt Lett 37(24), 5184-6 (2012).
22. X. Zhang, and J. F. Greenleaf, "Estimation of tissue's elasticity with surface wave speed," J Acoust Soc Am 122(5), 2522-5 (2007).
23. Z. Han, J. Li, M. Singh, C. Wu, C. H. Liu, S. Wang, R. Idugboe, R. Raghunathan, N. Sudheendran, S. R. Aglyamov, M. D. Twa, and K. V. Larin, "Quantitative methods for reconstructing tissue biomechanical properties in optical coherence elastography: a comparison study," Phys Med Biol 60(9), 3531-47 (2015).
24. L. Drain, The laser Doppler technique, John Wiley, Chichester, 186-194 (1980). ISBN: ISBN 0-471-27627-8.
25. P. Castellini, G. Revel, and E. Tomasini, "Laser Doppler vibrometry: a review of advances and applications," The Shock and vibration digest 30(6), 443-456 (1998).
26. G. R. Ball, A. Huber, and R. Goode, "Scanning laser Doppler vibrometry of the middle ear ossicles," Ear Nose Throat J 76(4), 213-222 (1997).
27. J. Sokołowski, K. Niemczyk, R. Bartoszewicz, K. Morawski, A. Bruzgielewicz, and B. Rygalska, "Round window's movability measurements with helping of LDV in evaluation of ossicular chain functioning," Otolaryngol Pol 64(7), 77-80 (2010).
28. B. Felver, D. C. King, S. C. Lea, G. J. Price, and A. D. Walmsley, "Cavitation occurrence around ultrasonic dental scalers," Ultrason Sonochem 16(5), 692-7 (2009).
29. S. C. Lea, A. D. Walmsley, P. J. Lumley, and G. Landini, "A new insight into the oscillation characteristics of endosonic files used in dentistry," Phys Med Biol 49(10), 2095-102 (2004).
30. M. De Melis, U. Morbiducci, and L. Scalise, "Identification of cardiac events by optical Vibrocardiograpy: comparison with Phonocardiography," Conf Proc IEEE Eng Med Biol Soc 2007, 2956-9 (2007).
31. U. Morbiducci, L. Scalise, M. De Melis, and M. Grigioni, "Optical vibrocardiography: a novel tool for the optical monitoring of cardiac activity," Ann Biomed Eng 35(1), 45-58 (2007).
32. L. Scalise, and U. Morbiducci, "Non-contact cardiac monitoring from carotid artery using optical vibrocardiography," Med Eng Phys 30(4), 490-7 (2008).
33. D. Rixen, and T. Schuurman, "In Vivo Measurement of the Human Thorax and Abdomen Surface Using Laser Vibrometry: A New Diagnostic Tool?" in Topics in Modal Analysis II, Volume 6, Springer, New York, 235-245 (2012).

34. Y. Yazicioglu, T. J. Royston, T. Spohnholtz, B. Martin, F. Loth, and H. S. Bassiouny, "Acoustic radiation from a fluid-filled, subsurface vascular tube with internal turbulent flow due to a constriction," J Acoust Soc Am 118(2), 1193-209 (2005).
35. M. De Melis, U. Morbiducci, L. Scalise, E. P. Tomasini, D. Delbeke, R. Baets, L. M. Van Bortel, and P. Segers, "A noncontact approach for the evaluation of large artery stiffness: a preliminary study," Am J Hypertens 21(12), 1280-3 (2008).
36. M. C. Dahl, P. A. Kramer, P. G. Reinhall, S. K. Benirschke, S. T. Hansen, and R. P. Ching, "The efficacy of using vibrometry to detect osteointegration of the Agility total ankle," J Biomech 43(9), 1840-3 (2010).
37. P. Castellini, R. Huebner, and M. Pinotti, "Vibration measurement on artificial heart valve by laser doppler vibrometry," Fifth International Conference on Vibration Measurements by Laser Techniques, International Society for Optics and Photonics (2002).
38. C. C. Rondini, G. L. Rossi, and L. Scalise, "Laser vibrometry and stress measurement by thermoelasticity on mechanical heart valve," Sixth International Conference on Vibration Measurements by Laser Techniques: Advances and Applications, International Society for Optics and Photonics (2004).
39. R. K. Manapuram, V. G. R. Manne, and K. V. Larin, "Development of phase-stabilized swept-source OCT for the ultrasensitive quantification of microbubbles," Laser Physics 18(9), 1080-1086 (2008).
40. J. Li, S. Wang, R. K. Manapuram, M. Singh, F. M. Menodiado, S. Aglyamov, S. Emelianov, M. D. Twa, and K. V. Larin, "Dynamic optical coherence tomography measurements of elastic wave propagation in tissue-mimicking phantoms and mouse cornea in vivo," J Biomed Opt 18(12), 121503 (2013).
41. S. Wang, and K. V. Larin, "Shear wave imaging optical coherence tomography (SWI-OCT) for ocular tissue biomechanics," Opt Lett 39(1), 41-4 (2014).
42. S. Wang S, A. L. Lopez 3rd, Y. Morikawa, G. Tao, J. Li, I. V. Larina, J. F. Martin, and K. V. Larin, "Noncontact quantitative biomechanical characterization of cardiac muscle using shear wave imaging optical coherence tomography," Biomed Opt Express 5(7), 1980-92 (2014).
43. A. R. Skovoroda, S. Y. Emelianov, and M. O'Donnell, "Tissue elasticity reconstruction based on ultrasonic displacement and strain images," IEEE Trans Ultrason, Ferroelect, Freq Control 42(4), 747-765 (1995).
44. J. F. Doyle, Wave Propagation in Structures: Spectral Analysis Using Fast Discrete Fourier Transforms, 2nd ed., Springer-Verlag, New York (1997). ISBN: 0387949402.
45. K. M. Kennedy, L. Chin, R. A. McLaughlin, B. Latham, C. M. Saunders, D. D. Sampson, and B. F. Kennedy, "Quantitative micro-elastography: imaging of tissue elasticity using compression optical coherence elastography," Sci Rep 5, 15538 (2015).
46. S. Wang, and K. V. Larin, "Noncontact depth-resolved micro-scale optical coherence elastography of the cornea," Biomed Opt Express 5(11), 3807-21 (2014).
47. M. Singh, C. Wu, C. H. Liu, J. Li, A. Schill, A. Nair, and K. V. Larin, "Phase-sensitive optical coherence elastography at 1.5 million A-Lines per second," Opt Lett 40(11), 2588-91 (2015).
48. R. W. Kirk, B. F. Kennedy, D. D. Sampson, and R. A. McLaughlin, "Near Video-Rate Optical Coherence Elastography by Acceleration With a Graphics Processing Unit," J Lightwave Technol 33(16), 3481-3485 (2015).

1 Introduction

The biomechanical properties of tissues are important parameters for tissue characterization [1]. For example, keratoconus structurally degenerates the cornea [2], tumors generally stiffen tissue [3], and atherosclerosis hardens the vasculature [4]. Thus, quantifying changes of biomechanical properties of tissue can provide critical information for early diagnosis and effective treatment of various diseases [3, 5].

Several elastographic methods have been developed in the past few decades to characterize the biomechanical properties of tissues, such as ultrasound elastography (USE) [6], magnetic resonance elastography (MRE) [7], acoustic radiation force imaging [8], supersonic shear imaging [9], and dynamic corneal imaging [10]. All of these methods combine an imaging technique with external loading, such as mechanical compression [11], acoustic radiation force [12], pulsed laser [13], or focused air-pulse [14]. The imaging modalities measure the tissue response to the excitation, and these measurements can then characterize the biomechanical properties of tissue through the use of appropriate mechanical models. However, these elastographic methods require relatively large tissue deformation due to their limited displacement sensitivity. Alternatively, Brillouin microscopy can map the Brillouin shift of tissue in 3D with high spatial resolution without external loading [15, 16]. While it is understood that the Brillouin shift is related to the Young's modulus, accurately quantifying the stiffness of tissue from the Brillouin shift is still a challenge.

Optical coherence elastography (OCE) is an emerging technique that can assess the biomechanical properties of tissues completely non-destructively [17, 18]. Similar to USE and MRE, OCE is an elastographic extension of its parent imaging modality, optical coherence tomography (OCT) [19]. In addition to

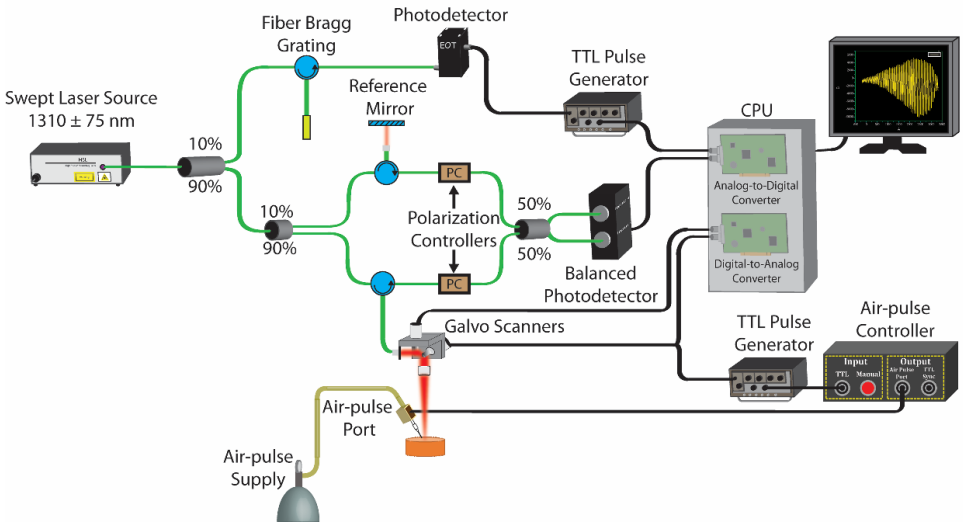


Fig. 1 Schematic of PhS-SSOCE experimental setup.

micrometer-scale spatial resolution, phase-resolved OCT has enabled nanometer-scale displacement sensitivity [20]. We have previously utilized the superior displacement sensitivity of OCT to analyze the propagation of a low amplitude (≤ 10 μm) focused air-pulse induced elastic wave [21]. By quantifying the velocity, the Young's modulus can then be estimated with reasonable accuracy as compared to uniaxial mechanical testing [22, 23].

However, OCT setups, particularly phase-sensitive systems, can be complex and expensive. Simpler and more cost-effective techniques such as Michelson interferometer-based laser vibrometery could potentially also provide measurements for calculating the velocity of the air-pulse induced elastic wave [24]. Laser vibrometry has been successfully used in various applications due to its high sensitivity, which has enabled detection of very small vibrations on the order of the source wavelength. Laser vibrometry was first applied in different engineering fields, such as modal analysis, vibration and noise testing, characterizing loudspeakers, and assessing piezoceramic transducers [25]. Recently, laser vibrometry has gained traction in biomedical and bioengineering applications, such as auditory research [26, 27], dentistry [28, 29], cardiology [30-32], as well as elastography and rheology [33-38].

In this study, a phase sensitive swept source optical coherence elastography (PhS-SSOCE) system and laser Michelson interferometric vibrometer (LMIV), both developed in our lab, were utilized to measure the velocity of focused air-pulse induced elastic waves propagating in tissue-mimicking agar phantoms of various concentrations. The Young's modulus was then quantified from the wave velocity and was compared to the stiffness as measured by uniaxial mechanical compression testing. The results show that the velocities as measured by both systems were very similar, and the estimated Young's modulus was consistent with mechanical testing.

2 Materials and methods

A home-built focused air-pulse delivery system [14] induced elastic waves in tissue-mimicking agar phantoms of various concentrations (1%, 1.5%, 2%, w/w, n=3 for each concentration) The elastic waves were then detected by the LMIV and PhS-SSOCE systems, separately. The air-pulse delivery system employed an air gate and a control unit to provide a short duration (~800 μs) focused air-pulse to the sample surface, and the control unit enabled synchronization of the air-pulse with the OCE and LMIV systems. The air source pressure was obtained from a standard pressure gauge, and the air-pulse was expelled through a cannula port with a flat edge and inner diameter of ~150 μm. The localized air-pulse excitation was precisely positioned with a 3D linear micrometer stage.

The PhS-SSOCE system was comprised of the previously described air-pulse delivery device and a home-built phase stabilized swept source optical coherence tomography (PhS-SSOCT) system. A schematic of the experimental setup is displayed in Fig. 1. Further details about the PhS-SSOCT system can be found in our previous work [39, 40]. Briefly, the PhS-SSOCT system utilized a broadband swept laser source (HSL2000, Santec, Inc., Torrance, California) with central wavelength of 1310 nm, bandwidth of ~130 μm, scan rate of 30 kHz, and output power of ~39 mW. A fiber Bragg grating was used as the A-scan trigger that improved phase stabilization. The axial and lateral resolutions of the system were ~11 μm and ~16 μm, respectively. The phase stability of the system was ~16 milliradians, which corresponded to ~3.3 nm displacement sensitivity in air. The experimental acquisition and data processing methods are detailed in our previous work [41]. Simply, successive M-mode images were acquired in a line, and the M-mode frame trigger was synchronized with the air-pulse so that effectively, the same elastic wave was imaged.

LMIV schematic is depicted in Fig. 2. The LMIV employed a Helium-Neon (HeNe) laser with wavelength of 633 nm and output power of 1.5 mW (model 31005, Research Electro-Optics, Inc., Boulder, CO). The output of the HeNe laser was expanded and collimated to 90% of the objective lens aperture to maximize photon collection. The light beam was then split into sample and reference arms using a 50:50 non-polarizing cube beam splitter. In the sample arm, the beam was transmitted through a 10X microscope objective and focused on the sample surface. In the reference arm, the beam was directed to a matching 10X microscope objective and focused onto the surface of a silver mirror. After the reflected light beam passed through the beam splitter, the interference signal was detected by a silicon photodetector (model DET100A, Thorlabs, Inc., USA). The temporal intensity output from the photodetector was captured by a digital oscilloscope (model DS4014, Rigol Inc., USA). The air-pulse stimulation and the data acquisition were synchronized by a TTL signal, which was provided by a digital pulse generator (model 575, BNC Inc., USA). The system was assembled on a 3-inch thick optical breadboard and supported with four sorbothane isolation pads to maximize system stability and minimize environmental noise. During the LMIV measurements, all data was acquired with the same acquisition window and oscilloscope sampling settings. Six co-linear measurements positions were recorded on each sample, and the distance between two adjacent positions was 1 mm. The time t for the wave to propagate from a reference measurement position to each location was obtained by cross-correlation analysis. The elastic wave velocity, c, was then obtained by the inverse slope of the linear fit of the propagation distances, Δd, to the elastic wave propagation delays, Δt [42].

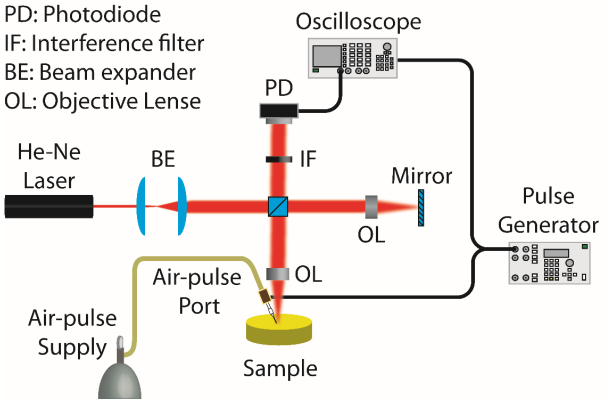


Fig. 2 Schematic of LMIV experimental setup.

Since the tissue-mimicking agar phantoms can be treated as an isotropic homogeneous elastic material, the Young's modulus [43], E, was estimated by [23, 40, 44]:

$$E = 2\rho c^2 \frac{(1+v)^3}{(0.87+1.12v)^2}, \quad (1)$$

where ρ=1.02 k/gm^3 was the material density, and v=0.49 [21, 44] was the Poisson ratio. For all experiments, the output pressure of the air-pulse was ≤ 10 Pa. Uniaxial mechanical compression testing (model 5943, Instron Inc., MA, USA) was performed on the same samples after OCE and LMIV measurement [23].

3 Results

Figure 3 shows typical 1% agar phantom surface response signal to the air-pulse at various positions during OCE (Fig. 3(a)) and LMIV (Fig. 3(b)) measurement. During OCE measurements, 501 M-mode measurements were acquired over 6.9 mm. Figure 3(a) shows typical surface responses to the air-pulse stimulation at OCE measurement positions which were 0.1 mm apart, and the first acquisition position was 1 mm away from the excitation position. During LMIV experiments, the first measurement position was also 1 mm away from the stimulation position, but successive measurement positions were 1 mm apart as depicted in Fig. 3(b).

Figure 4 shows the elastic wave propagation velocity as measured by both systems. The group velocity as measured by OCE was 1.72±0.25 m/s, 3.41±0.49 m/s, and 5.11±0.26 m/s in the 1%, 1.5%, and 2% agar phantoms, respectively. The velocities measured by the LMIV from the same agar samples were 1.75±0.03 m/s, 3.66±0.26 m/s, and 5.13±0.28 m/s, respectively. Statistical testing by a paired t-test showed no significant difference between the two systems (P=0.90, 0.25, and 0.89 for the 1%, 1.5%, and 2% phantoms, respectively).

Figure 5 shows the Young's modulus (E) of the samples estimated based on the OCE and LMIV measurements using equation (1) and as measured by "gold standard" mechanical testing system. The Young's moduli of the 1%, 1.5%, and 2% agar phantoms as estimated by OCE were 8.01±2.3 kPa, 31.39±9.19 kPa, and 69.45±7.07 kPa, respectively. The elasticities as quantified by the LMIV were 8.12±0.28 kPa, 35.69±5.07 kPa, and 70.14±7.57 kPa for the 1%, 1.5%, and 2% phantoms, respectively. The stiffness of the same samples was also measured by mechanical testing (MT), which resulted in a stiffness of 9.46±0.43 kPa, 45.34±2.32 kPa, and 89.25±9.4 kPa for the 1%, 1.5%, and 2% samples, respectively.

4 Discussion

The shape of the displacement as measured by the LMIV (Fig. 3(b)) was somewhat similar to the displacements detected by the OCE system in this work (Fig. 3(a)) and previous work [23, 40]. The differences in the shape of the temporal profiles can be attributed to the different ways of each technique measure the

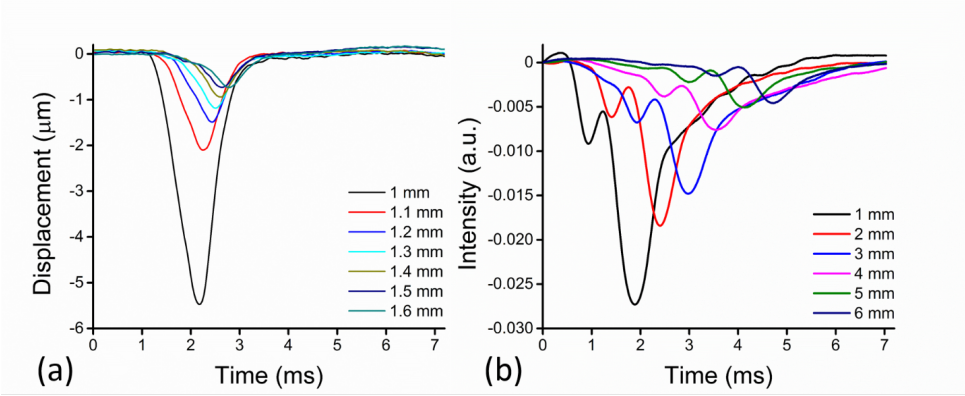


Fig. 3 Sample surface responses of a 1% agar phantom recorded during (a) OCE and (b) LMIV experiment at the indicated distances from the air-pulse excitation.

displacement of the sample. OCE measures the optical path difference between sample and reference arm, and the LMIV measures the intensity of light reflected from the sample surface. More specifically, the elastic wave may undulate similar to a wave in water, and the resulting change in sample surface geometry relative to incident beam may explain the kink during the inward process. Furthermore, OCE can easily provide absolute displacement, which can be used in other OCE techniques, such as compressional OCE for stress/strain analysis [45].

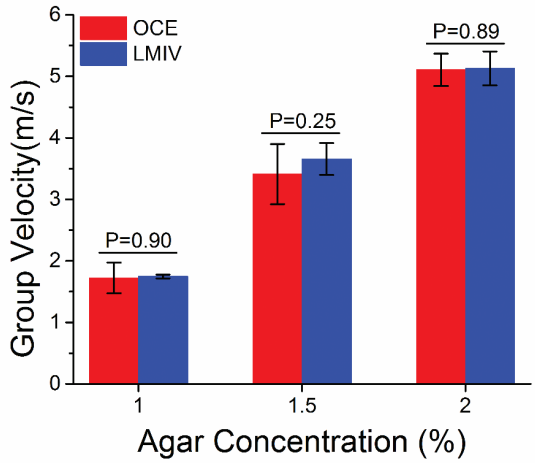


Fig. 4 Elastic wave propagation velocity measured by OCE and LMIV. Statistical testing was performed by a paired t-test to demonstrate that the velocity measurements made by both systems were not different. The respective *P*-values are labeled.

Statistical testing via a paired t-test showed that there was no significant difference between the velocities measured by both systems, with P=0.90, 0.25, and 0.89 for the 1%, 1.5%, and 2% phantoms, respectively (Fig. 4). However, the LMIV can only measure the wave propagation at the surface of the sample since internal scattering is dominated by the specular reflection from the surface. In contrast, OCE can provide depth-resolved elasticity measurements [46]. To further demonstrate the depth-resolved elasticity characterization by OCE, a sandwich-type agar phantom was constructed with a 2% agar layer between two layers of 1% agar (Fig. 6). Because the air-pulse induced elastic wave wavelength is large, spectral analysis was utilized to provide depth-resolved elasticity assessment [46], and all three layers were differentiated successfully. Figure 6 shows the phase velocity of the air-pulse induced elastic wave at 180 Hz. The boundary layers are marked by the dashed red line.

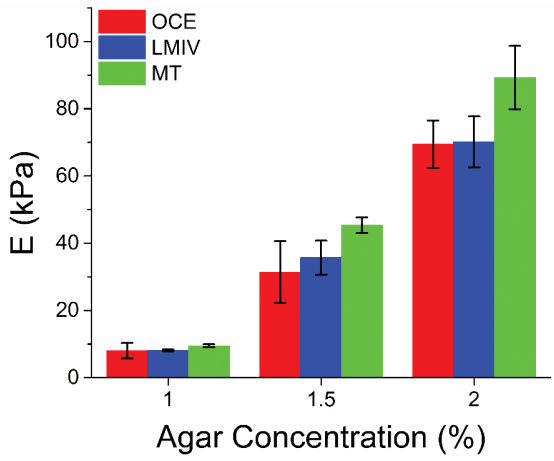


Fig. 5 Young's modulus (E) estimated by the OCE system, LMIV, and as measured by mechanical testing (MT).

The Young's moduli estimated from the group velocities were smaller than as measured by mechanical testing. However, this is in agreement with our very recent investigation and can be explained by assumptions about sample geometry in Eq. 2 and the non-linearity of the agar stress-strain curve [23].

The LMIV can provide very rapid detection of elasticity since the data acquisition and post-processing are minimal. During OCE study, 501 successive M-mode images were acquired at 100 ms per M-mode image, resulting in an acquisition time of approximately half a minute. However, due to the large data size, the post-processing time can be on the order of several minutes. Since each OCE measurement position results in a longer acquisition time and more data, there is an

intrinsic trade-off between spatial resolution and acquisition and processing times. Lateral measurements in the LMIV system were made by translating the sample, whereas the galvanometer-mounted mirrors were used to make measurements at the transverse locations in the OCE system. An automated motorized linear stage would dramatically speed up the acquisition time of the LMIV, but the speed would be limited to ensure that no damage was caused to the sample or that there was no slipping of the sample. Hence, elastographic measurements made with OCE are simpler because the probe beam is moved and not the sample. Furthermore, the LMIV requires precise alignment in order to capture the reflected photons. Moreover, OCE can provide a depth-resolved image of the sample, making alignment significantly easier.

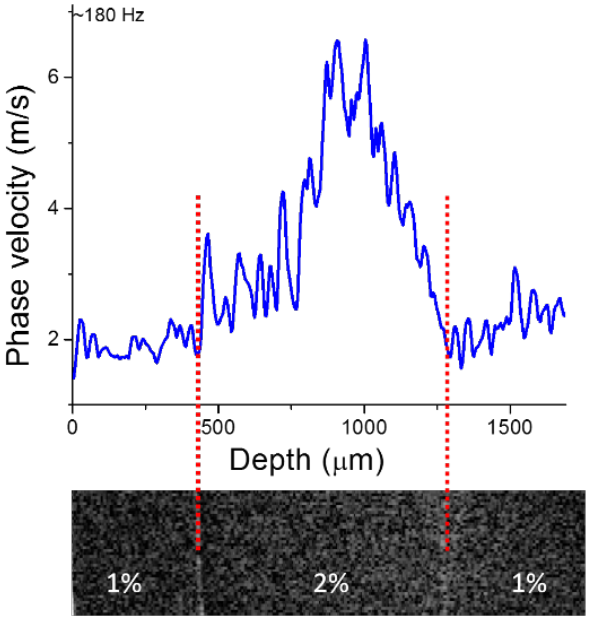


Fig. 6 Phase velocity of the air-pulse induced elastic wave at 180 Hz in a sandwich-type agar phantom (top) with OCT image of the phantom (bottom). The layer boundaries are marked by the dashed red line.

In this study, successive M-mode images were acquired and an air-pulse excitation was synchronized with each measurement. This technique may not be feasible for *in vivo* measurement due to multiple excitations and the extended acquisition time, which may lead to excessive laser exposure. However, we have recently developed a technique that takes advantage of recent advances in OCT sources by directly imaging the propagation of an air-pulse induced elastic wave. Here, only a single excitation was necessary for a line measurement and the MPE limit for the sample (cornea) was not exceeded [47]. However, the spatial and temporal resolutions were still limited as compared to the OCE technique described in this work. Recently, GPU-accelerated compressional OCE has been demonstrated, enabling near real-time 3D elasticity assessment [48]. Combining high-performance computing would drastically reduce the processing time of the OCE post-processing and would also enable near real-time characterization of tissue biomechanical properties and is currently under development.

Another core issue for comparison of the two techniques is the cost. The approximate total costs of building the OCE and LMIV systems are listed in Table 1. The LMIV system is approximately one-tenth the cost of the OCE system. The LMIV system requires a simple HeNe laser, whereas the OCE system requires a broadband low coherence swept source laser. As the LMIV system is an open space system, there are no expensive fiber based components. Fiber optical components are becoming more mainstream and prices continue to decrease. However, the price disparity will still exist due to the sheer difference in complexity of the two systems.

Table 1. Approximate cost in $US of the OCE and LMIV systems used in this study

	OCE	**LMIV**
Light source	20000	850
Optical components	4500	2550
Scan	2850	0
Control units	6500	600
Data acquisition	10000	150
Data processing	3000	500
Total cost	46850	4650

5 Conclusion

In this work we have utilized two optical techniques, laser Michelson interferometric vibrometry (LMIV) and optical coherence elastography (OCE) to assess the elasticity of tissue-mimicking agar phantoms. A focused air-pulse induced elastic waves in the samples, which were then detected by the two techniques. The stiffness of the agar phantoms as quantified from the velocity were measured by the LMIV and OCE systems was in good agreement. The LMIV system was significantly less complex and cost-effective as compared to the OCE system, but the LMIV system cannot provide-depth resolved elasticity assessment. Therefore, if depth-resolved elasticity or high spatial resolutions are not necessary, then LMIV may be a simple and cost-effective technique to measure the elasticity of tissues completely noninvasively.

Optical method for screening and a new proteinuria focus group

Alar Sünter[1*], Aleksander Frorip[2], Vadim Korsakov[4], Remo Kurrruk[3], Artur Kuznetsov[2], and Mai Ots-Rosenberg[1]

[1] Tartu University Hospital, 1a L.Puusepa st., 50406 Tartu, Estonia
[2] AS Ldiamon, Tartu Science Park, 185 Riia st., 51014 Tartu, Estonia
[3] Tartu, Family Medicine Providers Mõisavahe Centre, 2 Mõisavahe st., 50707 Tartu, Estonia
[4] Jeko Disain OÜ, Riia 185,51014 Tartu, Estonia

[*] **e-mail:** alar.sunter@ut.ee

Abstract. The detection of small quantities of proteinuria has gained significance as multiple studies have demonstrated its diagnostic, pathogenic, and prognostic importance. More than 260 samples of urine taken from the patients suffering chronic kidney disease (CKD), diabetes and hypertension have been analysed in the certified laboratory, with urine analyser H-50 (urine test strips) and with an optoelectronic set-up specially designed for this study. Albumin, protein and creatinine concentrations have been determined in the laboratory and the data thoroughly analysed with the aim to find new approaches to tackle the lowered level proteinuria problems. Special attention has been paid to a particular screening focus group of 16 patients all having normal or slightly abnormal levels of albumin in parallel with enhanced levels of total protein (45% cases) up to 0.4 g/L. A fair correlation between the maxima in the protein, protein/creatinine, protein/albumin values and CKD in the focus group has been observed. The urine test strips method gave 94% negative false results for the focus group whereas the new sensor has shown in all cases the presence of proteins. The sensor signals higher than the mean in this focus group were obtained for the donors with the diagnosed CKD and some other diseases. The new method is based on the optical absorption measurements (285 nm) in the protein fractions received with use of the commercial desalting columns PD-10. The method can be applied in the wide region of protein concentrations from ≤0.1 g/L up to the levels of severe proteinuria (~10g/L).
© 2016 Samara State Aerospace University (SSAU).

Keywords: albuminuria, screening, Tamm-Horsfall protein, Bence-Jones protein, diabetic nephropathy.

Paper #2803 received 2015.12.07; revised manuscript received 2015.12.25; accepted for publication 2015.12.30; published online 2016.02.02.

References

1. K. Matsushita, M. van der Velde, B. C. Astor, M. Woodwart, A. S. Levey, P. E. de Jong, J. Coresh, and R. T. Gansevoort, "Association of estimated GFR and albuminuria with all-cause and cardiovascular mortality in general population cohorts: a collaborative meta-analysis," The Lancet 375(9731), 2073-2081 (2010).
2. KDIGO Clinical Practice Guideline of CKD, Kidney International Supplements 3, (2013).
3. M. Rosenberg, and Ü. Pechter, "Microalbuminuuria – südame- ja veresoonkonnahaiguse riski näitaja," Eesti arst, 86(7), 470-473 (2007).
4. KDIGO Guideline for the Care of Kidney Transplant Recipients.
5. G. Pittman, "Evidence lacking on screening for kidney disease," Reuters Health, 27 August. 2012.
6. R. T. Gansevoort, K. Matsushita, M. van der Velde, B. C. Astor, M. Woodward, A. S. Levey, P. E. de Jong, and J. Coresh, "Lower estimated GFR and albuminuria associated with adverse kidney outcomes. A collaborative meta-analysis of general and high-risk population cohorts," Kidney Int. 80(1), 93-104 (2011).

7. J. A. Simerville, M. C. Maxted and J. J. Pahira, "Urinalysis: A Comprehensive Review," Am. Family Physician 71(6), 1153-1162 (2005).
8. J. Dube, J. Girouard, P. Leclerc, and P. Douville, "Problems with the estimation of urine protein by automated assays," Clin. Biochemistry 38(5), 479-485 (2005).
9. P. L. Lynch, J. Savory, and D. M. Haverstick, "Urine total measurement with the Vitros dry reagent technology: modification of diluent to resolve positive bias of diluted samples," Clin. Chem. 44(3), 674-675 (1998).
10. R. E. Chambers, D. G. Bullock, and J. T. Whicker, "Urinary total protein estimation – fact or fiction?" Nephron 53(1), 33-36 (1989).
11. M. Rosenberg, A. Kuznetsov, and A. Frorip, "Threshold-like dependences in albuminuria/proteinuria," Eesti Arst (Estonian Doctor) 92(Suppl. 2), 1-52 (2013).
12. A. Sünter, A. Kuznetsov, A. Frorip, V. Korsakov, and M. Rosenberg, "Optical methods, devise and statistics of determination of albumin and/or protein concentration in human urine," Saratov Fall Meeting 2015, Biophotonics Internet Invited Lecture.
13. S. G. Guminetsky, O. R. Gauka, G. I. Kokoschuk, P. M. Grigorishin, and N. L. Kirsh, "Absorption spectra of the main organic components of human urine in the absence of proteins," Proc. SPIE 3904, 579 (1999).
14. K. Umimoto, Y. Kanaya, H. Kawanishi, and N. Kawai, "Measuring of uremic substances in dialysate by visible ultraviolet spectroscopy," IFMBE Proc. 25(7), 42-45 (2009).
15. H.A. Schwertner, "Isolation and chromatographic analysis of unidentified fluorescence in biological fluids of patients with chronic renal disease," Nephron 31(3), 209-211 (1982).
16. A. Kuznetsov, A. Frorip, A. Maiste, M. Ots-Rosenberg, and A. Sünter, "Visible auto-fluorescence in biological fluids as biomarker of pathological processes and new monitoring tool," J. Innov. Opt. Health Sci. 8(3), 1541003 (2015).
17. PD-10 Desalting Columns (GE Healthcare), Instructions 52-1308-00 BB, General Electric Company, September 2007.
18. G. Konoplev et al., "Dual-wavelength optical sensor for on-line monitoring of uric acid concentration in spent dialysate during hemodialysis," XI Baltic Nephrology Conference (Tartu), Programme and Abstract Book 48, 20-22 September 2012.
19. Y. Zuo, C. Wang, J. Zho, A. Sachdeva, and V. C. Ruelos, "Simultaneous Determination of Creatinine and Uric Acid in Human Urine by High-Performance Liquid Chromatography," Analytical Sciences 24(12), 1589-1592 (2008).
20. Y. Yue-dong, "Simultaneous determination of creatine, uric acid, creatinine and hippuric acid in urine by high performance liquid chromatography," Biomedical Chromatography 12(2), 47-49 (1998).
21. Urine Anlyzer H-50.
22. E. V. Lerma, T. Desai, and P. Jawa, "Proteinuria: Background, Pathophysiology, Etiology," 10 December 2015.
23. Reference < 200 g/g for protein/creatinine is being issued in the routine praxis of the TUHL.
24. Extinction Coefficients, A guide to understanding extinction coefficients, with emphasis on spectrophotometric determination of protein concentration, Pierce Biotechnology, October 2002.
25. S. C. Gill, and P. H. von Hippel, "Calculation of Protein Extinction Coefficients from Amino Acid Sequence Data," Anal. Biochem. 182(2), 319-326 (1989).
26. D. C. J. Rhodes, "Binding of Tamm-Horsfall protein to complement 1q measured by ELISA and resonant mirror biosensor techniques under various ionic-strength conditions," Immunology and Cell Biology 78(5), 474-482 (2000).
27. SIGMA ProductInformation.
28. I. Björk, F. A. Karlsson, and I. Berggård, "Independant Folding of the Variable and Constant Halves of a Lambda Immuniglobulin Light Chain," Proc. Nat. Acad. Sci. 68(8), 1707-1710 (1971).
29. B. L. Boyanton, and K. E. Blick, "Stability Studies of Twenty-Four Analytes in Human Plasma and Serum," Clin. Chem. 48(12), 2242-2247 (2002).
30. A. Kuznetsov, A. Frorip, M. Rosenberg, and N. Mulina, "Time dependences of concentrations of serum creatinine and uric acid in spent dialysate," X1 Baltic Nephrology Conference (Tartu), Programme and Abstract Book 51, 20-22 September 2012.
31. C. Y. Yang, F. A. Chen, C. F. Chen, W. S. Liu, C. J. Shih, S. M. Ou, W. C. Yang. C. C. Lin, and A. H. Yang, "Diagnostic Accuracy of Urine Protein/Creatinine Ratio Is Influenced by Urine Concentration," PLoS One 10(9), e0137460 (2015).

1 Introduction

Population studies have demonstrated the presence of the chronic kidney disease (CKD) in 10% cases and therefore CKD is an important public health issue. CKD is the common disease but few individuals have strongly reduced glomerular filtration rate (GFR), kidney failure or severely increased albuminuria. However, there is

substantial evidence linking increased albuminuria to outcomes of CKD [1, 2]. The detection and evaluation of small quantities of proteinuria have gained significance as multiple studies have demonstrated its diagnostic, pathogenic, and prognostic importance [1-3]. There exists a large need for the express and cheap methods for the population screening and regular monitoring of albumin and/or protein levels in urine of people suffering the CKD. Albuminuria should be monitored also regularly in patients with transplanted kidney [4]. Screening of healthy people is also an important topic but there is not enough evidence to recommend checking the kidney function of otherwise healthy people for signs of disease [5]. One can think that the development of assay methods will allow the people to perform self-screening even at home. This may be appropriate because the CKD is the common disease and higher albuminuria is associated with adverse kidney outcomes [6].

Urine test strips (or dipsticks) are well known instruments invented for such purposes but the cheap test strips cannot enable sufficient sensitivity and precision. In the KDIGO 2012 guidelines [2] it is stated that "…there is no standardization between manufacturers. The use of such strips should be discouraged in favour of quantitative laboratory measurements of albuminuria or proteinuria". Strips are envisaged mainly for selective detection of albumin and are not sensitive to some other proteins, e.g., Bence-Jones proteins (monoclonal heavy or light chains) and give often negative false results [7].

At the same time the laboratory total protein assays are also commonly flawed and under these circumstances are often still standardized against albumin [2]. Comparison of different automated assays of urine protein was carried out [8]. It was established that the results of different methods (Randox, Beckman, Roche and Vitros) at low, so called, normal protein concentrations (≤ 0.1 g/L in the untimed samples) do not correlate with each other and with the data obtained by the Ponceau S/TCA manual method used by the authors. It was also speculated that the colorimetric (a dye binding; Randox, Beckman, Vitros) and turbidimetric (protein agglutination; Roche) methods usually used in automated technologies can be not neutral for very complex urine environment and can depend on the concentration of one or another urine component, e.g., sodium chloride and other salts [9].

There is one more possible explanation of deviations connected with different reaction of different protein components (albumin, globulin, Tamm-Horsfall, polypeptides) with different reagents under use. For instance, small peptides induced significant signals with the Beckman and Randox assays and were neglected by the Roche and Ponceau S/TCA assays [8].

All circumstances mentioned above manifest that the protein quantification at lowered concentrations can be a challenge [10] not only for the work with the express methods but even for the certified automated laboratories. At the same time it is often impossible to avoid the direct estimation of proteins because there are the diseases when it is necessary to know just the total protein and not only albumin concentration (tubular proteinuria, children diseases etc.) [2].

In this study we have encountered a particular case where by the low (normal or slightly abnormal) levels of urine albumin (≤ 0.03 g/L) the total protein concentrations can be rather high, e.g., by the factor of 10 and much more. Abnormal protein level is correlated with diabetes, hypertension, kidney and urinary failures in these urine donors. This new fact directly points to one more reason why it is important to provide the total protein quantification in urine.

2 Aims

The main aim of the undertaken study was to demonstrate the possibility to exploit the UV absorption of proteins at $\lambda \approx 285$ nm in specially fractionated urine for estimation of their concentration in the whole human urine. The second goal of the project was the comparison of optical results with those obtained in parallel by use of urine test strips and automated (Roche) assays. Additionally, a concise analysis of the obtained results from the clinical point of view is also undertaken. The given research is a continuation of our previous studies [11, 12].

3 Method, patient and samples

3.1 Urine fractionation

We have used the direct UV absorption measurement at $\lambda \approx 285$ nm for the estimation of total protein concentration. In the whole urine the absorption at ~280 nm is very high and is induced mainly by uric acid [13, 14] and, so called, visible (blue) fluorescence substance (VFS) present in all biological fluids [15, 16]. The absorption of proteins is usually totally masked by these components. Therefore urine has to be fractionated to extract the protein fraction envisaged for optical measurements.

For fractionation commercially available and cheap PD-10 desalting columns (GE Healthcare) with the cut-off at M < 5 kDa were used [17]. The urine fraction eluted as the timely first contains the whole pool of the typical urine proteins (albumin, globulin, Tamm-Horsfall, etc.) and, eventually, some large peptides and complexes with the molecular masses M > 5 kDa.

The chronogram of such a fractionation of urine with the starting protein concentration of 5 g/L is represented in Fig.1. The sharp peak at the retention time $t \approx 1.5$ min belongs to the total protein fraction. The other peaks are induced by the VFS (the interval 3.5 – 5 min) and uric acid (7.5 min). Additional analysis has shown that in the protein fraction there are residuals of the abundant metabolites urea and creatinine in a rather high concentration of ~ 10 and ~1 mmol/L, respectively. These metabolites absorb the light in the region $\lambda < 250$ nm and do not disturb our

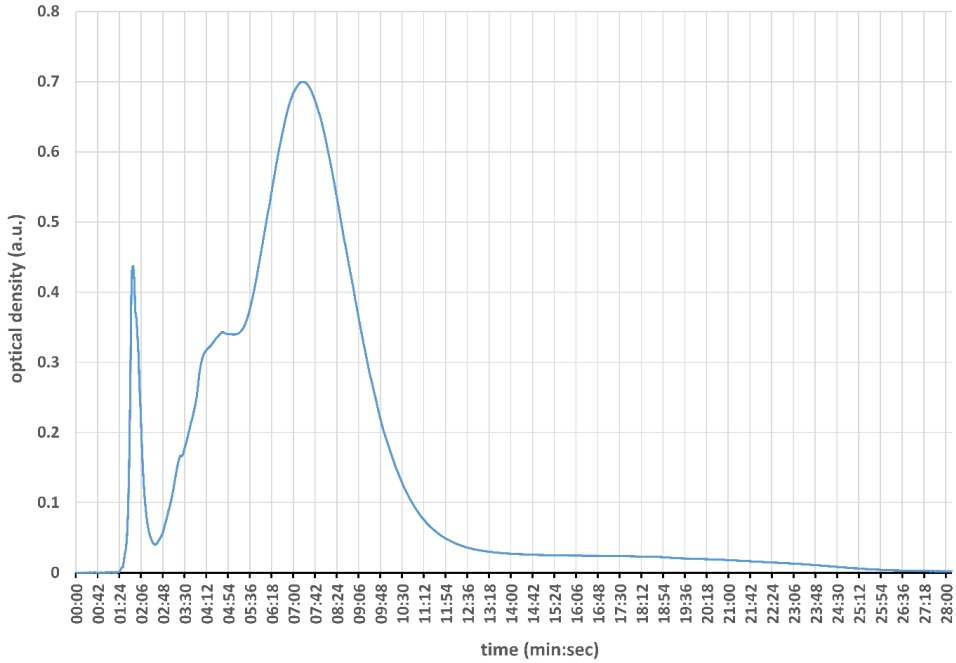


Fig. 1 Fractionation chronogram of albuminuria urine in a desalting column PD-10. The 1.5 min elution peak belongs to proteins with M > 5 Da whereas the hump at 3.5 min to the VFS and the most intensive maximum (6.5 min) to uric acid.

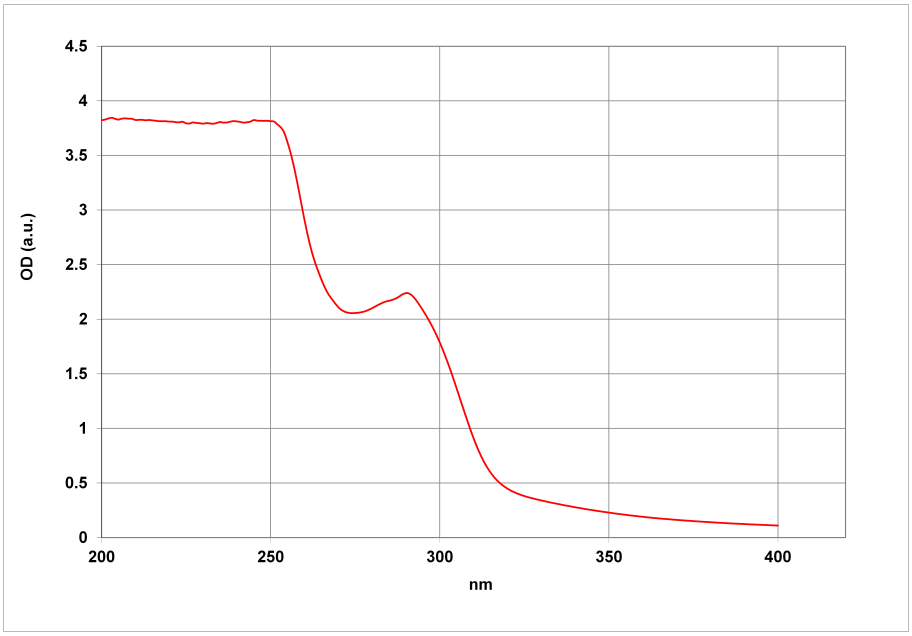


Fig. 2 Absorption spectrum of a urine fraction M > 5kDa in the 5 mm thick layer. The concentration of protein in the whole starting urine was 5 g/L.

measurements (see also [14]). The presence of uric acid could not be established in the protein fraction at the sensitivity level of the Cobas 6000 Roche method (<12 μmol/L). No correlation between the uric acid concentration in the starting urine and the protein peak maximum in the chronograms has been seen.

The absorption spectrum of a protein fraction produced by use of a PD-10 column is given in Fig.2. The spectrum was measured at a spectrophotometer Jasco V-550. One can see that the absorption for the 5 mm layer in the case of protein concentrations in the starting urine material in the range of several g/L (5 g/L in the given case) is high with optical density (OD) of >2. In the special test with water dilution of a high protein level fraction the linearity of OD in the range 2.84 – 0.05 with a very small correlation variation (CV) (R^2 = 0.9996) was established.

It is important to mention that one and the same PD-10 column is suitable for multiple usages up to 100 times and more. This experience has been obtained in

the exploitation mode applied in this study: 200 μL of starting urine plus 50 ml of a buffer for one fractionation procedure. By this protocol strong dilution 1:250 does take place and the variations in concentration (specific density) of starting urines are minimised and could not be taken into account.

3.2 Choose of buffers

We have proved different buffer liquids needed for fractionation with the wide pH range from pH3.5 (e.g., blank dialysate SW 380 A) up to pH9.3 (10 mM TRIS + 150 mM NaCl + 2 mM EDTA). The distilled or salt water with 0.9 wt. % of NaCl (physiological fluid) can be used too. One can obtain higher signals in the chronograms for the protein peaks (M > 5 kDa) with distilled water but the measurement errors, i.e., stdev/average in this case were sometimes higher than with the other buffers, i.e., ≈10% instead of 3.5 – 5% for the more complex buffers. The results represented in this paper are obtained mostly with the basic buffer pH9.3 (10 mM TRIS +150 mM NaCl +2 mM EDTA).

3.3 CKD patients

Urine samples were collected from the CKD or at CKD risk subjects (diabetes and/or hypertension) treated in the nephrology division at the Tartu University Hospital (TUH) or monitored in the ambulatory service at the TUH or at the Family Medicine Providers Centre (FMPC) Mõisavahe (Tartu).

In this study we have paid much attention to the patients with the normal urine albumin (≤ 0.03 g/L) and with abnormal protein (≥ 0.1 g/L) in untimed samples. The FMPC part of them (16 patients) constituted the main focus group for the further scrutinised investigation.

Additionally, 5 urine samples were taken from the healthy people for comparison purposes.

The average age in the main focus group (50% males and 50% females) was 56.75 years, whereas the average age for the controls (4 males and one female) was "tuned" to the close level of 57.6.

3.4 Urine samples

Altogether 261 samples of urine were collected and analysed. All samples were taken one or two times and usually in the first half of the day. No 10-hours or day night collection attempts were undertaken. Approximately 150 different urine samples were assayed in the laboratory of the Tartu University Hospital (TUHL) where the Cobas 6000 Roche systems technology is being used. The albumin, protein, creatinine and, sometimes, uric acid concentrations were determined. The dominant part of urine samples were delivered to the TUHL as soon as possible (mostly within one hour). The samples collected at the FMPC could be transported to the TUHL in several hours.

Many urine samples were stored in the frozen condition at -10^{0}C and some of those were reused for additional or special tests. No remarkable changes in relation to protein optical absorption after the freezing/de-freezing circles have been noted.

A part of urines were centrifuged before fractionation at the angle speeds of 1200-3000 rpm. Sometimes there were precipitates on the bottom of test-tubes with fresh or de-frozen centrifuged urines. We avoided using in experiments the lowest part of the fluids with precipitates but one cannot exclude the influence of the smallest suspension particles which scatter the light and affect the accuracy of absorption measurements. Different scattered light levels were indicated in some samples in the urine transparency region at $\lambda > 300$ nm but they were not quantified and not used in the estimations. This matter should be given more attention in the future (see p. 5.1.).

Another part of urines was filtered with use of the Whatman FP30/0.45 CA-S 0.45 μm filters. More stable results have been obtained with filtered urines than with centrifuged ones.

3.5 Optical cell and chronograms recording

For the measurements a UV optical cell cognate with that used in [18] was connected to the exit of a column PD-10 and the standard chronogram recording on a computer monitor took place (Fig. 1). This approach resembles those used earlier for determination of small molecular mass urine components by the methods of high performance liquid chromatography [19, 20]. We have used the area under the protein peak in the chronograms as the measure of protein absorption (concentration) after the recalculation "*peak area → concentration*". The computer programme stopped the measurement at the first minimum in the chronogram, i.e. approximately at the retention time t ≈ 2.5 min (Fig.1) so that the peak measurement procedure lasted usually less than 2 min. One needs an additional time (~10 min) for the elution of all smaller mass fractions and prepare the column for the next measurement.

The analytical error "stdev/average" in the multiple test measurements (10 up to 20) with one and the same urine was mostly between 3.5 and 5% at the low (0.1-0.2) as well as at the high protein concentrations (3.5 g/L).

There is some inaccuracy in this mode of measurements because of the overlapping of the protein and strong VFS elution peaks (Fig. 1). We have circumvented this difficulty by the use of the empirical correlation "*protein peak area*" versus "*certified protein concentration in the starting whole urine*". This correlation was obtained on the base of the numerous (~ 100) parallel measurements in the TUHL and by our method with all possible urine protein concentrations from 0.03 up to 10 g/L. The obtained linear dependence formula $p = k\ x\ + b$, where p is the protein concentration, x – peak area, k – slope and b – bias, served further for estimation of a newly measured protein concentration (for the value of the parameters k and b see *p.4.1*). This approach does work well. The

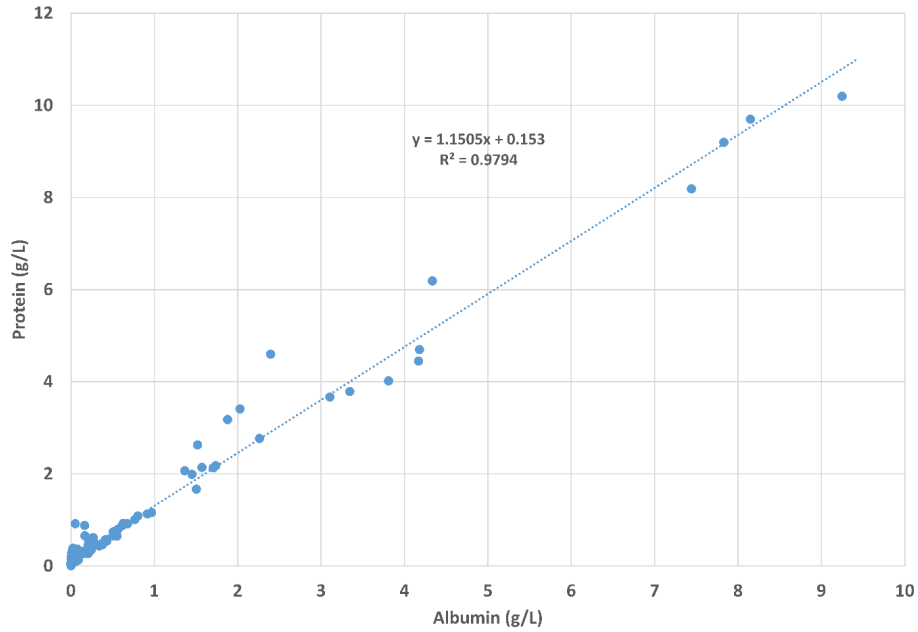


Fig. 3 Correlation between albumin and protein concentrations determined by the Roche assays in the whole urines (133 samples) in the widest available range of concentrations from 0.002 g/L for albumin up to 9.3 g/L for both albumin and protein.

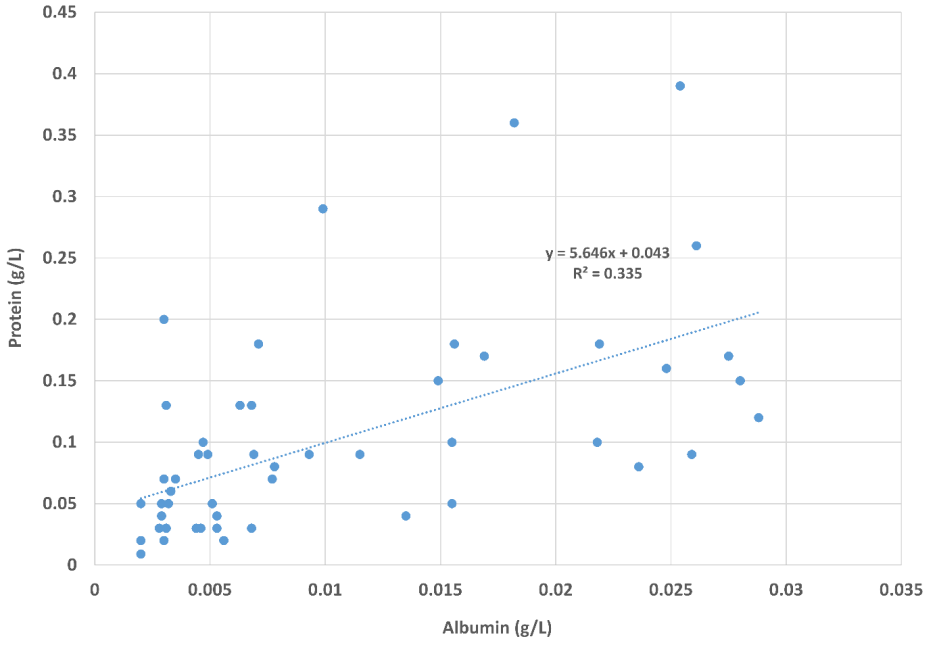


Fig. 4 The part of the lowest albumin vs protein concentrations correlation as a fragment from the united interdependence in Fig.3.

differences sometimes still observable in the results obtained by the proposed method and Cobas 6000 Roche assays can be connected not so much with the technical aspects of measurements but with different and hardly predictable variations in interaction of urine components in the different methods and technologies (see also Introduction and Discussion). Nevertheless, we have used in this study the laboratory data as the reference and designate these as “certified data”.

3.6 Use of urine test strips

We have used a commercial DIRUI urinalysis instrument H-50 for the work with the samples collected at the FMPC. In this photoelectric colorimetry device the urinalysis strips of the type H13 were used for an automated reading of coloured strips at six possible wavelengths 400, 520, 560, 610, 660 and 940 nm [21].

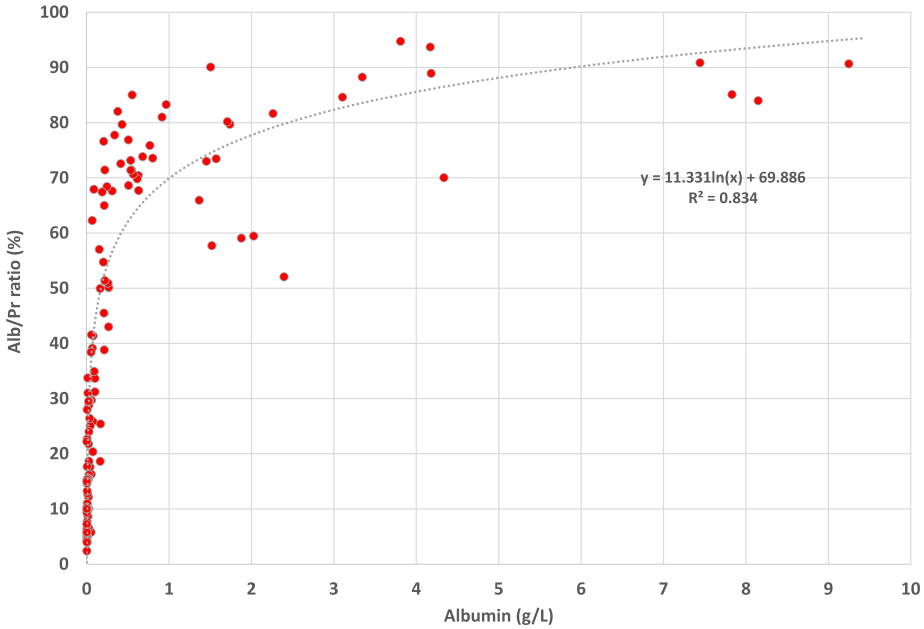


Fig. 5 Albumin/protein ratio Alb/Pr dependence on albumin concentration in 133 samples of the whole urines (compare with Fig. 3).

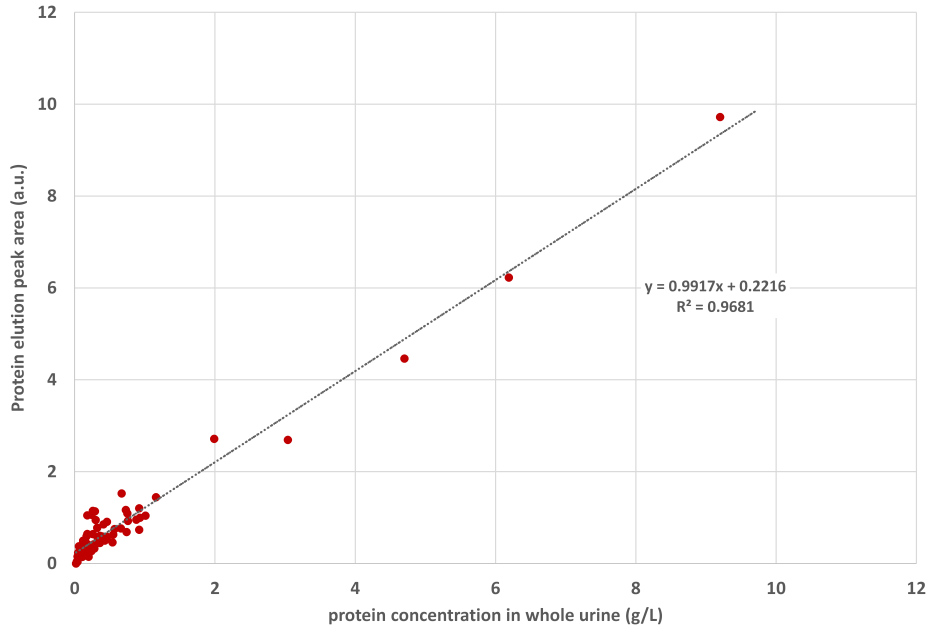


Fig. 6 Correlation between the absorbed light sum designated as the "protein elution peak area" and concentration of protein in the corresponding whole urines established for the widest range of concentrations up to ~10 g/L.

4 Results

4.1 Certified data obtained with the whole urine samples

In Fig.3 we demonstrate the correlation between albumin and protein concentrations in the whole urines using the data obtained by the Cobas 6000 Roche technique for 133 samples. We have tested the urines with the widest available concentration extension from the lowest 0.002 g/L of albumin and 0.01 g/L of protein for healthy people up to ≈10 g/L for both components in the severe proteinuria case. In these wide scales the obtained correlation

$$y = 1.15x + 0.15 \text{ g/L} \quad (1)$$

is perfectly linear (R^2 = 0.9794) and can be used for rough estimation of protein concentration y on the base of known albumin data x or *vice versa*.

It is important to note that in the empirical formula (1) there is the bias parameter b = 0.15 g/L. This would mean that in the albumin-free urines (x=0) there are other proteins at a rather high concentration of 0.15 g/L.

The similar correlation formula holds also for the albuminuria region 0.03 – 0.3 g/L (36 samples in our collection)

$$y = 1.15x + 0.19 \text{ g/L} \quad (2)$$

with the CVs much larger in this case (R^2 = 0.2391).

If we had focused our consideration particularly onto the region of the lowest levels of both albumin and protein, i.e., at the normal albumin concentrations x ≤ 0.03 g/L (50 donors) we have obtained the essentially different correlation

$$y = 5.65x + 0.04 \text{ g/L}. \quad (3)$$

The corresponding distribution is depicted in Fig. 4. The proportionality coefficient 5.65 before x in (3) is much larger than in (1) and (2) showing the diminished role of albumin in this region. The decrease of the bias down to 0.04 g/L is also remarkable. The scattering of the dots in Fig. 4 is high (R^2 = 0.335) what creates difficulties for precise work in this domain. One can see that there are some points which deviate especially strongly upwards and lie in the range of protein concentrations 0.15 – 0.4 g/L. This region is beyond the normality level of protein determined typically at < 0.15 g /24 hours or translated to the concentration < 0.1 g/L by the daily urine dose 1.5 L [22]. We will pay later on the main attention just to these enhanced protein values (see *p.4.3*).

Fig. 5 demonstrates one more possibility to distinguish three sub-regions in the wide proteinuria region 0.01 – 10 g/L which need to be addressed separately. There is in Fig. 5 the depicted distribution of concentration ratios albumin/protein Alb/Pr in the same family of samples as in Fig. 3. The distribution can be fairly approximated by the logarithmic law

$$y = 11.33\ln(x) + 69.89, \quad (4)$$

where x is the concentration of albumin in g/L and y – ratio Alb/Pr in %. At the largest concentrations (> 2 g/L) the total protein consists mostly of albumin (>80%). The albumin portion asymptotically approaches 100% and one can say that in this region proteinuria is, in essence, albuminuria or *vice versa*. At the curve bend around 1 g/L the domination of albumin is not so strong (~70%) and in the region of lower values (< 0.3 g/L) the ratio Alb/Pr decreases abruptly. In this region the significance of albumin is diminished and it is even doubtful whether the albumin can be used as a standardization agent. In determination of protein by means of measurement of albumin it would be the case of determination of a "large" through a "small". These observation and distribution (Fig. 5) gave us one more impetus to elaborate a method for direct determination of non-albumin proteins.

4.2 Optical sensor data

In Fig. 6 we represent the correlation between the optical sensor readings obtained with the urine protein fractions as described in *p. 3.1.* and protein concentrations (g/L) in the whole urines as assayed by the Roche method in the TUHL. The correlation

$$y = 0.99x + 0.22 \text{ g/L}, \quad (5)$$

where x is the protein concentration in g/L in a whole urine and y is a sensor reading. The formula (5) is valid for estimation of high protein concentrations (> 1 g/L): the difference y – 0.22 g/L gives the protein concentration. Using obtained protein concentration one can estimate also the albumin level with the aid of the correlation (1). The accuracy of these estimations is not very high (±20% or even more) but one can mention, for comparison, that the urine test strips do not typically work selectively in the region of concentrations > 0.3 g/L.

In the region of the lower proteins the correlation (5) transforms into the other formulas. For instance, for the protein concentrations ≤ 0.3 g/L the correlation is:

$$y = 2.284x + 0.047 \text{ g/L}; (R^2 = 0.405) \quad (6)$$

The remarkable CVs coming together with the correlation (6) is a reflection of the fundamental phenomenon that the proportions of albumin and non-albumin proteins are very different in the urines from the range of normal (≤0.03), microalbuminuria 03 – 0.3) and severe albuminuria (> 1 g/L) (Fig 5).

It is important to stress that the determination uncertainties arise not just from the low accuracy of the method or sensor itself. The analytical error "stdev/average" was in some tests with 10 up to 20 repeatedly done fractionations only 3.3% and always below 10%. The optical sensor readings are induced by the absorption of albumin and other proteins altogether. For instance, two urines can be of one and the same concentration of low total protein but with a different proportion protein/albumin (Fig. 4) and the sensor readings can be different since not all total protein components must have the equal absorption coefficients. In fact, the similar problem exists by the biochemical assays since not all particular proteins give the equal yields in reactions with dyes or coagulants [8]. This problem is considered in more details in *p. 5.2*.

4.3 Screening results

We present here the results of a pilot population screening action performed at the FMPS Mõisavahe (Tartu) (see *p.3.3*). The manifestation of our method as a helpful instrument for such purposes is aimed at.

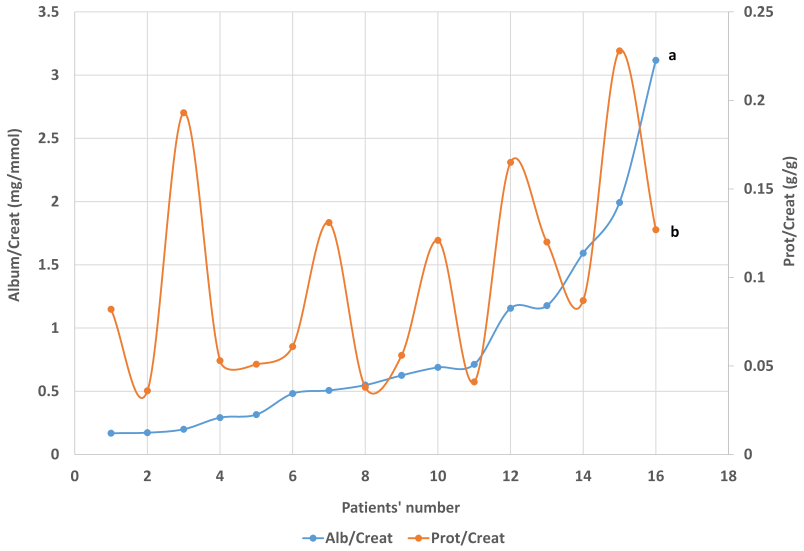


Fig. 7 Markers albumin/creatinine (a) and protein/creatinine (b) in the whole urines from 16 patients of the screening focus group. For other details see Table 1.

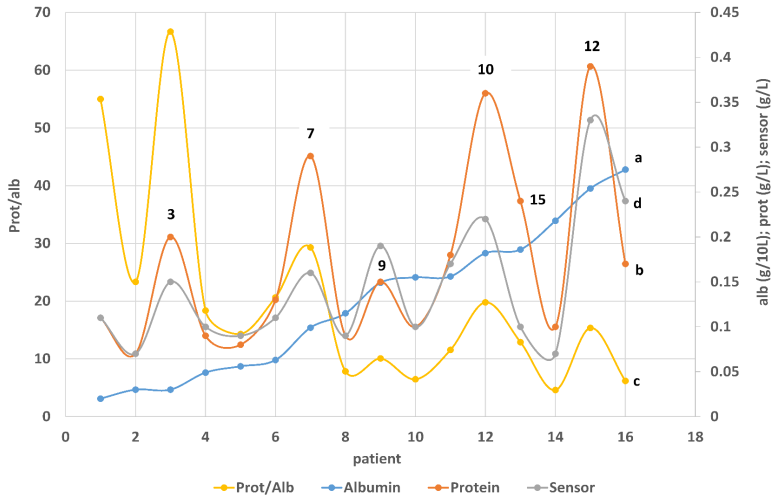


Fig. 8 Distributions of laboratory albumin (*a*) and protein (*b*), ratio protein/albumin (*c*) and readings of the UV sensor (*d*) in the same focus group as in Fig. 7. The inserted numbers 3, 7, 9, 10, 15 and 12 indicate the corresponding positions in Fig. 7. For additional data see Table 2.

Among 41 patients with diabetes or/and hypertension registered at the FMPC there were 16 (39%) patients with the normal or slightly abnormal albumins (≤ 0.03 g/L). These patients formed the focus sub-group for our investigation (see also p. 3.3).

In Table 1 there are the data on the albumin/creatinine (mg/mmol) and protein/creatinine (g/g) parameters in the whole urines which are widely acknowledged in the clinical praxis for searching and monitoring of renal, uremic and other pathologies. Fig. 7 illustrates the specificity in distribution of the given parameters in this focus group. We see a spectacular difference if we depict the distribution of albumin/creatinine values as the gradually growing curve *a* and the corresponding curve *b* for protein/creatinine. Some maxima of the curve *b* point to the patients 3, 7 and 10 with the CKDs as it is noted in Table 1.

One can note, however, that the CKD patient 9 (a young girl) in Table 1 did "remain" without such a particular maximum in the curve b in Fig.7. Her albumin /creatinine (0.626 mg/mmol) and protein/creatinine (0.056 g/g) parameters are remarkably lower than the mean value 0.86 mg/mmol and median ≈ 0.085 g/g in these two rows, respectively. The repeated tests done with the intervals of two-three months gave the similar results for the patients 3, 7, 9 and 10 (Table 1).

It is also noteworthy that only in two cases the values of the parameters albumin/creatinine

(3.117 mg/mmol, patient 16) and protein/creatinine (0.228 g/g, patient 15) exceed the references indicating the probable danger. In both cases no information about additional diseases was available. The control performed with patient 15 two months later gave 0.117 g/g what points to the transient proteinuria in this case.

Table 1 The patients in the screening focus group with low level albumin/creatinine and protein/creatinine parameters.

Patient	Alb/Creat mg/mmol	Prot/Creat g/g	Diseases
1	0.169	0.082	HT
2	0.173	0.036	HT
3	0.2	0.193	CKD
4	0.292	0.053	HT
5	0.316	0.051	HT
6	0.482	0.061	D
7	0.507	0.131	CKD
8	0.549	0.038	HT
9	0.626	0.056	CKD
10	0.689	0.121	CKD
11	0.713	0.041	HT
12	1.157	0.165	HT
13	1.177	0.12	HT
14	1.592	0.087	HT+D
15	1.993	**0.228**	HT
16	**3.117**	0.127	HT

Explanations to Table 1. HT – hypertension, D – diabetes, CKD – chronic kidney disease. The numbers in bold indicate the patients whom belong the maxima in the curve *b* in Fig. 7 as well as the values exceeding the normality references given in [2] for albumin /creatinine (≤3 mg/mmol) and in the Cobas 6000 Roche practical guide for the protein /creatinine marker (< 0.200 g/g) [23].

Unsatisfied with the results obtained with the standard markers albumin/creatinine and protein/creatinine we have tried another approach to the same patients' group and took into account the data on the single albumin and protein concentrations (Table 2). In Table 2 we give also our sensor data in g/L, ratios protein/albumin as well as urine test strips data. We reproduce the information about the diseases in the focus "group 16".

In Fig. 8 by analogy with Fig. 7, the curve *a* is albumin and the curve *b* protein concentration distributions. Again, we see strong fluctuations in the protein curve *b* on the relatively smooth background of the albumin curve *a*. It is remarkable that all patients 3, 7, 9 and 12 with the identified CKD obtain now their own maxima in the curve *b*. The correspondence of the maxima in Fig. 8 to the "clones" in Fig. 7 is given by the numbers placed near the maxima and at the position 13 in Fig. 8. Additionally, we have drawn the curve *c* for the ratios protein/albumin. The curve *d* represents the protein concentration data obtained with our sensor.

We see that the similar behaviour of three distributions *b*, *c* and *d* is obvious: the quantity (5+4) and positions of all extrema coincide sharply. Numerically, the Pearson correlations are: r = 0.79 for the arrays "laboratory protein vs sensor data" and r = 0.086 for "laboratory protein vs protein/albumin". Regardless the latter weak correlation we would consider the parameter protein/albumin as a useful one for its insensitivity to the urine density and other characteristics (time of sampling, is it a 24 h dose or not, is it stored for long or short time etc.). As one can see from Table 2 and Fig. 8 the high values of the protein/albumin ratios (> 10) can serve as indications to the pathology.

The important result seen in Table 2 and in Fig. 8 is that all patients 3, 7, 9 and 12 with the CKD have their own maxima in the characteristics based on the protein (*b*), protein/albumin (*c*) and sensor (*d*) data. This is in the contrast to the situation with the creatinine parameter involvement (Table 1 and Fig. 7) where the CKD patient 9 had no specific maximum. All laboratory and sensor data for the patients 3, 7, 9, 12 and 15 with maxima in Fig. 8 and Table 2 are higher than the mean (0.14 g/L) or median (0.11 g/L) values in the focus group.

In parallel, almost all tests with strips gave negative results, i.e. 15 from 16 or 94%, only for the patient 15 with the laboratory protein 0.39 g/L the reading was positive (0.15 g/L). We take this information as a fact.

At the same time, we see that not all certified laboratory data coincide well with our sensor readings. These deviations are more pronounced for the higher protein concentrations than for the lower ones: in the last case the perfect coincidence is predominant (nine patients 1, 2, 4, 5, 6, 8, 10, 11, 14 or 56% of the cohort).

We can also mention that for the FMPC patients with the albuminuria in the range 0.03 – 0.3 g/L, sometimes called microalbuminuria, (19 persons) 15 tests with strips (79%) gave positive results in the relation to presence of protein. Three tests from these 15 (or 20%) one can name as false positive since the strip readings were 1.5 up to 5 times higher than the Roche assay ones.

The sensor data obtained in this albuminuria group correlated well with the laboratory protein (r = 0.863) and, surprisingly, weakly with albumin values (r = 0.124). It means that our method works preferably for detection of non-albumin proteins even in the albuminuria region, at least, for the hypertension, diabetes and CKD patients.

Table 2 Focus group patients' characteristics with a partial connection to the data given in Table 1.

	Albumin, g/L	Protein, g/L	Sensor, g/L	Prot/Alb	Strip, g/L	Disease
1	0.02	0.11	0.11	55	Neg	HT
2	0.03	0.07	0.07	23.33	Neg	HT
3	0.03	0.2	0.15	66.67	Neg	CKD
4	0.049	0.09	0.1	18.37	Neg	HT
5	0.056	0.08	0.09	14.29	Neg	D
6	0.063	0.13	0.11	20.63	Neg	HT
7	0.099	0.29	0.16	29.29	Neg	CKD
8	0.115	0.09	0.09	7.83	Neg	HT
9	0.149	0.15	0.19	10.07	Neg	CKD
10	0.155	0.1	0.1	6.45	Neg	HT
11	0.156	0.18	0.17	11.54	Neg	HT
12	0.182	0.36	0.22	19.78	Neg	CKD
13	0.186	0.24	0.1	12.90	Neg	HT
14	0.218	0.1	0.07	4.59	Neg	HT
15	0.254	0.39	0.33	15.35	0.15	HT
16	0.275	0.17	0.24	6.18	Neg	HT+D

Explanations to Table 2. HT, D and CKD meaning is the same as in Table 2. Albumin concentration values are multiplied by the factor 10; Neg means a negative result indicated by the strips method.

We have achieved a rather good correlation between the Roche laboratory assays of proteins and our sensor data (p. *4.3* and, particularly, Table 2). This fact gives a perspective for the development and practical use of the proposed method. Nevertheless, the deviations between the laboratory and our data are sometimes remarkable and they need to be explained. One of the discrepancy sources can be the phenomenon established in [8] and, namely, that small peptides do not at all produce signals with the Roche assays and Tamm-Horsfall protein gives a weak reaction. This can, in principle, explain why our sensor values for patients 9 and 16 (Table 2) are higher than the corresponding laboratory ones.

On the other hand, the same logic is valid in another aspect: not all non-albumin proteins must have high and equal absorption coefficients at 285 nm. It is possible that some non-albumin proteins produce strong Roche assay signals and have a lowered optical absorption coefficient (see also *5.2*). The matter has to be clarified in details in the way of concrete identification of all non-albumins actually present in the urine samples under investigation and establishing the correlation between the absorption spectra of the definite non-albumins and their correspondence to the Roche or other automated assays signals. This could be the aim for the further studies which could be also more extensive and embrace a larger screening group. The question about the factor of light scattering in urine fractions should also be scrutinised.

We have calibrated our method in relation to the Roche method by fractionations with pH9.3 buffers with a complex composition (10 mM TRIS +150 mM NaCl +2 mM EDTA) (see *3.2*). For the wide practical use can be, however, more appropriate the standard physiological fluid, i.e., salt water (0.9 wt % NaCl). A number of fractionations with salt waters have been done with positive results (see *3.2*) but the full-scale recalibration should be done in the development of this method.

5.2 Real proteinuria

To our best knowledge earlier the protein/albumin ratio was not used extensively for proteinuria analysis. We have here usefully involved it and can give one more argument to confirm the usefulness of this parameter.

We can suppose that the readings s of our optical absorption sensor depend, primarily, on the concentration of non-albumin proteins p and albumin a, i.e., $s = n\,(p + a)$, where n is the adjusting coefficient. We have in reality the laboratory data on protein / albumin ratios or $(p + a) / a$, what we designate as $(p + a)/a = m$. With use of the empirical m values from Table 2 we get the equation of only one variable p:

$$s = n\,(p + p / (m\text{-}1)). \qquad (7)$$

For our focus group $m_{mean} = 17.8$ and the second member $p / (m\text{-}1)$ in eq. 7 is in the most cases very small. That is rather negligible for the patients 1, 3, 7 ($m > 29$). It means that our sensor is responsive overwhelmingly to the non-albumin proteins. This gives one more argument to say that we are dealing just with proteinuria, especially, in our focus group. Therefore our sensor can serve as a real proteinuria sensor. This

matter needs and deserves further attention to establish direct correlation between the individual non-albumins and sensor readings.

Our method correlates with the well-known and widely used in industry and laboratories method of certification of proteins mixture solutions. The measurement of the UV absorbance at a chosen wavelength from the range 277 – 280 nm is being carried out. It is recommended for 1% solutions to use a single averaged extinction coefficient ε = 10 "for a mixture of many different proteins" [24]. We did the same and considered the mix of abundant urine proteins as a (quasi)homogenous substance. By advancing of this method one should take into account the differences in extinction coefficients for separate proteins: ε = 5.8 (human albumin) [25], 10.8 (Tamm-Horsfall) [26], 13.8 (γ-Globulins) [27], 14.6 (Bence-Jones) [28] and search for distinct correlations between absorbance and the composition of typical urine proteins. This work was out of the scope of the present investigation and can be undertaken in the future.

It seems that the acknowledged reference values for identification of abnormalities can be too high. For instance, all patients 3, 7, 9, 12 with the CKD (Fig.7 and Table 1) had albumin/creatinine values smaller than the low limit of normality range 3 mg/mmol given in the guidelines [2]. The protein/creatinine reference value for indications of abnormalities by the Roche technology is > 0.200 g/g (>22.6 mg/mmol) and that is also too high. In our focus group only the patient 15 had once a higher ratio protein/creatinine (0.228 g/g) and this was, most probably, a transient proteinuria case.

5.3 With creatinine or without it?

We have seen that the predictable power of the markers involving creatinine concentrations has turned out to be weaker than the appropriate protein and protein/albumin parameters free of creatinine (the case of the patient 9 (Fig. 7&8 and Tables 1&2). We acknowledge that our statistics is not rich and needs to be enlarged. Nevertheless, one can draw some additional facts and speculate a little bit why the use of creatinine data is not always profitable, can be excessive and bear unnecessary costs.

It is clear without saying that for a given specimen of some biofluid the ratios albumin/creatinine and protein/creatinine have the larger uncertainties (or standard deviations) than the single albumin and protein magnitudes. Moreover, earlier there were carried out profiled investigations in the respect to the creatinine data stability for the human plasma and serum [29] and hemodialysate [30]. It was found that the creatinine concentration assay data can fluctuate depending on the store conditions and time intervals more than those of the other metabolites. In the recent paper [31] it was established that the diagnostic accuracy of the urine protein/creatinine ratio depends on urine concentration. Therefore we think that such a creatinine-free approach can be plausible and useful. The stabile ratios protein/albumin could be used in parallel or even replace the markers with creatinine involvement at least in the low level proteinuria region.

5 Conclusion

As the result of the performed study we would like to propose a new method of screening and monitoring for the low level proteinuria. This straightforward method can be exploited easily in work "in the field", i.e. outsides of the automated laboratories. The determination of protein concentration is based on the measurement of the UV (285 nm) absorption in fractions of urine eluted using the commercial columns PD-10 and specially designed optical cell. The applied standard urine test strips method failed to indicate in 94% cases any presence of proteins in the urines in the patients' focus group whereas the proposed method, in the parallel comparison, gave the correct positive results. One more advantage of the new method over the strips method is the possibility to use that in the wide region of protein concentrations from the normal proteinuria (≤ 0.1 g/L) up to the levels of severe proteinuria (~10 g/L). The trials in the larger screening groups and clinical tests are under preparation with the aim to elaborate the screening and monitoring algorithms.

6 Ethics

The study has been approved by the Ethics Committee on Human Research of the University of Tartu, Estonia (protocol no 232/M-8(1) 2013 and 244/M-25, 2015).

7 Acknowledgments

We thank Mrs. Mare Säde for very useful participation in this work. The partial financial support of the Foundation EAS (Estonia) is also sincerely acknowledged.

The stress-related changes in the cerebral blood flow in newborn rats with intracranial hemorrhage: metabolic and endothelial mechanisms

Olga Sindeeva[1*], Ekaterina Borisova[2], Arkady Abdurashitov[1], Ekaterina Zhinchenko[1], Artem Gekalyuk[1], Maria Ulanova[1], Aly Esmat Sharif[1], Victoria Razubaeva[1], Sergey Serov[1], Ludmila Yankovskaya[3], Valery Tuchin[1,4], Oxana Semyachkina-Glushkovskaya[1]

[1] National Research Saratov State University, Astrakhanskaya Str. 83, Saratov 410012, Russia
[2] Institute of Electronics, Bulgarian Academy of Sciences, Tsarigradsko Chaussee 72, Sofia 1784, Bulgaria
[3] Grodno State Medical University, Maxima Gorkogo Str. 80, Grodno 230009, Belorus
[4] Laboratory of Biophotonics, Tomsk State University, Tomsk 634050, Russia

[*] **e-mail:** mouse-oa@rambler.ru

Abstract. Neonatal brain hemorrhages is a major problem of future generation's health due to the high rate of cognitive disability of newborns after vascular catastrophes in the brain. Despite the public health impact of neonatal brain hemorrhages, the mechanisms underlying in these pathological processes remain unknown. Here, using a model of sound-stress-induced brain hemorrhages (per diapedesis, no per rhexis) in newborn rats and optical methods, we found that brain hemorrhages in newborn rats are accompanied by the increase in perfusion of brain tissues, which closely associated with reducing of cerebral oxygenation and increasing of nitric oxide production in both the brain tissues and blood. We assume that nitric oxide contributes the dilation of cerebral vessels during hypoxia and the increasing of cerebral blood flow in newborn rats with brain hemorrhages. Hypoxic-hyperperfusion during stress-related hemorrhages in newborn animals can be an important protective mechanism against anoxia and critical changes in cerebral hemodynamics. © 2016 Samara State Aerospace University (SSAU).

Keywords: speckle laser contrast imaging, oxygen saturation, stress-related intracranial hemorrhages, hypoxia, nitric oxide.

Paper #2804 received 2015.12.10; revised manuscript received 2015.12.30; accepted for publication 2015.12.31; published online 2016.02.02.

References

1. V. J. Rooks, J. P. Eaton, L. Ruess, G. W. Petermann, J. Keck-Wherley, and R. C. Pedersen, "Prevalence and evolution of intracranial hemorrhage in asymptomatic term infants," AJNR Am J Neuroradiol 29(6), 1082-1089 (2008).
2. T. Takenouchi, E. Kasdorf, and M. Engel, "Changing pattern of perinatal brain injury in term infants in recent years," Pediatr Neurol 46(2), 106-110 (2012).
3. A. J. Brouwer, F. Groenendaal, and C. Koopman, "Intracranial hemorrhage in full-term newborns: a hospital-based cohort study," Neuroradiol 52(6), 567-576 (2010).
4. S. Siu, N. S. Kwong, and K. T. So, "A 10-year Review of intracranial hemorrhage in term neonates," HK J Peadiatr (new series) 11(2), 140-146 (2006).
5. B. S. Jhawar, A. Ranger, D. A. Steven, and R. F. Del Maestro, "A follow-up study of infants with intracranial hemorrhage at full-term," Can J Neurol Sci 32(3), 332-339 (2005).
6. S. N. Gupta, A. M. Kechli, and U. S. Kanamalla, "Intracranial hemorrhage in term newborns: management and outcomes," Pediatr Neurol. 40(1), 1-12 (2009).
7. E. H. Whitby, P. H. Griffiths, S. Rutter, M. F. Smith, A. Spriqq, P. Ohadike, N. P. Davies, A. S. Rigby, and M. N. Paley, "Frequency and natural history of subdural heamorrhages in babies and relation to obstetric factor," Lancet 363(9412), 846-851 (2004).

8. C. B. Looney, J. K. Smith, L. H. Merck, H. M. Wolfe, N. C. Chescheir, R. M. Hammer, and J. H. Gilmore, "Intracranial hemorrhage in asymptomatic neonates: prevalence on MR images and relationship to obstetric and neonatal risk factors," Radiology 242(2), 535-541 (2007).
9. S. Maccari, M. Darnaudery, S. Morley-Fletcher, A. R. Zuena, C. Cinque, and O. Van Reeth, "Prenatal stress and longterm consequences: implications of glucocorticoid hormones," Neurosci. Biobehav 27(1-2), 119–127 (2003).
10. C. Mirescu, J. D. Peters, and E. Gould, "Early life experience alters response of adult neurogenesis to stress," Nat. Neurosci 7(8), 841–846 (2004).
11. P. Ballabh, "Intraventricular hemorrhage in premature infants: mechanism of disease," Pediatr Res 67(1), 1-8 (2010).
12. O. Semyachkina-Glushkovskaya, T. Anishchenko, S. Kapralov, R. Novikov, and K. Skvorcov, "Sex differences in cardiovascular control by nitric oxide in normotensive and hypertensive rats at rest and during stress," Health 2(8), 897-905 (2010).
13. T. G. Anishenko, O. V. Semyachkina-Glushkovskaya, and V. A. Berdnikova "Effect of age and sex on renal hypertension and concentration of nitric oxide in the blood of albino rats," Bulletin of Experimental Biology and Medicine 149(1), 1-4 (2010).
14. R. Hlatky, J. C. Goodman, A. B. Valadka, and C. S. Robertson, "Role of Nitric Oxide in Cerebral Blood Flow Abnormalities After Traumatic Brain Injury," Journal of Cerebral Blood Flow & Metabolism 23(5), 582-588 (2003).
15. P. J. Goadsby, H. Kaube, and H. L. Hoskin, "Nitric oxide synthesis couples cerebral blood flow and metabolism," Brain Res 595(1), 167–170 (1992).
16. C. Iadecola, and F. Zhang, "Permissive and obligatory roles of NO in cerebrovascular responses to hypercapnia and acetylcholine," Am J Physiol 271(4 Pt.2), R990–R1001 (1996).
17. Committee for the Update of the Guide for the Care and Use of Laboratory Animals, Institute for Laboratory Animal Research, Division on Earth and Life Studies, National Research Council of the National Academies, "Guide for the care and use of laboratory animals. 8th edition," Washington, The National Academies Press (2011).
18. O. Semyachkina-Glushkovskaya, A. Pavlov, J. Kurths, E. Borisova, A. Gisbrecht, O. Sindeeva, A. Abdurashitov, A. Shirokov, N. Navolokin, E. Zinchenko, A. Gekalyuk, M. Ulanova, D. Zhu, Q. Luo, and V. Tuchin, "Optical monitoring of stress-related changes in the brain tissues and vessels associated with hemorrhagic stroke in newborn rats," Biomedical Optics Express 6(10), 4088-4097 (2015).
19. O. Semyachkina-Glushkovskaya, V. Lychagov, O. Bibikova, I. Semyachkin-Glushkovskiy, S. Sindeev, M. Kassim, H. Braun, F. Al-Fatle, L. Al Hassani, and V. Tuchin, "The experimental study of stress-related pathological changes in cerebral venous blood flow in newborn rats assessed by DOCT," Journal of Innovative Optical Health Science 6(3), 1-9 (2013).
20. A. Pavlov, O. Semyachkina-Glushkovskaya, Z. Yang, O. Bibikova, O. Pavlova., Q. Huang, D. Zhu, P. Li, V. Tuchin, and Q. Luo "Multiresolution of pathological changes in cerebral venous dynamics in newborn mice with intracranial hemorrhage: adrenorelated vasorelaxation," Physiol. Meas 35(10), 1983-1999 (2014).
21. A. Abdurashitov, V. Lychagov, O. Sindeeva, O. Semyachkina-Glushkovskaya, and V. Tuchin, "Histogram analysis of laser speckle contrast image for cerebral blood flow monitoring," Frontiers of Optoelectronics 8(2), 187-194 (2015).
22. A. K. Dunn, "Laser speckle contrast imaging of cerebral blood flow," Annals of biomedical engineering 40(2), 367-377 (2012).
23. F. Domoki, D. Zölei, O. Oláh, V. Tóth-Szűki, B. Hopp, F. Bari, and T. Smausz, "Evaluation of laser-speckle contrast image analysis techniques in the cortical microcirculation of piglets," Microvascular research 83(3), 311-317 (2012).
24. N. Liu, X. Cui, D. M. Bryant, G. H. Glover, and A. L. Reiss, "Inferring deep-brain activity from cortical activity using functional near-infrared spectroscopy," Biomed. Opt. Express 6(3), 1074-1089 (2015).
25. T. Alderliesten, P. M. Lemmers, J. J. Smarius, R. E. van de Vosse, W. Baerts, and F. van Bel, "Cerebral oxygenation, extraction, and autoregulation in very preterm infants who develop peri-intraventricular hemorrhage," J. Pediatr 162(4), 698-704 (2013).
26. G. A. Taylor, "New concepts in the pathogenesis of germinal matrix intraparenchymal hemorrhage in premature infants," AJNR Am. J. Neuroradiol 18(2), 231-232 (1997).
27. G. A. Taylor, W. H. Trescher, M. V. Johnston, and R. J. Traysman, "Experimental neural injury in the newborn lamb: a comparison of NMDA receptor blockade and nitric oxide synthesis inhibition on lesion size and cerebral hyperemia," Pediatr Res 38(5), 644-651 (1995).
28. G. Hambleton, and J. S. Wigglesworth, "Origin of intraventricular hemorrhage in the preterm infant," Arch Dis Child 51(9), 651-659 (1976).

29. J. M. Valdueza, F. Doepp, S. J. Schreiber, B. W. van Oosten, K. Schmierer, F. Paul, and M. P. Wattjes, "What went wrong? The flawed concept of cerebrospinal venous insufficiency," J. Cereb. Blood Flow Metab 33(5), 657-668 (2013).
30. A. Michoulas, S. N. Basheer, E. H. Roland, K. Poskitt, S. Miller, and A. Hill, "The role of hypoxia ischemia in term newborns with arterial stroke," Pediatr Neurol 44(4), 254-258 (2011).
31. P. Bodin, and G. Burnstock, "Synergistic effect of acute hypoxia on flow-induced release of ATP from cultured endothelial cells," Experientia 51(3), 256-259 (1995).
32. Y. Tomiyama, J. E. Brian, and M. M. Todd, "Cerebral blood flow during hemodilution and hypoxia in rats: role of ATP-sensitive potassium channels," Stroke 30(9), 1942-1948 (1999).
33. T. Kiliç, and A. Akakin, "Anatomy of cerebral veins and sinuses," Front Neurol Neurosci 23, 4-15 (2008).
34. J. Volpe, "Intracranial hemorrhage: Germinal matrix hemorrhage," in Neurology of the Newborn, 5th edition Philadelphia, PA, Saunders Elsevier (2008). ISBN: 978-1-4160-3995-2.

1 Introduction

Neonatal brain hemorrhages (BH) are among the top ten causes of development of significant cognitive disability (42%-85% of those who survive) in newborns [1-5]. It was believed that BH is typical only for pre-term newborns and is uncommon among term neonates because the incidence of BH in them is difficult to diagnose due to absence of clear symptoms [6]. However, two magnetic resonance imaging studies of asymptomatic term newborns found 8% (0.2T, 110 neonates) and 26% (3T, 88 neonates) incidence of BH after vaginal delivery [7, 8]. These results show that BH in term newborns is much more frequent that earlier assumed.

The reasons and mechanisms underlying BH are difficult to determine. Potential risk factors for BH are still poorly studied. Some studies report an association between assisted deliveries and BH in neonates, but those results are not consistent [1, 7, 8]. Such risk factors as hypertension, smoking, diabetes, atherosclerosis are not suitable for neonates. It is assumed that stress as the main process of adaptation to the environment is a crucial risk factor for BH in neonates, but the mechanism of stress-related BH is unclear [9, 10].

In this experimental study on three-day-old rat pups, we aimed to determine the mechanisms underlying stress-induced BH. With this aim, we focused on different levels of the cascade of stress responses: systemic (monitoring of cerebral blood flow - CBF), metabolic (assessment of oxygen saturation of the brain tissues) and molecular (evaluation of nitric oxide content in the brain and blood). Our choice of experimental tasks is caused by main actual questions related to the stress-induced cerebrovascular catastrophes. Many studies showed that abnormalities of the CBF, including fluctuations in the CBF, provide a considerable contribution to BH in newborns [11]. Nitric oxide is a main factor of vascular stress-reactivity and resistance to traumatic stress [12-14]. In the central nervous system, NO participates in the regulation of CBF and in the cerebrovascular responses to metabolic activity and to hypercapnia [15, 16]. But, the exact role of these processes in neonatal BH, especially, in aspect of stress accompanying the birth is not established yet and needs to be thoroughly studied.

2 Materials and Methods

Experiments were performed out in newborn mongrel rats 3 days old. All procedures were performed in accordance with the "Guide for the Care and Use of Laboratory Animals" [17]. The experimental protocol was approved by the Committee for the Care and Use of Laboratory Animals at Saratov State University (Protocol H-147, 17.04.2001).

To induce hemorrhagic stroke, the following protocol of sound stress's impact was used (120 dB, 17 Hz): 10 sec – sound, then 60 sec – pause. This cycle repeated during 2 h [18-20].

For measurement of cerebral circulation, the anesthetized rats (isoflurane – inhalant anesthetic) with fixed head and scalp incision (the dura was left intact) were immobilized. Anesthetic depth was assessed by periodically monitoring the rear foot reflex.

To assess the stress-related changes in cerebral hemodynamics, we studied the changes in relative cerebral blood flow (rCBF or perfusion) using a home-made system for laser speckle contrast imaging (LSCI). The raw speckle images were recorded under the following conditions: light source – HeNe laser with the wavelength 632.8 nm; image sensor – CMOS camera Basler acA2500-14gm; imaging lens – Computer M16140-MP2 16 mm at F-number equal to 6, that corresponds to speckle/pixel size ratio of around 2; exposure time – 20 ms. The speckle images were recorded for 3 min at an average frame rate of 40 frames per second. Spatial speckle contrast was calculated as, $K = \sigma/\langle I \rangle$, where σ is the standard deviation of intensity fluctuations and $\langle I \rangle$ is the mean intensity within a 5x5 sliding window. 50 consecutive frames were averaged into one speckle contrast image.

The measurement of cerebral circulation was performed through the fontanel of newborn rats with focus on:

1) the superior sagittal sinus, which is one of four major sinuses collecting blood from the small veins of the brain;

2) the small, optically unresolvable vessels surrounding the sagittal sinus. Information about macro-

(the sagittal sinus) and microcirculation (capillaries, arterioles, venules) was extracted simultaneously.

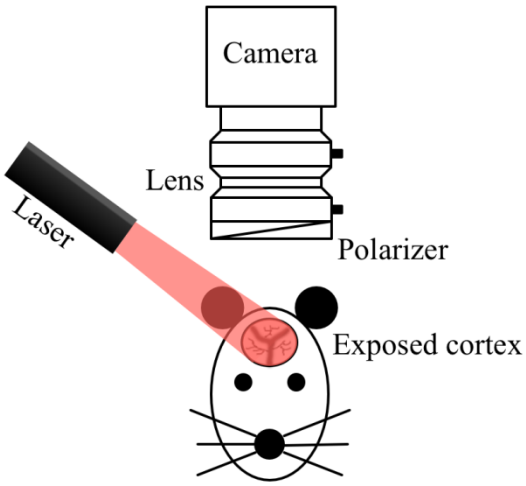


Fig. 1 LSCI system.

Acquisition information from resulting images about flow indexes and vessel's differentiation was performed by histogram analysis of ROI (region of interest). Detailed information about this algorithm and calculation of speckle contrast from raw images itself was explained in our early published article [21] but briefly explanation is following: it was shown several times [22, 23] that conventional LSCI system can sense integral erythrocytes motions even in optically unresolvable vessels. Therefore, if we overlay large enough ROI on speckle image (ROI should contain vessels of different caliber and even unresolvable ones) in resulting histogram we can observe clear peaks. Those peaks are related to different vessels with various diameters. By analysis of this histogram and matching each peaks to a specific collection of vessels with particular diameter we can differentiate venous and microcirculatory components in real time during experiments. In this study rCBF was set to reciprocal of speckle contrast.

The changes in oxygen saturation are often associated with the brain injures and are an important for evaluation of severity of these injures [24]. To measure oxygen saturation level (SpO_2) in the brain tissue we used pulse oximeter model CMS60D (Contec Medical Systems Co., Ltd., Qinhuangdao, China). The system is characterized with a small volume, easy-to-use operation and portability, which make it very convenient for the detection of blood hemoglobin oxygen saturation levels of small laboratory animals. Optical sensor is based on dual wavelengths pulse oximetry approach, using 660 nm and 880 nm for the SpO_2 detection. Display screen of the system could directly show the measured values of the pulse oxygen saturation and pulse rate. Using USB standard for data transmission the measurements could be also visualized on a personal computer using software SpO_2 Assistant version 2.7.0. (Contec Medical Systems Co., Ltd., Qinhuangdao, China). The software allows as well to store the data in ASCII format for a further analysis.

The content of NO (*in vitro*) in serum and cerebral tissues (cerebral cortex, cerebellum, hippocampus, brain axis) was determined by the presence of nitrite. The rats were decapitated, the blood samples were collected, the brain was carefully removed and homogenized. Staining was performed using the Griess reagent-Ilosvaya. The color intensity is measured with a spectrophotometer (SF-2000 Bio, Saint Petersburg, Russia, 2002) at fixed wavelength of 538 nm.

2.1 The protocol of experiments

The basal values of SpO_2 and rCBF were performed in each healthy newborn rats (n=24). Afterward, each rat underwent to sound stress during 2h. Next day after stress when brain hemorrhages developed, we performed the recording of rCBF and SpO_2 in the same newborn rats (n=24). Thus, animals were divided into two groups:

1) intact, unstressed newborn rats (the control group);

2) stressed rats 24 h after stress-off.

The measurement of NO content in the brain tissues and in blood was carried out on other newborn rats: the control group including healthy newborn rats (n=24) and the stressed group (n=24) including newborn rats 24h after stress with brain hemorrhages.

The results were reported as mean ± standard error of the mean (SEM). Differences from the initial level in the same group were evaluated by the Wilcoxon test. Intergroup differences were evaluated using the Mann-Whitney test and ANOVA-2 (post hoc analysis with the Duncan's rank test). Significance levels were set at $p < 0.05$ for all analyses.

3 Results

3.1 Stress-induced changes in the cerebral blood flow in newborn rats with brain hemorrhages

At the first step of our work, we analyzed the stress-induced changes in perfusion and capacitive sectors of cerebral circulation associated with BH in newborn rats using LSCI system.

The sound stress induced the development of small BH (average size 0.005 mm^2) in the cortex and subcortical tissues per diapedesis (no per rhexis), i.e. separated red blood cells squeezed out of the functionally damaged venous vessel walls. Figure 2 (in the right) demonstrates a typical example of diapedesis BH in the subcortical tissues in newborn rat. All rats survived after sound stress, there were no dead newborn rats. Note, that human newborns with BH demonstrate

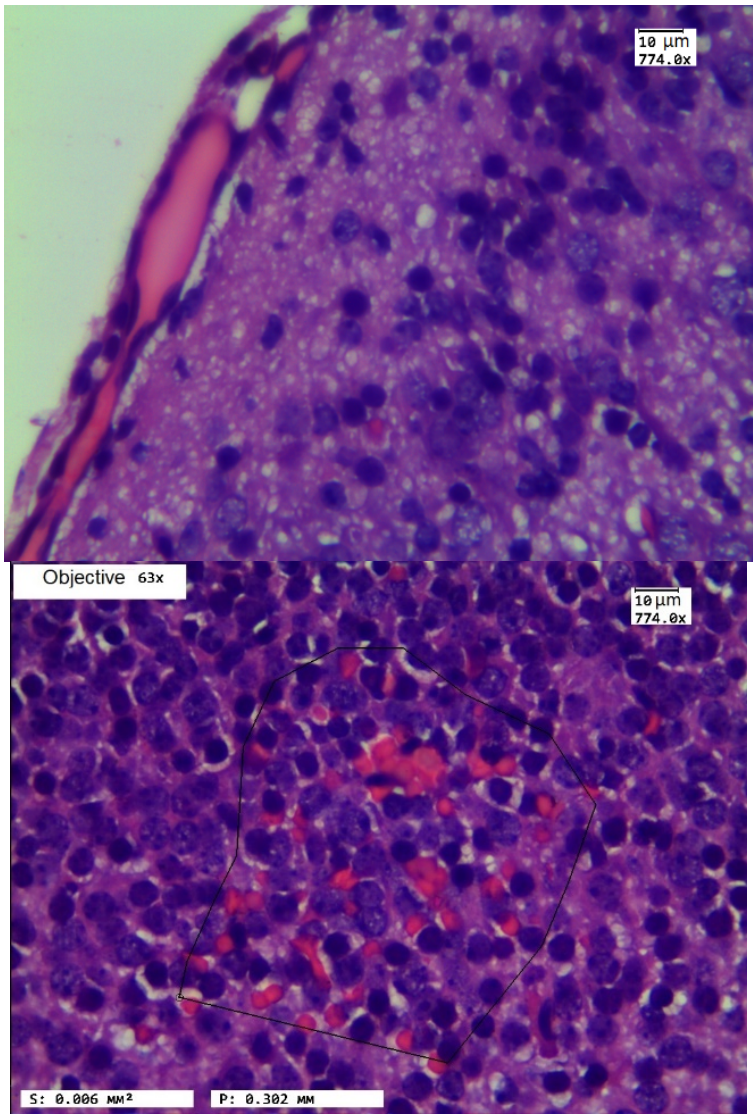


Fig. 2 The typical example of diapedesis (no per rhexis) brain hemorrhage (in the right) in newborn rat (the subcortical area). The normal subcortical tissue of newborn rat from the control group is shown in the left. Hematoxylin & Eosin staining. Bars represent 10 µm (774.0X).

high survives after such brain injures but with long lasting cognitive disorders [1-5]. The one of possible explanation of this fact is the location of brain hemorrhages in neonates who have usually vascular catastrophes in the cortex, i.e. not in the deep important brain centers controlling vital functions such as heartbeats, breathing and etc. [3,6]. Therefore, the consequences of BH in the intellectual zone of the brain might not be recognized for many years [1-5].

LSCI results showed that newborn rats with BH vs. healthy animals demonstrated an increased rCBF in both level of venous and microcirculatory components of cerebral circulation. But, the changes in the sagittal sinus was more pronounced than those in microvessels (Fig. 3). Indeed, after stress exposure rCBF increased in newborn rats by 53±3% ($p<0.05$) in the sagittal sinus and by 29±4% ($p<0.05$) in microvessels. In our previous study we also obtained that stress-reactivity of cerebral veins are greater than vessels of microcirculatory bed [18].

3.2 Stress-induced changes in blood oxygen saturation of the brain tissues in newborn rats with brain hemorrhages

At the second step of this investigation, we studied the metabolic component of cerebral circulation using the assessment of SpO_2 of the brain tissues. The results of this series of experiments showed that the stress-related changes in the CBF in newborn rats was associated with reduced of SpO_2 in the brain. The following SpO_2 levels averaged for all animals were obtained: 98.1±0.3% in the control group and 76.5±3.0% ($p<0.05$) in newborn rats with BH. Thus, the stress-induced pathological changes in the cerebral circulation was associated with reducing of SpO_2 by 22% ($p<0.05$) compared with normal state (Fig. 4).

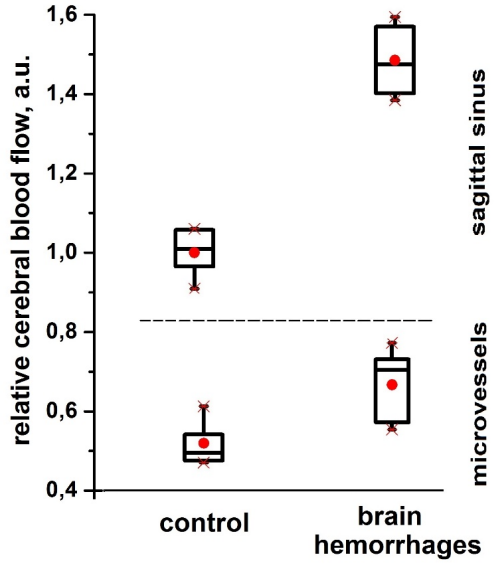


Fig. 3 The relative cerebral blood flow (a.u.) assessed by LSCI in the sagittal sinus and in the microvessels in healthy newborn rats (the control group) and in newborn rat with brain hemorrhages.

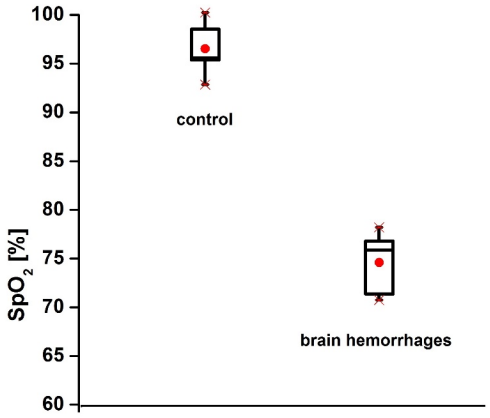


Fig. 4 The SpO_2 (%) in the brain tissues in healthy newborn rats (control group) and newborn rat with brain hemorrhages.

3.3 Stress-induced changes in NO production in the blood and brain tissue in newborn rats with brain hemorrhages

At the third step of this work, we analyzed endothelial component of cerebral circulation using spectrophotometric assessment of NO production in the blood and brain tissues in healthy newborn rats (the control group) and in newborn animals with BH.

The results demonstrated that the increased rCBF and hypoxia, which we obtained in newborn rats with BH in the first and second parts of this work, were associated with the increase in NO content in all investigated zoned of the brain as well as in the blood (Table 1). So, NO level in newborn rats with ICH was higher in the cortex, cerebellum, hippocampus, brain axis, and in the blood compared with healthy animals.

Table 1 Stress-induced changes in NO (μg/ml) production in the blood and brain tissues in healthy (the control group) and with BH newborn rats.

	healthy newborn rats	newborn rats with ICH
cortex	0.23±0.02	0.36±0.03*
cerebellum	0.27±0.03	0.32±0.02*
hippocampus	0.22±0.04	0.31±0.05*
brain axis	0.20±0.03	0.28±0.02*
blood	0.30±0.07	0.48±0.05*

$p<0.05$ vs.: * - healthy newborn rats (control group)

4 Discussion

Here we studied the stress-induced changes in the brain tissues and vessels associated with BH in newborn rats using LSCI assessment of perfusion (microvessels) and capacitive (the sagittal sinus as a main cerebral vein) components of cerebral circulation as well as a measure of metabolic (SpO_2 in the brain tissues) and endothelial (level of NO in the brain tissues and in the blood) factors in the regulation of cerebral blood flow.

Our results show that the stress-induced development of BH in newborn rats is accompanied by the increase in rCBF in both level of microvessels and venous zones of cerebral circulation. These results are consistent with clinical data suggesting that hyperperfusion is one of mechanisms responsible for brain hemorrhages [25-27]. However, separate LSCI analysis of venous and microcirculatory components of cerebral circulation shows that the maturation of changes in the sagittal sinus were more pronounced than in microcirculatory network (53±3% vs. 29±4%, $p<0.05$). This fact is according with our previous histological data, which showed that the venous vessels are more sensitive to harmful effect of stress than microvessels [18]. In clinical studies also have been shown that neonatal stroke is primary venous infarction due to a weakness of the wall of cerebral veins in neonates [28].

We assume that the increase in rCBF in the area of microvessels is the consequence of congestion of blood in the cerebral veins and the decreasing of blood outflow from the brain. In our previous histological data [18-20] we showed that the brain hemorrhages in newborn rats are associated with the increase in size of cerebral veins due to accumulation of extensive blood in them. These changes are associated with formation of perivascular edema, i.e. fluid pathway from the vessels. The relaxation of cerebral veins with perivascular edema are markers of accumulation of extensive blood in venous system and suppression of blood outflow from the brain leading to venous insufficiency [29].

The hypoxia is one of main reasons for critical venous pathological changes associated with brain hemorrhages in newborns [30]. Our results suggest that stress-induced increase in rCBF is accompanied by

reduction of SpO_2 in the brain tissues. Notice, that the hypoxic-hyperperfusion is described also in other studies [31, 32]. A normal physiological response to reduction of oxygen delivery is relaxation of cerebral vessels that activates metabolism in the brain tissues via the increasing of CBF. The particularities of cerebral veins are no muscles and valves in their thin walls, therefore, they have low resistance to critical stretching occurring during blood accumulation in them [33]. The immature brain vessels of newborns have limitation in vasorelaxation capabilities (increase of vessel size). The hypoxia-induced vasorelaxation of cerebral veins causes increasing of cerebral venous pressure [34]. This high pressure can induce easily the rupture of thin walls of immature cerebral veins of newborns [28].

To better understanding of mechanisms underlying relaxation of cerebral vessels during hypoxia in newborn rats with BH, we studied the role of NO in these processes. Our choice of this vascular factor is caused by the fact that NO is a vasodilator, in the central nervous system, NO participates in the regulation of CBF and in the cerebrovascular responses to metabolic activity and to hypercapnia [15, 16]. Thus, NO is complex endothelial factor, which is involved in many levels of regulation of cerebral hemodynamics as well as NO is a key endothelial factor for regulation of vascular tone during stress [12-14].

We show that the stress-induced hypoxic-hyperperfusion in the brain tissues in newborn rats with BH is associated with increasing of NO level in the blood and cerebral tissues. The increase NO concentration was the same in different zones of the brain. But, the serum NO level was higher than in the brain that it is possible to explain by the stress-induced increase in NO synthesis in the vessels of all inner organs. In our previous results, we found that the stress-induced increase in NO serum level is a protective mechanism against the significant pressure effect of stress [12, 13]. Others also demonstrate that the increase of production of major endothelial relaxant such as NO is one of protective mechanism responsible for increasing of tissue perfusion during hypoxia [32]. Taking into account these data, we believe that the elevated level of NO in the brain and blood is the vascular protective response to hypoxia as mechanism of compensation of oxygen deficiency via the increase in perfusion of brain tissues.

5 Conclusion

In summary, our results suggest that stress-induced ICH in newborn rats is accompanied by the increase in perfusion of brain tissues, which closely associated with reducing of SpO_2 in the brain tissues and increasing of NO production in both the brain tissues and blood. We assume that NO as a major endothelial vasorelaxant may contribute dilation of cerebral vessels under hypoxia that explains the increase in rCBF in newborn rats with ICH. Thus, hypoxic-hyperperfusion during stress-related hemorrhages in newborn animals can be an important protective mechanism against anoxia and critical changes in cerebral hemodynamics.

Acknowledgments

This work is supported by Grant of Russian Science Foundation № 14-15-00128.

Software development for estimation of optical clearing agent's diffusion coefficients in biological tissues

Pedro Peixoto[1], Luís Oliveira[1,2,3*], Maria Inês Carvalho[2,4], Elisabete Nogueira[1,3], Valery V. Tuchin[5,6,7]

[1] Physics Department – Polytechnic Institute of Porto, School of Engineering, Rua Dr. António Bernardino de Almeida, 431, 4200-072 Porto, Portugal

[2] FEUP – University of Porto, Rua Dr. Roberto Frias, 4200-465 Porto, Portugal

[3] CIETI – Centre of Innovation in Engineering and Industrial Technology, ISEP, Rua Dr. António Bernardino de Almeida, 431, 4200-072 Porto, Portugal

[4] DEEC/FEUP and INESC TEC, University of Porto, Rua Dr. Roberto Frias, 4200-465 Porto, Portugal

[5] Research-Educational Institute of Optics and Biophotonics, Saratov National Research State University, 83 Astrakhanskaya str., Saratov 410012, Russia

[6] Laboratory of Laser Diagnostics of Technical and Living Systems, Institute of Precise Mechanics and Control RAS, 24 Rabochaya str., Saratov 410028, Russia

[7] Interdisciplinary Laboratory of Biophotonics, Tomsk National Research State University, 36 Lenin's av., Tomsk 634050, Russia

[*] **e-mail:** lmo@isep.ipp.pt

Abstract. The study of chemical diffusion in biological tissues is a research field of high importance and with application in many clinical, research and industrial areas. The evaluation of diffusion and viscosity properties of chemicals in tissues is necessary to characterize treatments or inclusion of preservatives in tissues or organs for low temperature conservation. Recently, we have demonstrated experimentally that the diffusion properties and dynamic viscosity of sugars and alcohols can be evaluated from optical measurements. Our studies were performed in skeletal muscle, but our results have revealed that the same methodology can be used with other tissues and different chemicals. Considering the significant number of studies that can be made with this method, it becomes necessary to turn data processing and calculation easier. With this objective, we have developed a software application that integrates all processing and calculations, turning the researcher work easier and faster. Using the same experimental data that previously was used to estimate the diffusion and viscosity of glucose in skeletal muscle, we have repeated the calculations with the new application. Comparing between the results obtained with the new application and with previous independent routines we have demonstrated great similarity and consequently validated the application. This new tool is now available to be used in similar research to obtain the diffusion properties of other chemicals in different tissues or organs. © 2016 Samara State Aerospace University (SSAU).

Keywords: collimated optical transmittance, chemical diffusion in tissues, glucose, optical clearing, refractive index matching, thickness variation, viscosity, software application.

Paper #2815 received 2015.12.17; revised manuscript received 2015.12.30; accepted for publication 2015.12.31; published online 2016.02.05.

References

1. F. E. Dunlap, O. H. Mills, M. R. Tuley, M. D. Baker, and R. T. Plott, "Adapalene 0.1% gel for the treatment of acne vulgaris: its superiority compared to tretinoin 0.025% cream in skin tolerance and patient preference," British Journal of Dermatology 139(52), 17–22 (1998).
2. E. A. Genina, A. N. Bashkatov, Y. P. Sinichkin, I. Y. Yanina, and V. V. Tuchin, "Optical clearing of biological tissues: prospects of application in medical diagnostics and phototherapy," J. of Biomedical Photonics and Engineering 1(1), 22–58 (2015).
3. L. M. Alvarez, Compendium of Organ & Tissue Banking Concepts (2015).
4. R. Bertram, and M. Pernarowski, "Glucose diffusion in pancreatic islets of Langerhans," Biophys. J. 74(4), 1722–1731 (1998).
5. A. C. Ribeiro, O. Ortona, S. M. N. Simões, C. I. A. V. Santos, P. M. R. A. Prazeres, A. J. M. Valente, V. M. M. Lobo, and H. D. Burrows, "Binary mutual diffusion coefficients of aqueous solutions of sucrose, lactose, glucose and fructose in the temperature range from (298.15 to 328.15) K," J. Chem. Eng. Data 51(5), 1836–1840 (2006).
6. M. G. Ghosn, E. F. Carbajal, N. A. Befrui, V. V. Tuchin, and K. V. Larin, "Concentration effect on the diffusion of glucose in ocular tissues," Opt. Laser Eng. 46(12), 911–914, (2008).
7. L. M. Oliveira, M. I. Carvalho, E. M. Nogueira, and V. V. Tuchin, "The characteristic time of glucose diffusion measured for muscle tissue at optical clearing," Laser Physics 23(7), 075606 (2013).
8. A. N. Bashkatov, E. A. Genina, and V. V. Tuchin, "Measurement of glucose diffusion coefficients in human tissues," Chap. 19 in Handbook of Optical Sensing of Glucose in Biological Fluids and Tissues, V. V. Tuchin, (ed.), Taylor & Francis Group LLC, CRC Press, London, 587–621 (2009).
9. M. Kreft, M. Lukšič, T. M. Zorec, M. Prebil, and R. Zorec, "Diffusion of D-glucose measured in the cytosol of a single astrocyte," Cell. Mol. Life Sci. 70(8), 1483–1492 (2013).
10. L. Oliveira et al., "Optical clearing mechanisms characterization in muscle", to be published.
11. V. V. Tuchin, I. L. Maksimova, D. A. Zimnyakov, I. L. Kon, A. H. Mavlyutov, and A. A. Mishin, "Light propagation in tissues with controlled optical properties," J. Biomed. Opt. 2(4), 401–407 (1997).
12. V. V. Tuchin, Tissue Optics: Light Scattering Methods and Instruments for Medical Diagnosis, 3rd Ed., Bellingham: SPIE Press (2015).
13. V. V. Tuchin, Optical Clearing of Tissues and Blood, Bellingham, SPIE Press (2006).
14. E. A. Genina, A. N. Bashkatov, and V. V. Tuchin, "Tissue optical immersion clearing," Expert Rev. Med. Devices 7(6), 825–842 (2010).
15. K. Becker, N. Jährling, S. Saghafi, R. Weiler, and H-U. Dodt, "Chemical clearing and dehydration of GFP expressing mouse brains," PLoS One 7(3), e33916 (2012).
16. K. Becker, N. Jährling, S. Saghafi, and H-U. Dodt, "Dehydration and clearing of whole mouse brains and dissected hippocampi for ultramicroscopy," Cold Spring Harbour Protocol 2013(7), 683-684 (2011).
17. D. Zhu, K. V. Larin, Q. Luo, and V. V. Tuchin, "Recent progress in tissue optical clearing," Laser Photonics Rev. 7(5), 732-757 (2013).
18. L. M. Oliveira, M. I. Carvalho, E. M. Nogueira, and V. V. Tuchin, "Diffusion characteristics of ethylene glycol in skeletal muscle," J. Biomed. Opt. 20(5), 051019 (2015).
19. V. V. Larin, M. G. Ghosn, A. N. Bashkatov, E. A. Genina, N. A. Trunina, and V. V. Tuchin, "Optical clearing for OCT image enhancement and in-depth monitoring of molecular diffusion," IEEE J. Select. Tops. Quant. Electr. 18(3), 1244-1259 (2012).
20. J. Wang, Y. Zhang, P. Li, Q. Luo, and D. Zhu, "Review: Tissue optical clearing window for blood flow monitoring," IEEE J. Select. Tops. Quant. Electr. 20(2), 92-103 (2014).
21. O. Nadiarnykh, and P. J. Campagnola, "SHG and optical clearing," in Second Harmonic Generation Imaging, F. S. Pavone, and P. J. Campagnola (eds.), CRC Press, Taylor & Francis Group, Boca Raton, London, NY, 169−189 (2014).
22. E. A. Genina, A. N. Bashkatov, and V. V. Tuchin, "Glucose-induced optical clearing effects in tissues and blood," Chap. 21 in Handbook of Optical Sensing of Glucose in Biological Fluids and Tissues, V. V. Tuchin (ed.), Taylor & Francis Group LLC, CRC Press, London (2009).
23. A. Kotyk, and K. Janacek, Membrane Transport: An interdisciplinary Approach, Plenum Press, New York (1977). ISBN: 978-1-4684-3333-3.
24. H. Suhaimi, S. Wang. T. Thornton, and D. B. Das, "On glucose diffusivity of tissue engineering membranes and scaffolds," Chemical Engineering Science 126, 244–256 (2015).
25. J. M. Christensen, M. C. Chuong, H. Le, L. Pham, and E. Bendas, "Hydrocortisone diffusion through synthetic membrane, mouse skin and epiderm™ cultured skin," Archives of Drug Information 4(1), 10–21 (2011).
26. P. N. Skandamis, and G.-J. E. Nychas, "Preservation of fresh meat with active and modified atmosphere packaging conditions," Int. J. of Food Microbiology 79(1-2), 35–45 (2002).

27. G. H. Zhou, X. L. Xu, and Y. Liu, "Preservation technologies for fresh meat – A review," Meat Science 86(1), 119–128 (2010).
28. D. Tiroutchelvame, V. Sivakumar, and J. P. Maran, "Optimization of mass transfer parameters during osmotic dehydration of momordica charantia slices," J. of Food Processing and Preservation, (2015).
29. A. Bouchoux, H. Roux-de Balmann, and F. Lutin, "Nanofiltration of glucose and sodium lactate solutions: Variations of retention between single- and mixed-solute solutions," J. of Membrane Science 258(1-2), 123–132 (2005).

1 Introduction and theoretical background

The treatment of biological tissues and blood with chemical compounds is widely used in many applications of dermatology [1], clinical research [2], and tissue or organ preservation [3]. The efficiency of the treatment can be evaluated and quantified if the diffusion properties of the chemical used are known for the desired tissue. Some results have been reported for the diffusion time and diffusion coefficients of some chemical agents in specific biological tissues but the techniques used to evaluate these parameters are diverse [4-9].

The technique of optical immersion clearing is one method where the evaluation of the diffusion properties of the optical clearing agents in tissues is of most importance. By estimating those parameters, it is possible to evaluate the necessary time to turn the tissue more transparent and to quantify that transparency as a function of the agent concentration used to treat the tissue [10]. The optical immersion clearing technique is a method initially described in 1997 [11] and presents great potential to be applied in clinical applications that use optical diagnosis or treatment methods [2]. Such technique originates a decrease in the natural scattering coefficient and an increase of the natural scattering anisotropy factor of the tissue, creating a temporary transparency that can be later reversed [12-13]. Such temporary tissue transparency is obtained by a stimulated tissue dehydration and consequent replacement of the water in the interstitial space by a biocompatible agent that has a higher RI, better matched to the RI of the other tissue components [14-18]. Recent research work demonstrated that this technique can be used in vivo with imaging techniques such as optical coherence tomography [19], speckle methods to monitor blood flow in dermis or cortical tissues [20], and second harmonic generation imaging (SHG) to improve tissue depth and resolution [21]. These various studies have also demonstrated the reversibility of the treatments applied by assisted rehydration.

The mechanisms involved in this technique are designated tissue dehydration and refractive index (RI) matching that ultimately turn the tissue more organized internally, leading to a smaller light scattering [13]. Such treatment is completely reversible by natural rehydration in vivo and by assisted rehydration on ex vivo tissue samples [10]. The potential of the optical immersion clearing technique is very significant to be used with clinical procedures that apply light for diagnostic and treatment purposes [2, 7, 14].

Considering an *ex vivo* sample, as it is immersed in an aqueous solution containing a particular concentration of a biocompatible chemical agent, the agent in the solution creates an osmotic pressure over the sample, which induces water loss by the tissue. This is the dehydration mechanism, which initiates immediately as the treatment is applied to the tissue sample. This mechanism is in general fast, usually contained within the first two minutes of treatment [18]. At the same time, but with a slower pace, the agent in the solution begins to diffuse into the outer layers of the tissue [18]. The difference in viscosity properties and molecular size between water molecules and agent molecules provide that the diffusion of agent into deeper layers of tissue to create the RI matching mechanism takes a longer time [10].

Since these two mechanisms occur simultaneously at the beginning of the treatment, it is not easy to discriminate one from the other and time dependence measurements made during treatment represent the mixed global flux, which is a combination of the water flux out of the tissue and the OCA flux into the tissue. This way, the individualization of the two mechanisms needs a refined method that produces accurate results. Such a method is described in literature [8, 13] and we have recently proven its concept experimentally as described in our recent publications [7, 10, 18]. In those papers we describe how we have used thickness and collimated transmittance (T_c) measurements made from thin muscle samples under treatment with glucose and ethylene glycol (EG) solutions to estimate the diffusion time, diffusion coefficient and viscosity of these agents in muscle. Our research has produced additional results. Those additional results were the estimated diffusion properties of water inside the muscle [10, 18] and the amount of free water content in the natural muscle [7, 10].

Considering as an example a treatment of a slab-form tissue sample with a solution of a particular optical clearing agent (OCA), we can assume that if the solution has a significant higher volume than the sample (e.g. 10x), the OCA diffuses through both slab surfaces according to free diffusion. If the tissue sample has a thickness d, we can calculate the OCA concentration inside the tissue as a function of time as [8, 13, 18]:

$$C(t) = \frac{1}{d}\int_0^d C(x,t)dx \simeq C_0\left[1 - exp\left(-\frac{t}{\tau}\right)\right]. \quad (1)$$

Eq. (1) is a first-order approximation of solution of the second Fick's law of free diffusion for an axial

direction crossing the tissue sample [9, 11, 13, 22 - 23]. In this equation, if the OCA concentration in the immersing solution C_0 is known, the OCA concentration on the tissue can be calculated for any particular time t as an exponential increase over time. Such exponential increase is characterized by the diffusion time τ. If we are performing T_c measurements during the treatment, we can correlate the T_c time dependence with the time dependence of OCA concentration in the tissue. This way, we can rearrange Eq. (1) to fit the T_c time dependence as follows [18]:

$$T_c(\lambda, t) \propto \frac{C(t)}{C_0} = 1 - exp\left(-\frac{t}{\tau}\right). \quad (2)$$

In Eq. (2) we have indicated the wavelength λ to say that the equation is valid for a single wavelength, but similar calculations can be performed for different wavelengths. Such equation is only valid when an effective flux is active between the immersing solution and the tissue sample. It is common in optical clearing treatments that if we perform the treatment for a long period of time, we will certainly observe a saturation regime where no active flux occurs. The time when the saturation regime begins depends on the sample, its geometry and also on the OCA concentration used to perform the treatment. As an example, for treatments of muscle samples with glucose solutions, we have observed that the beginning of the saturation regime occurs at a later period of time if we increase the glucose concentration in the solution from 20% to 40% [7]. This variation is imposed by the free water content in the tissue and the OCA concentration we use. Considering that the active water and OCA fluxes occur before the beginning of the saturation regime, to process the T_c time dependencies, we must consider only the data between the beginning of the treatment and the beginning of the saturation regime. This delimited data is then displaced and normalized to obtain time dependencies that vary between zero and unity. This organized data is fitted with a line described by Eq. (2) and during the fitting procedure, we obtain the characteristic diffusion time, τ for the effective flux in the considered treatment. If we have similar time dependencies for other wavelengths we can perform this fitting procedure for each of the wavelengths and then calculate the mean diffusion time value for that particular treatment. Repeating such method for other treatments made with other OCA concentrations we can represent the mean diffusion time as a function of OCA concentration in the treatment solution. As we have observed from our results for the studies of muscle under treatment with glucose and EG solutions [7, 18], such graph presents the highest diffusion time for a particular OCA concentration. In the case of the muscle, such OCA concentration was 40.5% after we fitted the data points with a spline to evaluate dependence on concentration. Such highest value indicates an optimized OCA diffusion into the tissue, meaning that no water flux occurs in this particular treatment due to the balance between the tissue free water and the water in the immersing solution [18]. If the OCA concentrations in the solutions used to perform the treatments are well selected, the analysis of this final graph provides information about the free water content in the tissue under study. For skeletal muscle, we have obtained a free water content of 0.595 (1 – 0.405), which was a value previously unknown. At this OCA concentration, we have estimated the diffusion time values of glucose and EG in muscle as 302.9 s and 446 s, respectively. These values characterize the RI matching mechanism of optical clearing with glucose and EG [7, 18].

A similar procedure can be performed to estimate the water diffusion time, if we consider a treatment with a highly concentrated solution. For a treatment with 54%-glucose we have obtained a diffusion time for water of 58.4 s and for the treatment with 60%-EG we have obtained a diffusion time of 57.9 s. Although these values are a little different, they indicate that the dehydration mechanism occurs in the muscle within the first minute of treatment.

Once the true diffusion time is obtained for OCA and water, we can use Eq. (3) to calculate the diffusion coefficient [11, 13, 22-23]:

$$D_a = \frac{d^2}{\pi^2 \tau} \quad (3)$$

Since the OCA flux in and water flux out of the tissue sample occur through both sample surfaces, Eq. (3) is appropriate to calculate the diffusion coefficients for these fluids [13]. Using Eq. (3) we have calculated the diffusion coefficients for glucose (5.9×10^{-11} m^2/s), EG (4.6×10^{-11} m^2/s) and water (3.21×10^{-10} m^2/s from the 54%-glucose treatment and 3.09×10^{-10} m^2/s from the 60%-EG treatment) [18]. Although we have obtained two diffusion coefficient values for water, they are very similar.

Finally, the dynamic viscosity of these OCAs in muscle can be calculated using the diffusion coefficients in Stokes-Einstein Eq. [24]:

$$\eta_{OCA} = \frac{k_B T}{6\pi D_{OCA} r_{OCA}}. \quad (4)$$

In Eq. (4), the viscosity of the OCA is calculated using the Boltzmann's constant (k_B=1.3807×10^{-23} J/K), the temperature T of the sample during treatment (in Kelvin), the OCA diffusion coefficient D_{OCA} and the OCA's Stoke's radius r_{OCA}, which should be known for the OCA in study. Performing the calculations with Eq. (4) for glucose and EG, we have obtained the values of 1.0×10^{-2} $kg/(m\cdot s)$ and 1.4×10^{-2} $kg/(m\cdot s)$, respectively [10]. These values indicate that muscle cell membrane limits OCA diffusion into the muscle tissue.

The diffusion of glucose and EG in skeletal muscle is one of many cases of interest and now that the theoretical methodology has been proven experimentally, similar studies need to be performed with other tissues under treatment with different

chemicals. The collection of such information is strongly necessary for different medical and industrial related specialities. In particular the knowledge of the diffusion properties of creams and ointments in skin is very significant for cosmetics and dermatology [25]. On the other hand, the diffusion properties of low temperature preservatives are of great interest for organ preservation industry and also for food preservation in long time periods [3, 26-28]. In the particular case of tissue optical clearing, there are many tissues and many OCAs that need to be studied. A particular interesting application that can be developed is based on the differentiation between the diffusion properties of a particular OCA in healthy and pathological tissue. If this method provides significant results it will be possible to develop an optical and non-invasive diagnostic methodology for tumour detection.

With such many fields that need the collection of the diffusion and viscosity properties of chemicals in biological tissues, it is highly recommended that a software application should be developed to perform the necessary calculations from the experimental measurements to obtain the diffusion time, diffusion coefficient and viscosity of chemicals and water. We have recently developed such application as an integrated solution that performs all necessary calculations in a sequential and optimized manner to estimate the desired parameters. The application was validated with the experimental data that we have published for muscle treatments with glucose solutions and results are in good agreement [7]. The following sections describe the development and validation of the application.

2 Materials and methods

Since our objective was to develop a software application, we have selected MATLAB™ as our tool and programming language. The choice of MATLAB was made since it is a dedicated software to work with mathematical and physical problems and offers many possibilities in data fitting and figure generating. The main application and all subroutines were developed in MATLAB language. The final application contains many routines that are used to perform the various steps, such as load and save experimental or calculated data. Each of the steps in the data processing or calculation procedures is also made by a particular routine. The sequential steps to be executed by the application are made in an ordered manner and they will be described sequentially in section 3.

During the application development, the experimental data that we have obtained from the muscle treatments with glucose solutions was used to make corrections to the various routines. After finalizing the application, the same experimental data was used to perform the calculations of the diffusion and viscosity properties of glucose and water. Comparing those results with the ones that we have previously obtained [10], we have validated the application.

3 Results and discussion

At the end of each experimental study, the only data available is the T_c spectra and thickness time dependence measured along the various treatments with different OCA concentration [7, 10, 18]. To follow the data processing and calculation procedures described in section 1, a routine was created to comply with each step and a main application program was developed to integrate all routines in sequential form. The main program is associated with a main window that is used to provide a user interface, present the various results in sequence to the user and allow him to adjust certain procedures manually, when necessary.

When the main program is initiated by the user, the application opens the main window. This window contains a menu at the top that allows loading or saving the experimental and calculated data, an "Options" button that allows configuring the aspect of the main window and a "Help" button that shows some guidelines to assist the user in the various stages of data processing or calculation.

To calculate data from a study, the first step is to upload the T_c data from all treatments performed. To do this, the user selects from the "Load" menu the option "Load (New)". A browser window is opened and the user selects the main folder that contains the various sub-folders correspondent to each particular treatment with T_c measurements (one for each OCA concentration). From the "Load" menu there is another option to load a saved experiment. Such option can be used if the user cannot finish the calculations in the same day. The upload of all data from all treatments is made at once and the spectra are presented on the right as we can see from Fig. 1.

On the upper right of the main window, we have several sub-windows that present the entire collection of spectra measured in each particular treatment. Such graphs are configured to present spectra between 170 and 1100 nm. Although these graphs present spectra from 200 to 1050 nm, we have neglected spectral data below 400 nm, since it corresponds to a strong inclusion of fluorescence. As we can see from Fig. 1, the spectra presented corresponds to the treatment with 20%-glucose, as indicated by highlighted label (20) on top of the graph. The other labels on the right are accessible by clicking over them and the spectra from each treatment can be seen.

Below the window with the spectra there is a matrix containing the spectral values for each time of treatment, so the user can check a particular value if necessary. If we select a different treatment above the spectra window, the data in the matrix will change automatically.

On the upper left there is an application log window that presents the various tasks that have been executed or eventual errors that might occur. Below this window there is an input window to select the wavelength bandwidth and the number of wavelengths to calculate the T_c time dependencies. As indicated in Fig. 1, our selection was 600 nm for the first wavelength to be

considered, 800 nm for the last and 11 for the number of wavelengths within the selected band. These choices will generate T_c time dependencies for wavelengths at each 20 nm from 600 to 800 nm. Once these values are appropriately selected, the user clicks the "Generate"

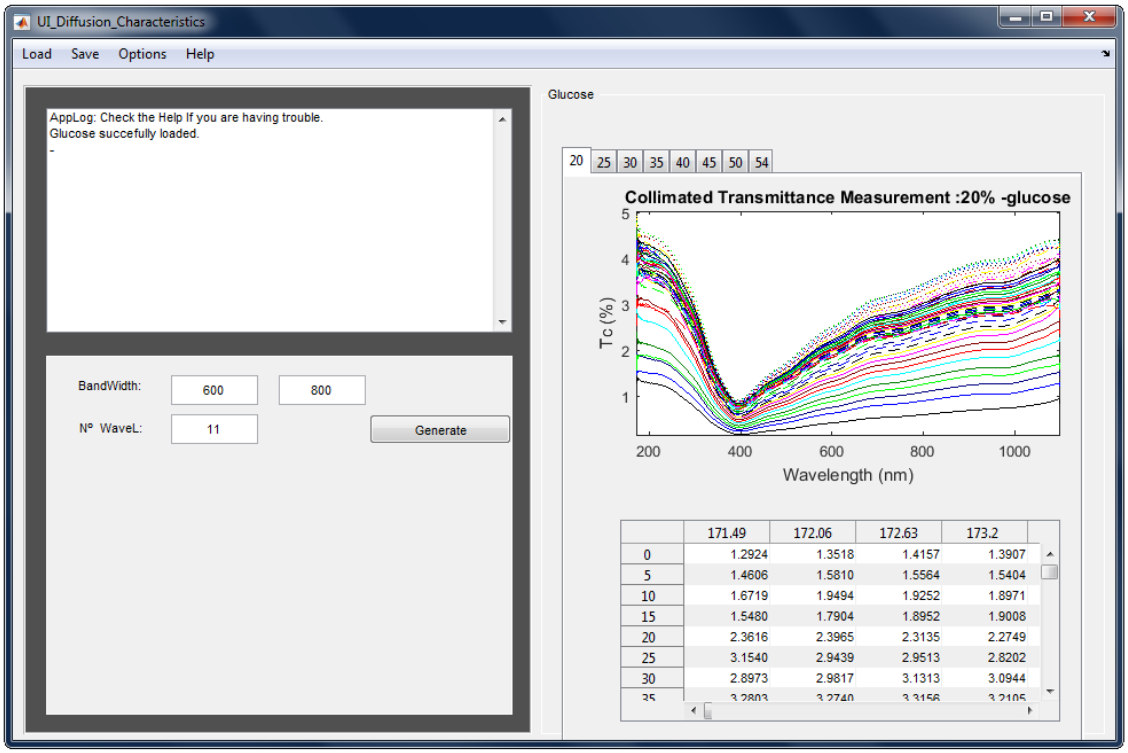


Fig. 1 Main window after uploading T_c data from all glucose treatments.

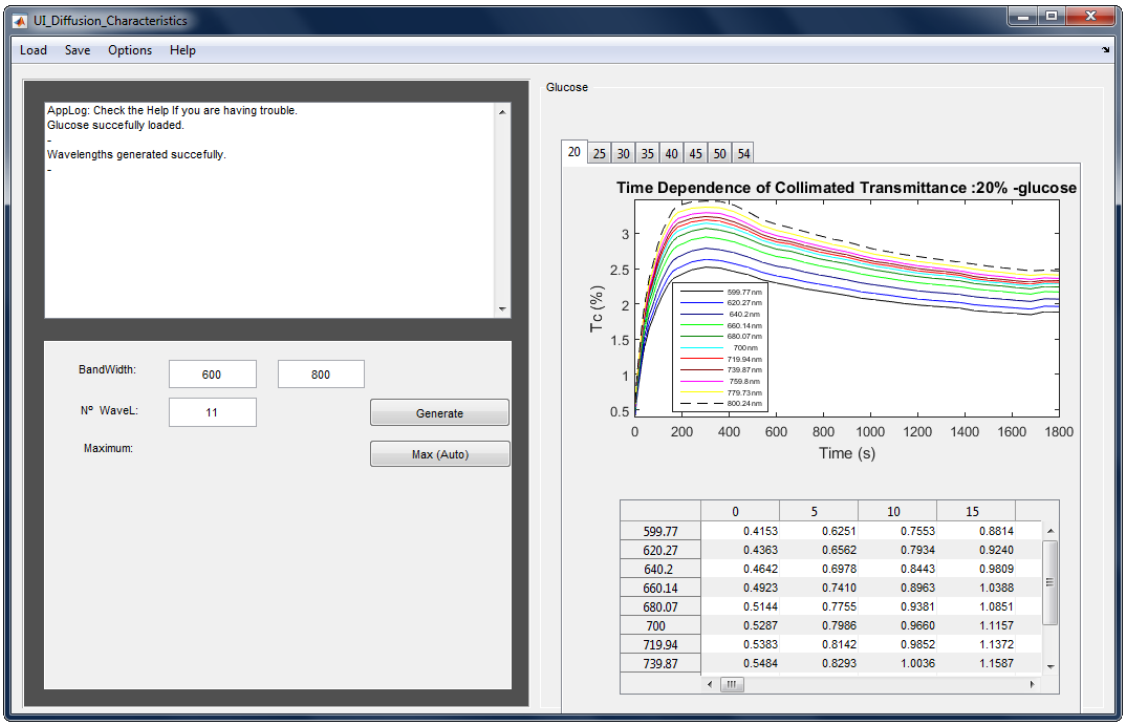


Fig. 2 Main window after selecting the wavelengths to calculate T_c time dependencies.

button to proceed. The previous data and graphs are replaced as can be seen in Fig. 2.

On the left of the main window a new button was added just below the "Generate" button. This new button is the "Max(Auto)" button, which allows selecting the beginning of the saturation regime in the T_c time dependencies represented for each treatment on the upper right graphs. Once again the graphs represented on the upper right can be exchanged between treatments by selecting the desired label.

The data matrix presented on the lower right contains now the T_c time dependencies for each wavelength and corresponds to the graph presented just above. If the graph is changed, the data in the matrix also changes. The next step consists on finding the beginning of the saturation regime for the treatment. To do this, the user selects the "Max(Auto)" button and some points appear in the graph on the right as can be seen in Fig. 3.

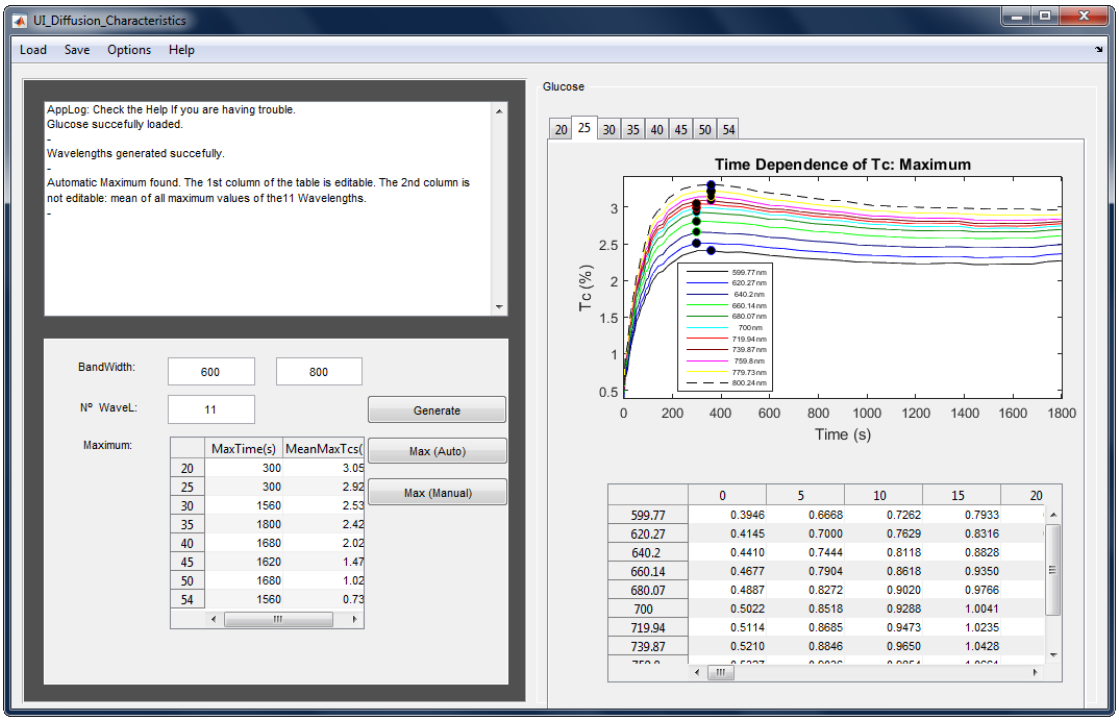


Fig. 3 Main window after automatic identification of the beginning of the saturation regime.

The graph presented in Fig. 3 corresponds to the treatment with 25%-glucose to show that the automatic selection was not done accurately for this particular case. The dots presented on the various curves of the graph are seen at two different times of treatment: 300 and 360s in the case presented in Fig. 3. To correct this, the user has now available on the lower left window a new button ("Max(Manual)") that allows for making a manual selection of the beginning of the saturation regime. With the automatic selection a new matrix is presented in the lower left window. In the first column of this matrix is presented for each treatment the time that corresponds to the greater number of maximal T_c values. The second column of the matrix contains the mean maximum T_c value observed for all dots on the graph. To correct the selection of the beginning of saturation regime, the user must click on the "Max(Manual)" button. When the user selects this button the first column on the lower left matrix becomes editable. Then the user should insert the values that he sees adequate for each treatment and click the "Max(Manual)" button again. At this point all graphs show the point markers at the time instant that the user selected, as we can see in Fig. 4 for the previous case of treatment with 25%-glucose.

Now we can see in Fig. 4 that all point markers are located at 360s for the 25%-glucose treatment. After the manual correction was made, a new button appears below the "Max(Manual)" button. This new button is called "Draw [0-max]" and it shows the treatment graphs on the right delimited between the beginning of treatment and the beginning of the saturation regime. When these new graphs are generated, each dataset (for each wavelength) was displaced vertically to have T_c=0 at t=0. Figure 5 presents the case of 20%-glucose treatment with graph contained in the first 300 s.

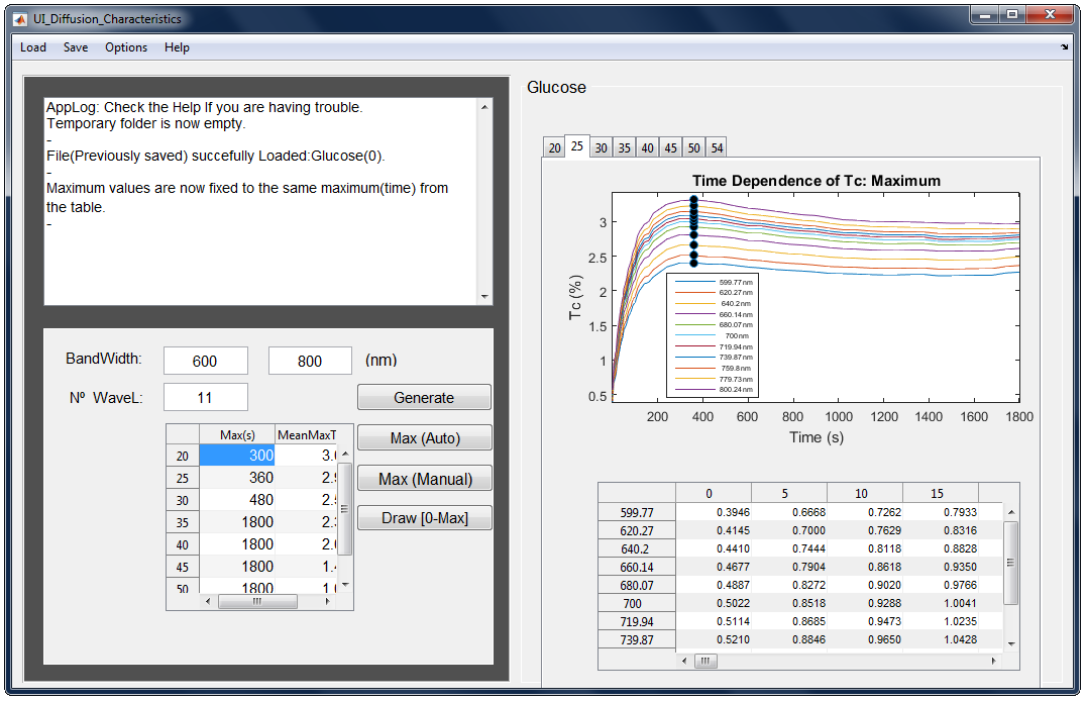


Fig. 4 Main window after manual correction of the beginning of the saturation regime.

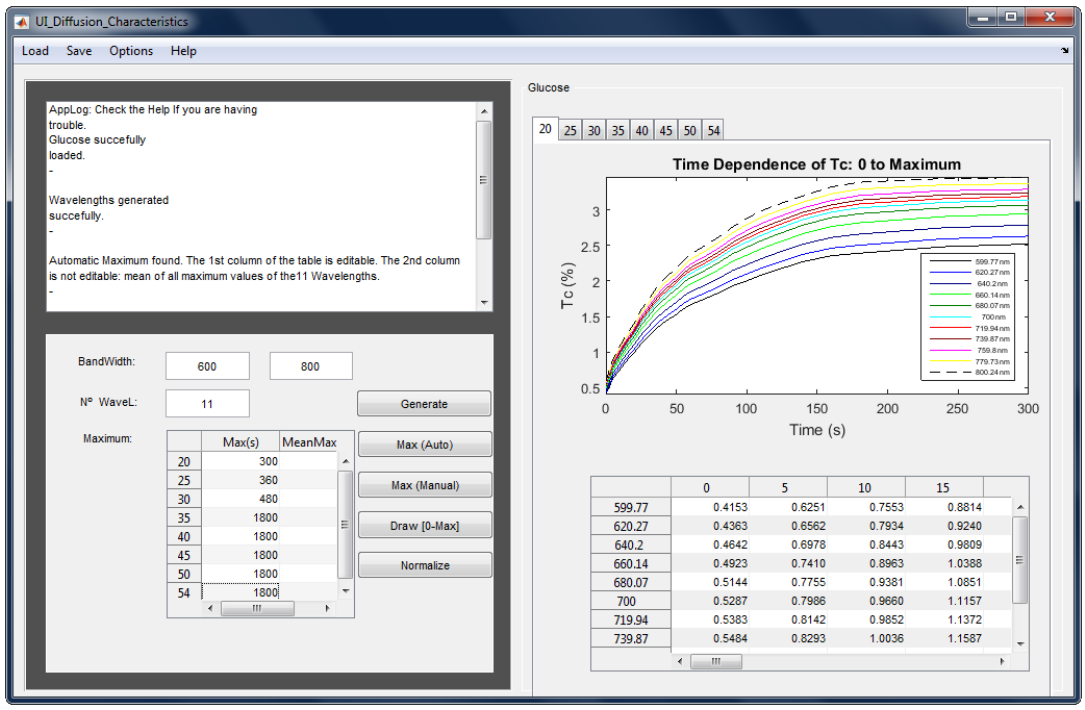


Fig. 5 Main window after T_c time dependency delimited by the beginning of the saturation regime was displaced vertically.

Once again the matrix on the lower right of the main window contains the data values correspondent to the graph above and it is updated each time the user selects one of the treatments from the labels above graph. In Fig. 5 we can now see a new button called "Normalize". This button performs the next data processing, by normalizing the delimited T_c time dependencies of each treatment to each highest value. This normalization procedure takes some time to be done, since normalization is made for each curve that corresponds to a single wavelength within each of the various treatments. At the end new graphs are presented on the right of the main window with the datasets normalized.

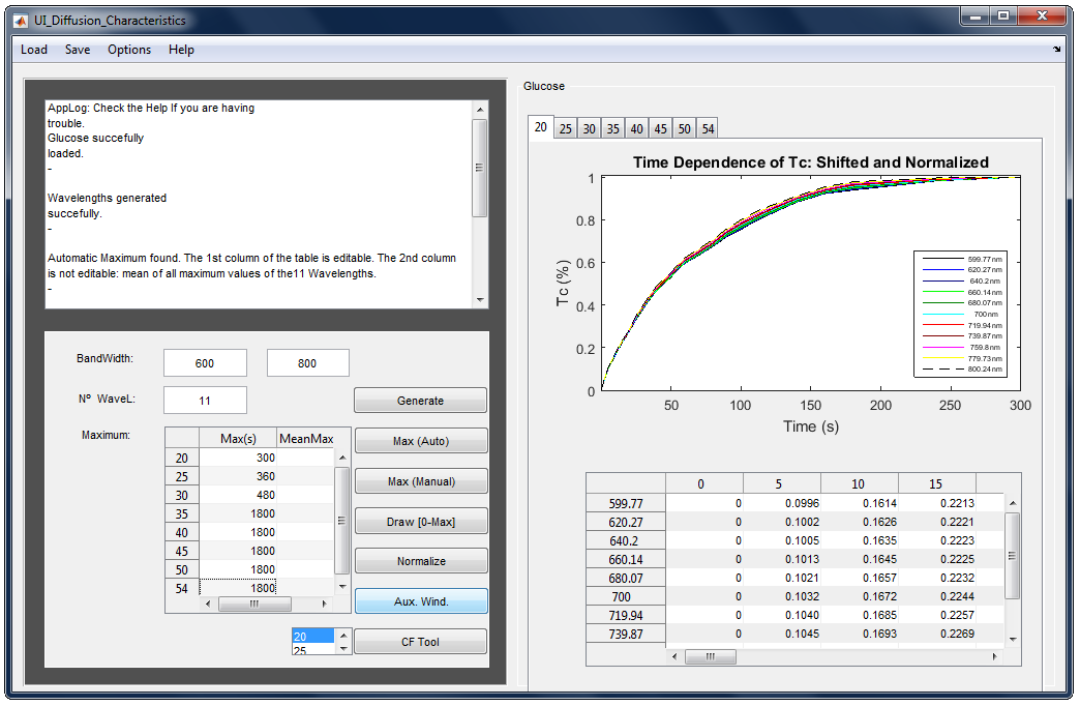


Fig. 6 Main window after performing data normalization to the value measured at the beginning of the saturation regime.

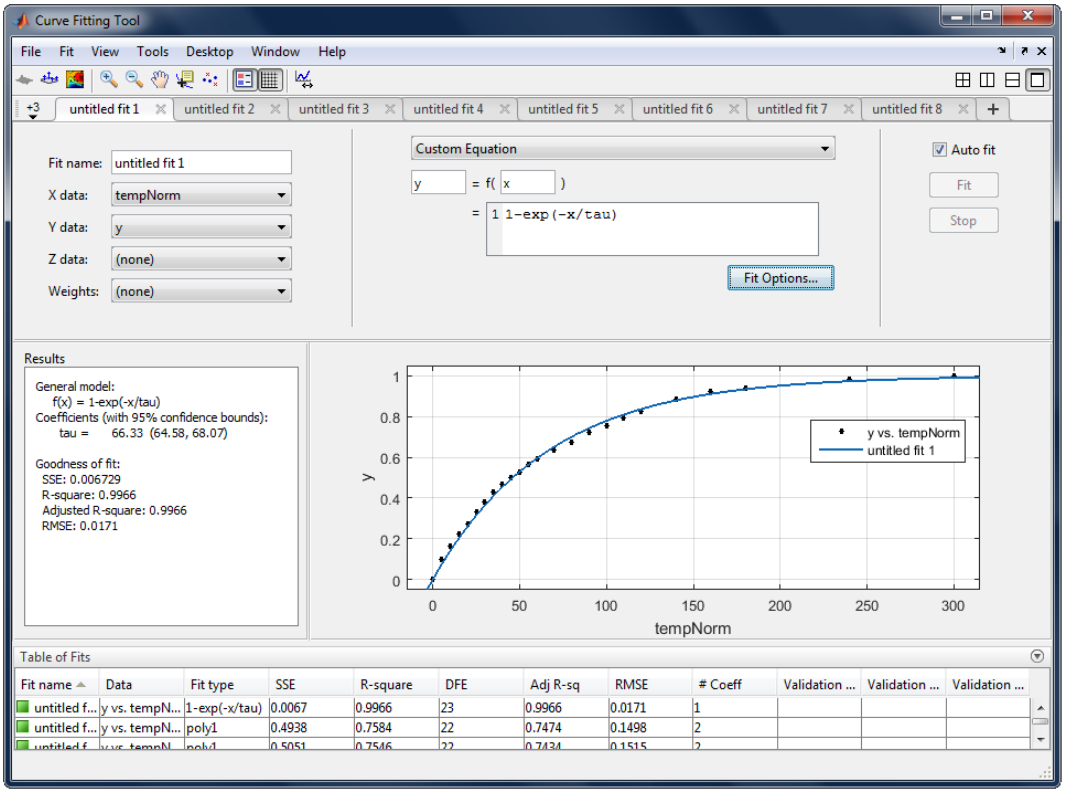


Fig. 7 Curve Fitting Tool window with all the data for the treatment with 20%-glucose.

After performing data normalization, two new buttons appear at the lower left section of the main window. These buttons will be used for the data fitting. The first new button is the "Aux. Wind.", which generates a new auxiliary window for the fittings and the second button is the "CF Tool", which corresponds to a MATLAB tool – Curve Fitting Tool and it generates also a new window with all the datasets for a particular treatment. In Fig. 6 we see that next to the CF Tool there is a scroll-dawn window with the number 20 in blue. This means that if the user clicks the "CF Tool" button, the data that will be uploaded to the new CF Tool window for the fitting procedure will be the data for the treatment with 20%-glucose. If the user wishes to select another treatment, it just needs to select it from the scroll-dawn window. Considering the 20%-glucose treatment, Fig. 7 presents the CF Tool window.

As we can see from Fig. 7 there are many tabs at the top with the labels "untitled fit 1", "untitled fit 2" and so on. Each of these tabs contains the dataset correspondent to each wavelength so the user can make the data fit for each one independently. In Fig. 7 the first tab is selected with the fitting line already applied to the dataset correspondent to 600 nm. Since CF Tool is a specific tool of MATLAB, we could not find a way so far to name the labels according to the wavelength, but this is considered for next improvements. There are many fitting options in the window. For instance, above the graph we have the equation fitting options where the user can select the most appropriate from a wide set of equations. In our case, the equation to be used in the fitting is according to Eq. (2). By selecting a custom equation and introducing Eq. (2) manually, the user can then select the best fitting options for this type of line by clicking the "Fit Options…" button. The fitting is optimized when the R-square value on the "Results" window is maximized. In the case represented in Fig. 7, the R-square value is 0.9699 and the τ value obtained in this fitting is 66.33s.
The R-square value optimization is made through a set of options related to fitting methods. Within the Least-square fitting method, we can for instance select between the algorithms of "Trust-Region" or "Levenberg-Marquardt". The objective is to obtain the highest R-square value to ensure the best data fit. A fitting must be performed to all datasets correspondent to each of the 11 wavelengths (one in each tab). The user must do these fittings manually and sequentially. Once all fittings are made and optimized, the correspondent τ values can be introduced manually in the matrix of the auxiliary window:

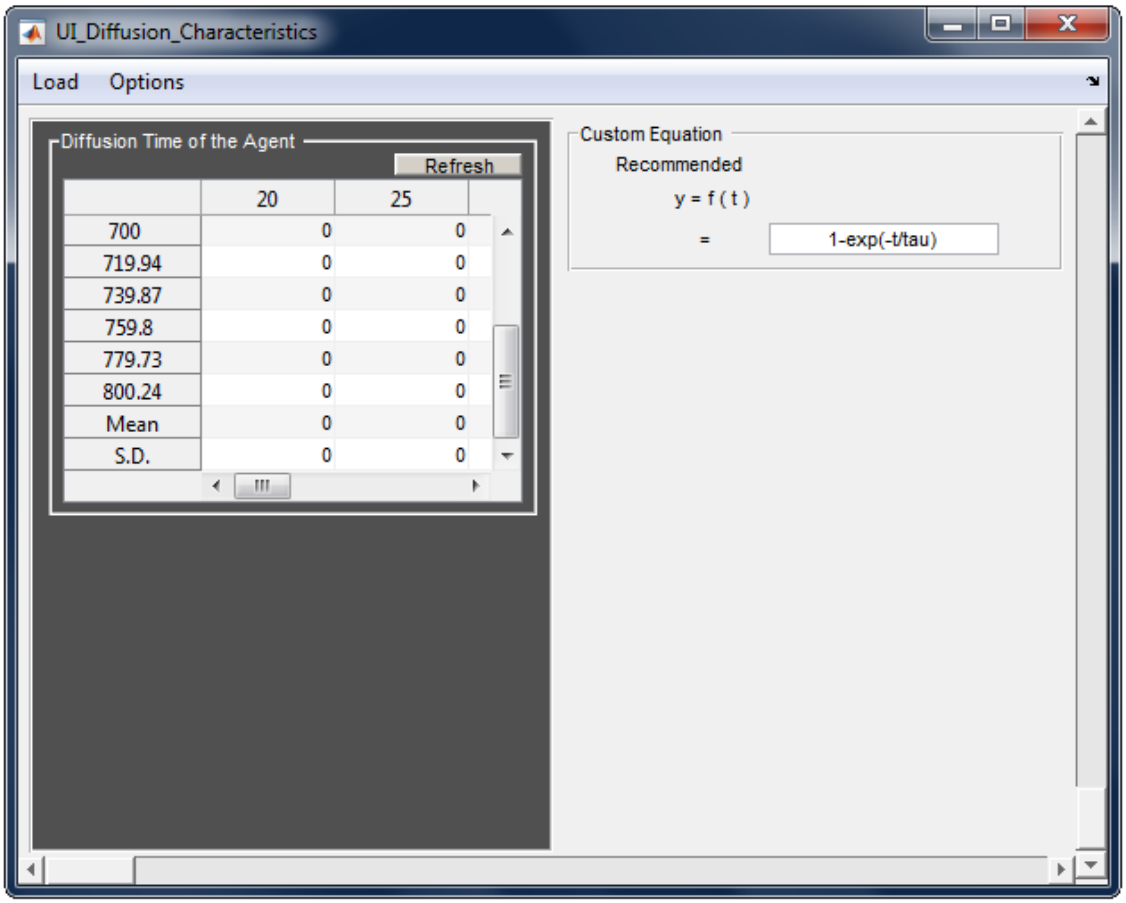


Fig. 8 Auxiliary window to introduce the diffusion time values for each treatment.

The auxiliary window represented in Fig. 8 contains the fitting equation on the right side, so that the user can copy it to the CF Tool window to save time. Both windows must be open at the same time to copy data manually from one to the other. The user must introduce the values on the matrix of the auxiliary window manually, since there is no direct way to copy those values from the "CF Tool" window.

Once the matrix in the auxiliary window is complete with all the diffusion time values from all wavelengths and treatments, the user clicks on the "Refresh" button above the matrix and the mean and standard deviation for all treatments are calculated and presented in the two lower rows of the table. At the same time a graph appears at the lower right of the auxiliary window containing the mean diffusion time values as a function of OCA concentration in solution. This graph shows also error bars that correspond to the standard deviation values on the matrix to show how disperse are the diffusion times in each treatment.

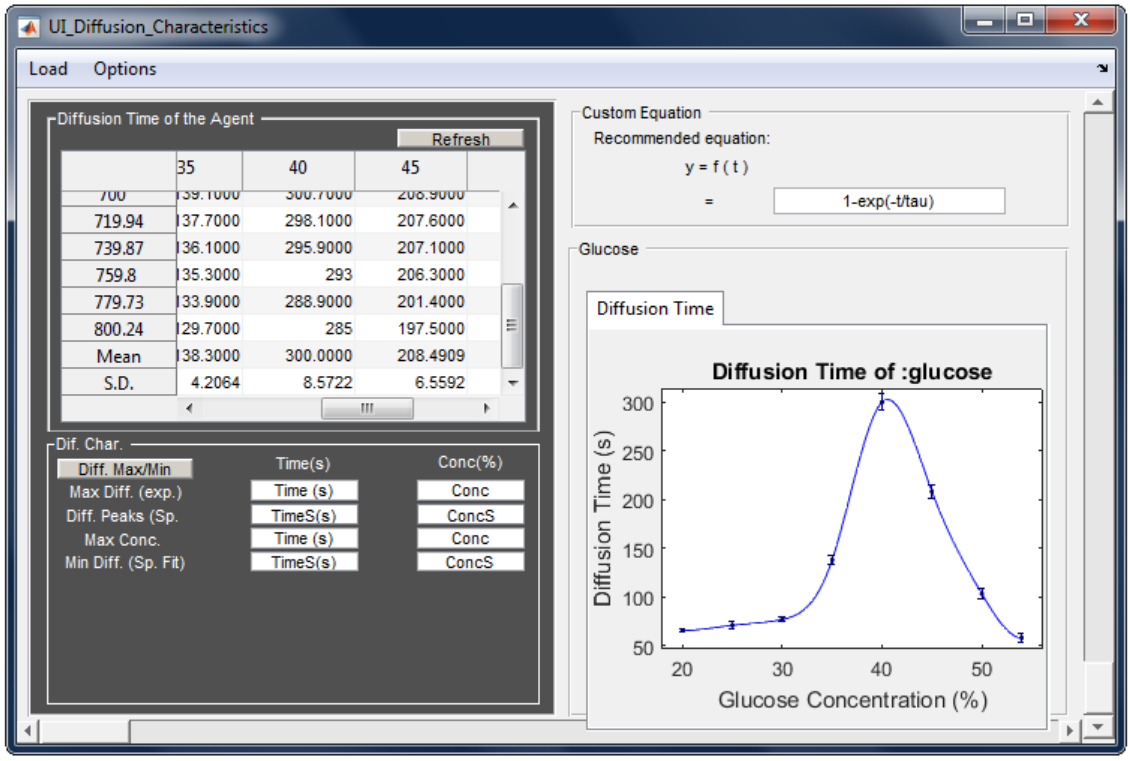


Fig. 9 Auxiliary window after filling the τ matrix.

As we can see from Fig. 9, some fields related to the OCA and water diffusion characteristics also appeared at the lower left. The first column corresponds to the diffusion time and the second to the OCA concentration in solution where those diffusion time values are observed. Once the user clicks on the "Diff. Max/Min." button, the values in these fields are automatically filled and new fields appear just below, as presented in Fig. 10.

In the first column of the diffusion characteristics, we see from top to bottom: the maximum experimental mean diffusion time (300s), the estimated absolute maximum mean diffusion time (302.674s), the smallest experimental mean diffusion time (58.4s) and the smallest estimated mean diffusion time (58.4s). The second column contains the OCA concentration values that correspond to the diffusion time values in the first column. As an example, the estimated maximum diffusion time of 302.674s would occur for an OCA concentration of 40.6%. The values in the two columns are also presented on the right side graph with different symbols and colours.

As the diffusion characteristic values are presented, four new fields are presented just below. These fields are the sample thickness (left column) and the diffusion time (right column) to calculate the diffusion coefficients for OCA and water. The user must copy the diffusion time values from OCA (302.674s) and water (58.4s) into the lower second column. These values are much approximated to the ones that we have previously estimated for glucose. In our previous estimations [7, 18], we have estimated a diffusion time of 302.9s for glucose from a treatment with 40.5%-glucose and the exact diffusion time of 58.4s for water from a treatment with 54%-glucose.

Once the first of these diffusion time values is introduced, new other fields and buttons appear, as we can see from Fig. 11.

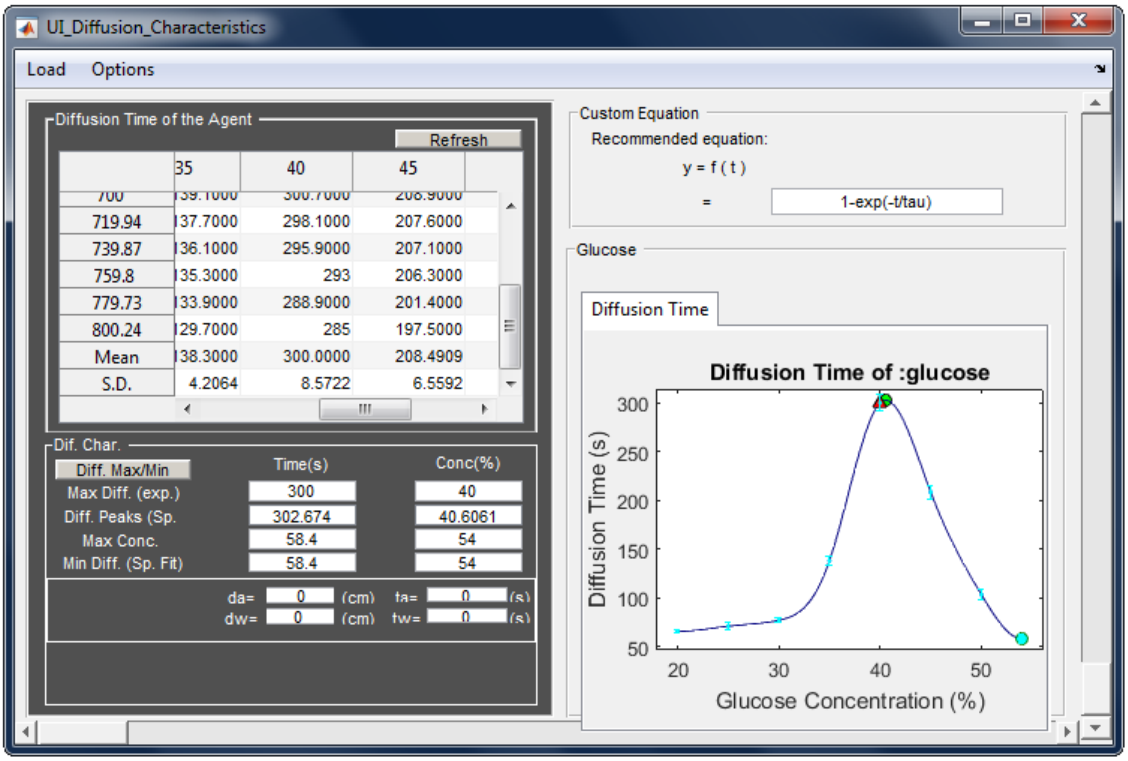


Fig. 10 Auxiliary window with automatically detected data for the diffusion time values.

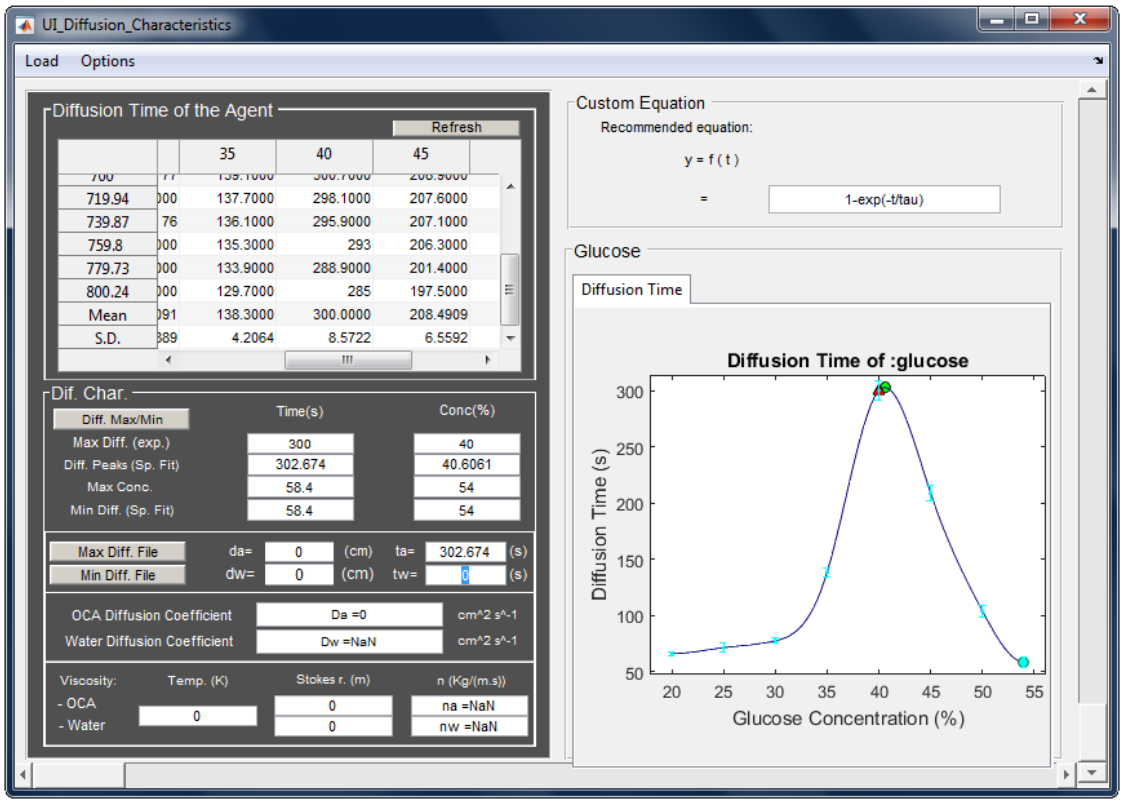


Fig. 11 Auxiliary window ready to calculate the diffusion coefficient and viscosity values.

Figure 11 shows that two new buttons became available on the left side of the thickness fields. If the user has the correct values for sample thickness to introduce, he can do it manually. If not, the new buttons are used to upload the experimental thickness time dependence files that correspond to the OCA

concentrations that produce the diffusion coefficients for OCA and water. For the case of water diffusion time, the OCA concentration was 54%, so we can upload the thickness time dependence of the sample for this treatment, by clicking the "Min Diff. File" button. For the case of OCA diffusion time, the application estimated that an OCA concentration of 40.6% is the ideal one. This value is almost the same as the ideal glucose concentration obtained in our previous estimations (40.5%) [18]. Since we do not have data for such a treatment, we can upload the thickness time dependence for the treatment with 40%-glucose by clicking the "Max. Diff File" button. By using this data, we do not introduce a significant error.

At the bottom, we already see from Fig. 11 the fields to present the diffusion coefficients and viscosity values of OCA and water. After introducing the diffusion time values for OCA and water, the user uploads the thickness time dependence files. Once they are uploaded, the application immediately creates two new graph tabs on the right. These new graphs contain the thickness time dependencies that were uploaded. The application also creates in each of the graphs a point with the thickness value that corresponds to the diffusion coefficient presented on the left. If the diffusion time value does not correspond exactly to a particular measurement, the point is interpolated, as we can see from graphs in Figs. 12 and 13.

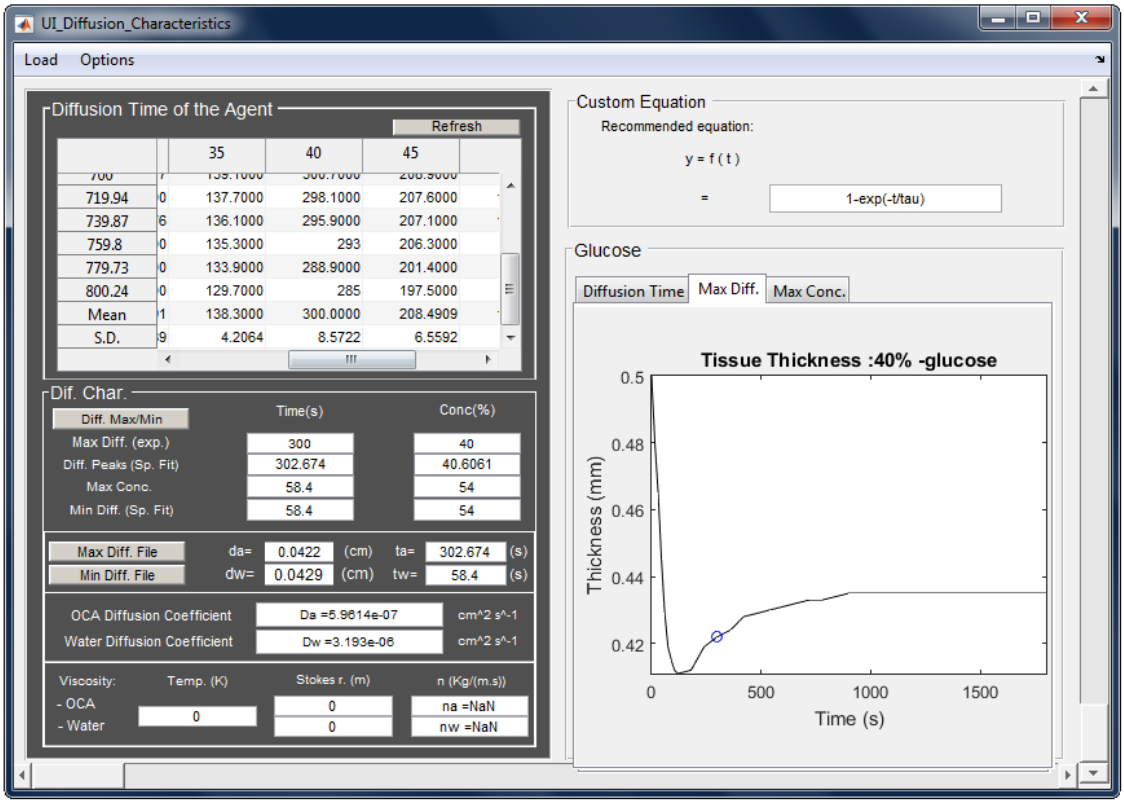


Fig. 12 Thickness time dependence graph for the treatment with 40%-glucose.

For the case presented in Fig. 12, a blue dot was automatically placed at the time of 302.674s and the correspondent thickness value of 0.0422 cm is placed in the field on the left side of the auxiliary window. The same happens to determine sample thickness to calculate water diffusion coefficient, as presented in Fig. 13.

In this case, a thickness of 0.0429 cm corresponds to the 58.4 s in the treatment with 54%-glucose.

In addition to the automatic detection of sample thickness, the diffusion coefficients are also automatically calculated and presented in the corresponding fields.

As we can see from Figs. 12 and 13, the calculated diffusion coefficients for glucose and water are respectively $5.9614\times10^{-7}\,(cm^2/s)$ and $3.193\times10^{-6}\,(cm^2/s)$. For the diffusion coefficient of glucose in muscle, our previous calculations have estimated the value of $5.9\times10^{-7}\,(cm^2/s)$ [10]. Our previous estimation for the water diffusion coefficient was $(3.21\times10^{-6}\,(cm^2/s))$ [10]. By comparing between these values, we see that the application generates very similar values. The differences that were observed have to do with the possibly different fitting algorithms and options used in both estimations to determine the various τ values.

The final calculation is the viscosity of glucose and water. To perform this calculation, the user must introduce the temperature (in K) observed during the studies and Stokes radius in the auxiliary window. This

value must be in meters (m), as indicated on Fig. 13, for example. For the temperature value we have introduced 293K (20 ºC), as in our previous estimations. Since we do not know the Stokes radius for water molecules, we have only introduced the value for glucose. This value of $0.365\times10^{-9}\,m$ is the same used in our previous estimations and was obtained from literature [29]. Fig. 14 shows the auxiliary window with all the data calculated.

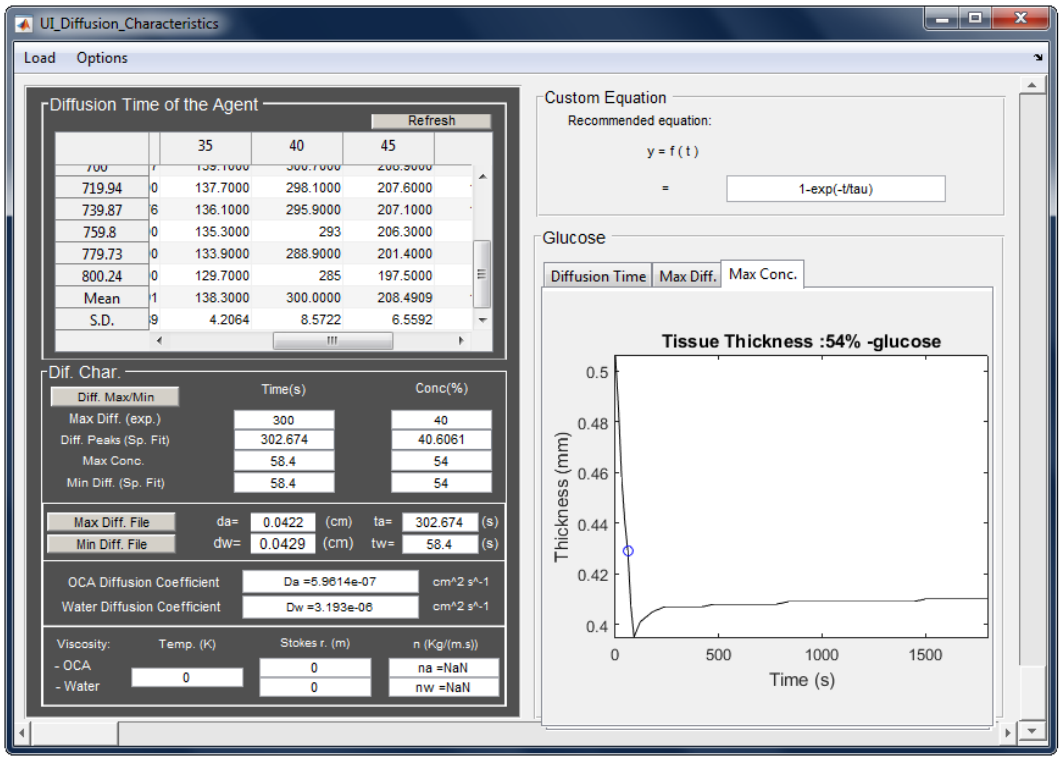


Fig. 13 Thickness time dependence graph for the treatment with 54%-glucose. Blue dot signals the thickness at 58.4s.

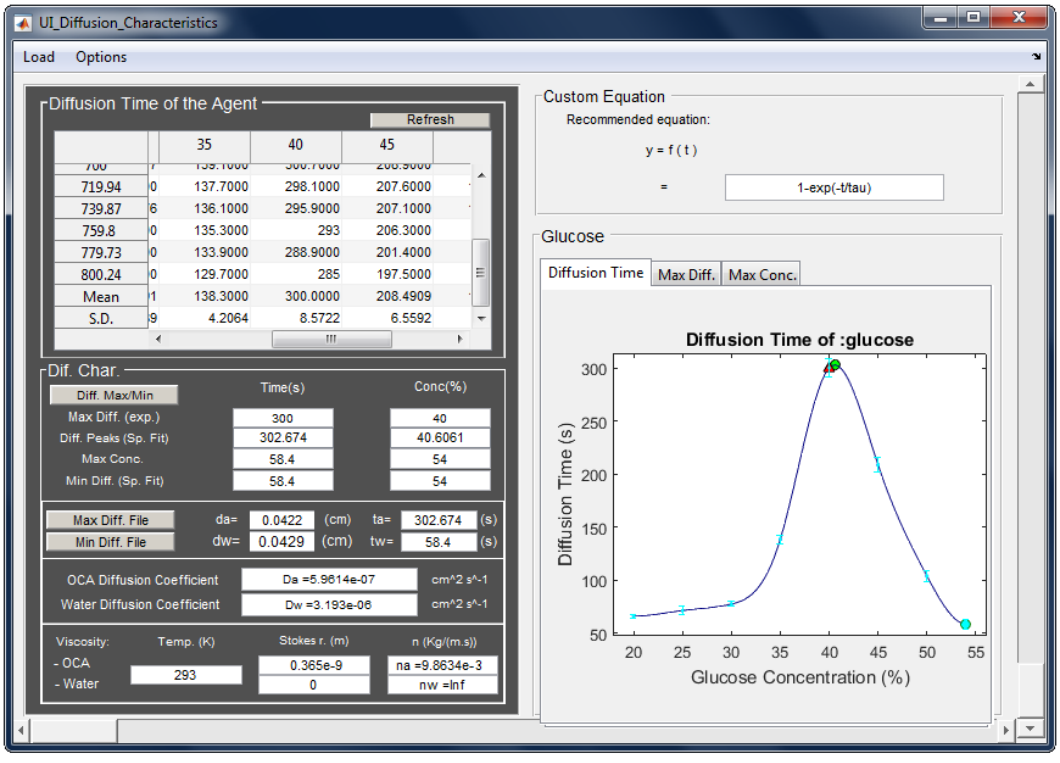


Fig. 14: Complete auxiliary window with all estimated and calculated diffusion and viscosity data.

Comparing the calculated viscosity for glucose (9.863×10^{-3} $(kg/(m\cdot s))$) with the one from our previous estimations (1.0×10^{-2} $(kg/(m\cdot s))$) [10], we see that they are also much approximated.

Although there have been observed some limitations in the application, it works in an integrated manner to perform the necessary calculations from the raw T_c and thickness measurements. There are some improvements that we plan to do to this application to turn it even better. We will discuss these matters in the following section.

4 Conclusions and future perspective

After finalizing, testing and validating the application we see that it is a very useful tool to help in the calculation of the diffusion properties of chemicals and water in biological tissues. It is an organized and focused tool that uses the theoretical background described in literature [13] for fast estimation of the characteristic diffusion and viscosity properties of optical clearing agents and water in tissues, based on collimated transmittance T_c and thickness measurements of a tissue sample. Such properties are particular for any agent-tissue combination and allow the characterization of the optical clearing mechanisms involved in the treatment – tissue dehydration and RI matching. Once the software has been developed, it can now be used for several and diversified applications. For instance, future studies can now be performed to calculate the diffusion properties of skin lotions and topically delivered medications. Another potential application may provide a diagnosis method for cancer detection. Healthy and pathological tissues have different water contents and consequently will originate different diffusion properties or viscosities for agents used in a monitoring study. By comparing between the different calculated properties, it might be possible to develop a non-invasive optical diagnosis method for early cancer detection. Future studies are necessary and this software is a significant asset for that research.

This application can read any set of files, provided they are named in a pre-established way and placed inside folders that correspond to particular treatments. Although the case presented here corresponds to treatments with glucose at the specified concentrations in solution, other concentrations are accepted by the application. It also can export graphical and numerical data in different formats like excel, pdf or MATLAB figures. The figures were not presented in this paper, but they can be generated and formatted according to the wishes of the user. At any stage of the data processing or calculation, a report can be generated in pdf or latex formats.

There are also some things we wish to improve in this application. As mentioned above, one thing to be tried in the next improvements is to correct the graphical labels in the CF Tool window to indicate which wavelength corresponds to each dataset to be fitted. On the other hand, the application saves temporary files with the data from the various steps of processing or calculation. One other improvement is to provide these file savings in a more user friendly manner.

Considering the benefit of having such application, we now plan to use it in our future research. As we have indicated in the introduction, we plan to perform several and different diffusion studies of various chemicals in various animal and human tissues. We will use this application to facilitate our data processing and calculation to obtain the diffusion properties in a more easier and fast way.

Statistical analysis of the parameters of the optic disk image

Valery Bakutkin[1], Vadim Gorelov[2], Yuriy Zayko[2*]

[1] Saratov Research Institute of Rural Hygiene, 1A Zarechnaya str., Saratov 410022, Russia

[2] Stolypin Volga Region Institute of Administration, Russian Presidential Academy of National Economy and Public Administration, 23/25 Sobornaya str., Saratov 410031, Russia

[*] **e-mail:** yuriyz@mail.ru

Abstract. In recent time much attention is payed to the computer analysis of the optic disc (OD) images, aimed at extracting the objective statistical characteristics of the OD image. In the present paper we describe a computer program that allows the determination of the mean colour indices, their variance, etc., for different regions of the OD. The total colour space in the RGB model is divided into subdomains in correspondence with the values of the mask that determines the subdomain boundaries. A simple method of determining the domain of the OD physiological excavation by the value of the variability coefficient is proposed. © 2016 Samara State Aerospace University (SSAU).

Keywords: eye diseases, optical disc, computer program.

Paper #2730 received 2015.11.15; revised manuscript received 2015.12.05; accepted for publication 2015.12.30; published online 2016.02.16.

References

1. V. V .Bakutkin, Y. N. Zayko, A. S. Lepesko, and A. N. Skidanov, "Development of a system for classification and diagnostics of ophthalmologic diseases based on artificial neuron networks," Proc. of Saratov University, Ser. Physics 8(1), 36-41 (2008).
2. V. V. Bakutkin, V. V. Gorelov, and Y. N. Zayko, "Computer analysis of the optic disk image," 19th School for Junior Scientists and Students on Optics, Laser Physics & Biophotonics, Saratov, Russia, 21-25 September 2015.
3. Y. N. Zayko, "Physics of Color Formation," Journal of Applied Physical Science International 2(4), 137-144 (2015).
4. G. Wyszecki, and W. Stiles, Color Science. Concepts and Methods, Quantitative Data and Formulas, 1st ed., Willey (1967). ISBN: 978-0471969204.
5. V. V. Gorelov, "Development of methods for analyzing medical data (by the example of visual nerve images)," Diploma project / Supervised by Zayko Yu. N., Stolypin Volga Region Institute of Administration, Saratov (2010).
6. B. Y. Kuritsky, Search for Optimal Solutions Using Excel 7.0 in Examples, BHV (1997). ISBN: 5-7791-0037-3.
7. V. A. Machehin, "Modern techniques in the analysis of the disc of the optic nerve," Russian Medical Journal. Clinical ophthalmology. Glaucoma 1, 14-18 (2011).
8. V. V. Bakutkin, Y. A. Dubinina, and I. O. Kolbenev, "Method of diagnostics of the visual nerve atrophy," The patent of the Russian Federation №2282390 from 27.08.2006, Patent application №20005102366, priority of 31.01.2005.
9. Y. A. Dubinina, "Complex system of assessing the optic disc condition in patients with primary open-angle glaucoma," Abstract of the Candidate of Medical Sciences thesis, Samara State Medical University, Samara (2011).
10. Y. A. Dubinina, V. V. Bakutkin, and I. O. Kolbenev, "Color index in the diagnostics of partial atrophy of optic nerve of various aetiology," Theses of Reports, VIII Congress of Ophthalmologists of Russia, Moscow, Russia, 1-4 June 2005, 692-693 (2005).
11. V. V. Bakutkin, I. V. Bakutkin, Y. N. Zayko, and V. F. Spirin, "Computer image analysis of the optic nerve in clinical practice," Proc. of the Orenburg State University 4(153), 27-29 (2013).

1 Introduction

The present work was carried out within the framework of the Agreement about the scientific and technical collaboration between the Stolypin Volga Region Institute of Administration and the Research Institute of Rural Hygiene (Saratov) and was aimed at the development of a physical approach to the colourimetric analysis of the human eye images. The beginning of the development of the physical theory of colour perception was started from 2006 and is related to the use of artificial neuron networks in the diagnostics of eye diseases [1]. Later efforts were mainly aimed at the use of computer analysis of the optic disc (OD) images in order to get objective quantitative characteristics of glaucoma [2]. An alternative branch of studies was related to the development of statistical theory of colour formation and perception [3] basing on the concept of colour temperature (CT) of the emitting object. All existing methods of the CT determination are associated with using the concept of the "standard colourimetric observer" [4], which introduces uncertainty into the colourimetric measurements. The method of CT measurement free of this drawback is described in [3].

Another source of uncertainty in colourimetric measurements implemented using the computer images is due to the properties of standard monitors. These measurements require corrections that should account for the specific features mentioned above. However, if the images are obtained and stored in the computer memory in a certain format, the correction is not necessary, since all computer programs "see" the same file that contains all information about the colour composition of each pixel.

This approach became possible, because in the recent time many programs operating with the computer images appeared, particularly in medicine. All problems related to the correct colour reproduction are solved at the stage of the image preparation before recording the file.

In this paper we present the results of the OD images, obtained using the special instrument, the "OPTON" fundus-camera. It is a combination of a microscope and a photo camera. The scanning method is known as the eye fundus photorecording. The experimental material offered by the Research Institute of Rural Hygiene (Saratov) was obtained in patients without expressed signs of glaucoma. The study was aimed at clarifying the boundary between the norm and the glaucoma pathology. The method of study was the statistical analysis of the OD. The object of study were the OD images obtained in a number of patients belonging to different age groups and having no expressed signs of glaucoma.

2 Measurement technique

To achieve the formulated goal, we developed a computer program that determined the mean colour characteristics and mean-square variance for different regions of OD. Figure 1 shows the program interface.



Fig. 1 The program interface. The top right window is the initial image; the small top left windows display the OD area and the result of its processing with the program. Below them the windows for the input of the colour mask values are seen. The rest elements are used for the interface between the program and the environment.

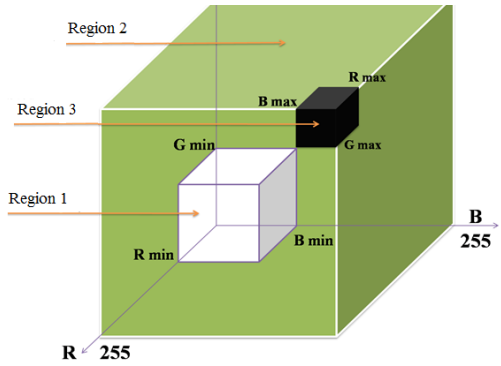


Fig. 2 Division of the RGB colour space into three subdomains.

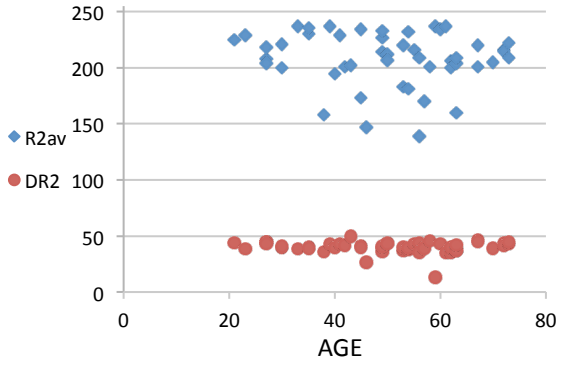


Fig. 3 Dependence of R2av and DR2 (ordinate) upon the age of the patients (abscissa).

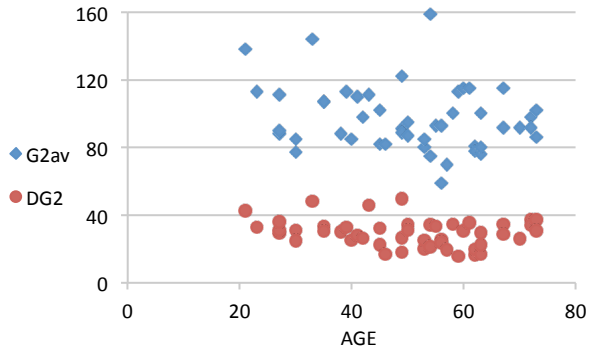


Fig. 4 Dependence of G2av and DG2 (ordinate) upon the age of the patients (abscissa).

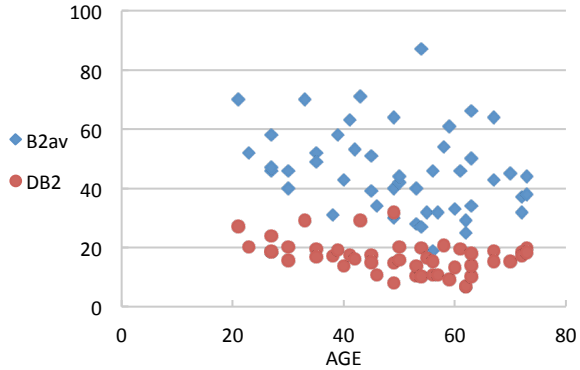


Fig. 5 Dependence of B2av and DB2 (ordinate) upon the age of the patients (abscissa).

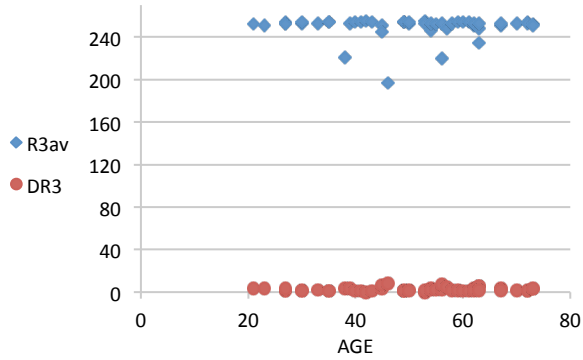


Fig. 6 Dependence of R3av and DR3 (ordinate) upon the age of the patients (abscissa).

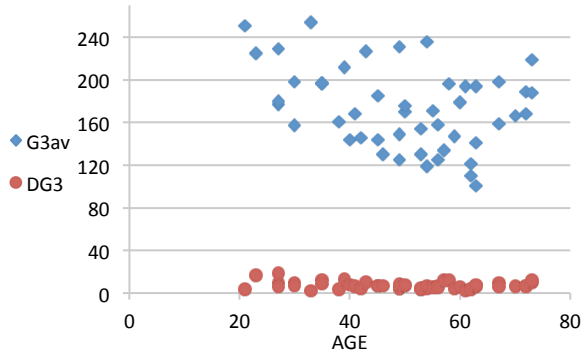


Fig. 7 Dependence of G3av and DG3 (ordinate) upon the age of the patients (abscissa).

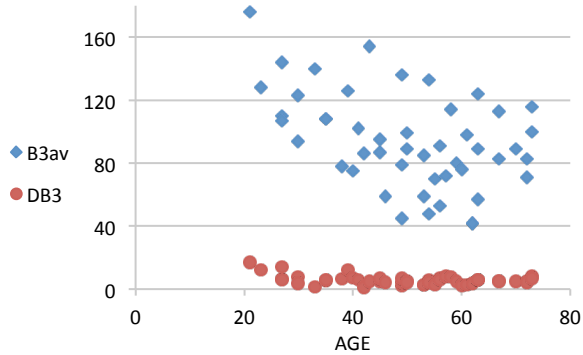


Fig. 8 Dependence of B3av and DB3 (ordinate) upon the age of the patients (abscissa).

According to the developed algorithm the OD domain is divided into three subdomains by applying a special mask, the role of which is to separate the pixels depending on their colour composition. For the RGB version of the program (the program can support the measurements in the HSV model as well) the pixels, for which the values of the red, green, and blue components satisfy the inequalities $R < R_{MIN}$, $G < G_{MIN}$ and $B < B_{MIN}$, are attributed to the subdomain 1 (beyond the OD in Fig. 1 it is shown in white). The pixels for which $R > R_{MAX}$, $G > G_{MAX}$ and $B > B_{MAX}$ belong to the subdomain 3 (the domain of physiological excavation of the OD, in Fig. 1 shown in black). All the rest pixels form the subdomain 2 ("healthy" region of the OD, in

Fig. 1 shown in green colour). The boundary values $R_{MAX, MIN}$, $G_{MAX, MIN}$, and $B_{MAX, MIN}$ are determined by preliminary pixel-by-pixel scanning of the initial image in the top right window (Fig. 1). Figure 2 shows the result of the division of the RGB colour space into three subdomains depending on the mask values R_{MIN}, G_{MIN}, B_{MIN} and R_{MAX}, G_{MAX}, B_{MAX}.

The colourimetric statistical analysis of the OD includes the determination of the mean values of *Rav, Gav, Bav* in the subdomains 2 and 3 of the OD using the program, as well as the calculation of the relevant root-mean-square deviations *DR, DG, DB*. The measurement performed in the groups of patients of different age without expressed signs of glaucoma were aimed at the determination of the boundaries between the norm and pathology for this disease. The results of the analysis are presented in Figs. 3-8 [5].

3 Discussion

As mentioned above, the main goal of the studies was to find a simple criterion for the determination of the domain of the physiological excavation of OD. This is just the domain, in which the phenomena accompanying the glaucoma development are observed. For this aim it is convenient to use the so called variability coefficient [6]: $\boldsymbol{V_{XN} = DXN/XN_{av}}$, where $X = R, G, B$ are the colour components, and $N = 2, 3$ is the number of the subdomain. As shown by the calculations, the value of the variability coefficient *VX2* for the domain conditionally considered as healthy exceeds by more than an order of magnitude the value of the analogous quantity for the domain of physiological excavation *VX3*. The corresponding results of the calculations for the red component ($X = R$) are shown in Fig. 9. For other colour components, the green ($X = G$) and the blue one ($X = B$), the corresponding results demonstrate similar behavior.

As follows from the papers [7-10], similar methods of optic disk analysis are used in the diagnostics of wide spectrum of eye diseases.

The authors of Ref. [7] describe the morphometric analysis of the OD parameters using the laser retina tomograph Heidelberg Engineering Company (HRT). Having appeared at the market of ophthalmological instruments in the middle of 1990s, it promoted the OD examination to the level of accuracy, comparable with that of the computer examination of the central visual field. During the last 10-15 years the Russian and foreign ophthalmologists carried out numerous complex studies of the capabilities of this method in the eyes of healthy persons with normal refraction and myopia, in patients with suspicion of glaucoma, and with different stages of low-pressure glaucoma.

In Refs. [8, 9, 10] the authors propose a method for diagnosing the visual nerve atrophy basing on the eye fundus imaging, extracting the OD region, and analysing its image by means of the computer system. The system includes the fundus camera "OPTON", the high-resolution colour video camera, the software-hardware complex for image digitising and the software for the image analysis. The developed set of indicators for assessing the presence and the degree of the OD decolouration provides the opportunity of the objective assessment of the OD structural changes at the expense of using the calculated integral index in absolute units that allows for the distribution of the values of basic spectral components and does not depend upon the imaging conditions.

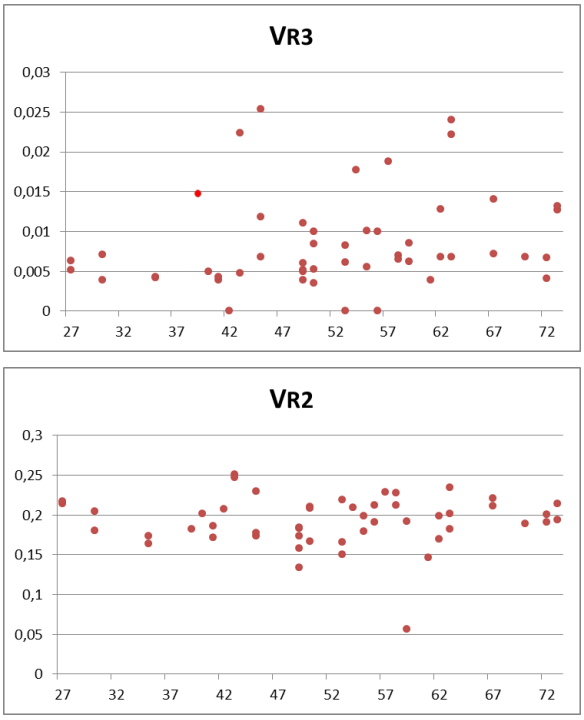


Fig. 9 The values of variability coefficient (ordinate) for the red component in the subdomains 2 (bottom) and 3 (top) for the OD versus the age of the patients (abscissa).

The technique described in the present paper allows the increase of precision and rate of getting objective colour characteristics of the OD and at present has already found application in the clinical practice [11].

4 Conclusion

The paper is devoted to the statistical analysis of the optical disc (OD) image parameters, carried out using a specially developed computer program. We present a brief description of the operation of the program, the calculation technique, and the obtained results. It is shown that one can definitely select the region of physiological excavation of OD by the value of the variability coefficient of the R, G, or B colour component, which becomes strongly reduced within the above region.

5 Acknowledgments

The authors express gratitude to Spirin V. F. and Bakutkin I. V. for collaboration at the stage of clinical tests.